RADC-TR-87-213
In-House Report
November 1987

INCREMENTAL DIFFRACTION COEFFICIENTS FOR PLANAR SURFACES, PART II: Calculation of the Nonuniform Current Correction to PO Reflector Antenna Patterns

Robert A. Shore and Arthur D. Yaghjian

ROME AIR DEVELOPMENT CENTER
Air Force Systems Command
Griffiss Air Force Base, NY 13441-5700

89 6 05 177

This report has been reviewed by the RADC Public Affairs Office (PA) and is releasable to the National Technical Information Service (NTIS). At NTIS it will be releasable to the general public, including foreign nations.

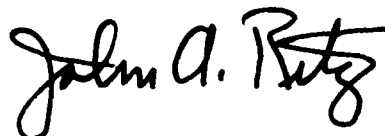RADC-TR-87-213 has been reviewed and is approved for publication.

APPROVED: *Raymond J Cormier*

RAYMOND J. CORMIER
Assistant Chief, Applied Electromagnetics Division
Directorate of Electromagnetics

APPROVED: *John K Schindler*

JOHN K. SCHINDLER
Acting Director of Electromagnetics

FOR THE COMMANDER: *John A. Ritz*

JOHN A. RITZ
Directorate of Plans & Programs

If your address has changed or if you wish to be removed from the RADC mailing list, or if the addressee is no longer employed by your organization, please notify RADC (EEAS) Hanscom AFB MA 01731-5000. This will assist us in maintaining a current mailing list.

Do not return copies of this report unless contractual obligations or notices on a specific document require that it be returned.

REPORT DOCUMENTATION PAGE

1a. REPORT SECURITY CLASSIFICATION Unclassified	1b. RESTRICTIVE MARKINGS

2a. SECURITY CLASSIFICATION AUTHORITY	3. DISTRIBUTION/AVAILABILITY OF REPORT Approved for public release;
2b. DECLASSIFICATION/DOWNGRADING SCHEDULE	Distribution unlimited

4. PERFORMING ORGANIZATION REPORT NUMBER(S) RADC-TR-87-213	5. MONITORING ORGANIZATION REPORT NUMBER(S)

6a. NAME OF PERFORMING ORGANIZATION Rome Air Development Center	6b. OFFICE SYMBOL (If applicable) EEAS	7a. NAME OF MONITORING ORGANIZATION

6c. ADDRESS (City, State, and ZIP Code) Hanscom AFB Massachusetts 01731-5000	7b. ADDRESS (City, State, and ZIP Code)

8a. NAME OF FUNDING/SPONSORING ORGANIZATION	8b. OFFICE SYMBOL (If applicable)	9. PROCUREMENT INSTRUMENT IDENTIFICATION NUMBER

8c. ADDRESS (City, State, and ZIP Code)	10. SOURCE OF FUNDING NUMBERS			
	PROGRAM ELEMENT NO. 61102F	PROJECT NO. 2305	TASK NO. 54	WORK UNIT ACCESSION NO. 04

11. TITLE (Include Security Classification) Incremental Diffraction Coefficients for Planar Surfaces, Part II: Calculation of the Nonuniform Current Correction to PO Reflector Antenna Patterns

12. PERSONAL AUTHOR(S)
 Robert A. Shore, Arthur D. Yaghjian

13a. TYPE OF REPORT In-house	13b. TIME COVERED FROM Jan 87 TO May 87	14. DATE OF REPORT (Year, Month, Day) 1987 November	15. PAGE COUNT 82

16. SUPPLEMENTARY NOTATION

17. COSATI CODES			18. SUBJECT TERMS (Continue on reverse if necessary and identify by block number)
FIELD	GROUP	SUB-GROUP	Diffraction coefficients
			Incremental length
			Reflector antenna

19. ABSTRACT (Continue on reverse if necessary and identify by block number)

   In Part I of this report, we provide a general and convenient method, for determining incremental length diffraction coefficients directly from the conventional two-dimensional diffraction coefficients. This sequel provides a detailed analysis of how the nonuniform incremental diffraction coefficients for the half-plane are integrated around the rim of a reflector. These computed far fields of the nonuniform current, when added to the far fields computed from the physical optics current, produce a more accurate total far field of the reflector. Excellent agreement with the far fields obtained from a method of moments solution to the electric field integral equation applied to a 20-wavelength-diameter reflector shows that the cross polarization, further-out sidelobes, and fields near nulls of reflector antennas can be appreciably changed by the fields of the nonuniform currents. Finally, we evaluate the fields of the nonuniform current of the reflector through conventional asymptotic evaluation of the diffraction integrals and compare these approximate results with the far fields obtained by numerically integrating the nonuniform incremental diffraction coefficients.

20. DISTRIBUTION/AVAILABILITY OF ABSTRACT ☐ UNCLASSIFIED/UNLIMITED ☒ SAME AS RPT. ☐ DTIC USERS	21. ABSTRACT SECURITY CLASSIFICATION Unclassified	
22a. NAME OF RESPONSIBLE INDIVIDUAL Robert A. Shore	22b. TELEPHONE (Include Area Code) (617) 377-2058	22c. OFFICE SYMBOL RADC/EEAS

DD FORM 1473, 84 MAR

83 APR edition may be used until exhausted.
All other editions are obsolete.

Contents

Illustrations

Incremental Diffraction Coefficients for Planar Surfaces, Part II: Calculation of the Nonuniform Current Correction to PO Reflector Antenna Patterns

1. INTRODUCTION

Numerous computer codes exist for calculating the far fields of reflector antennas by integrating either the physical optics (PO) current or the aperture fields obtained from geometrical optics (GO).[1,2] Both the PO current integration and the GO aperture-field integration produce far fields with reasonable and comparable accuracy† out to a sidelobe angle that depends upon whether the edges of the reflector are sharp, flared, absorber-lined, serrated, etc.[3] In particular, for antennas with locally wedge-shaped conducting edges, both PO current and GO aperture-field integration predict nearly the correct copolar fields out to 20° or more.[4] However, even for perfectly conducting reflectors with wedge-shaped edges, the PO current or GO aperture-field integrations neglect the nonuniform currents[5] or fields[6] near the edges and thus fail to produce reliable cross-polarized fields, far-out sidelobes of the copolarized fields and fields near nulls.[7] Thus a number of techniques have been used to improve the accuracy of PO current and GO aperture-field integrations.

The geometrical theory of diffraction[8] (GTD) or the physical theory of diffraction[5] (PTD) can be used to calculate more accurately the far-out sidelobes of reflectors. However, GTD introduces the problem of matching smoothly the far-out sidelobes to the near-in sidelobes, and both PTD and GTD, when applied directly to obtain the far-fields, fail (for a general illumination) to produce accurate co- and cross-polarized fields in the mainbeam region (which is a focal region for the GTD and PTD diffraction coefficients). Morcover, if conventional GTD or PTD is used to first calculate fields on a near-field surface before performing an aperture-field integration to obtain the far fields,[7,9] one is still

---

†The accuracy of the PO current and GO aperture-field integrations is comparable, provided the aperture surface used in the field integration caps the reflector.[3]

faced with the problem of computing accurate near fields in the focal regions. Also, conventional GTD or PTD is not well suited for computing end-point contributions such as from corners, even if higher order distortions of the current near the end-points are neglected.

To overcome this problem of computing fields in caustic and end-point regions, Mitzner[10] introduced PTD "incremental length diffraction coefficients," which, when multiplied by the incident field, could be integrated along the rims of reflectors (for example) to obtain the diffracted fields of the nonuniform current for arbitrary angles of incidence and scattering. Mitzner obtained explicit expressions for the incremental diffraction coefficients of the perfectly conducting wedge. More recently, Michaeli,[11] unaware of Mitzner's report, derived expressions for the GTD incremental diffraction coefficients of the wedge, and Knott[12] has shown that if the PTD incremental diffraction coefficients for the wedge are subtracted from the GTD coefficients, the result is the PO incremental diffraction coefficients. (The concept of incremental diffraction coefficients was used implicitly in work that preceded that of Mitzner,[10] notably that of Ufimtsev,[5] Braunbek,[6] Millar,[13-15] and the "equivalent (edge) current" work of Ryan and Peters.[16] However, this previous work used approximate ad hoc expressions for the incremental fields that did not necessarily agree with the diffracted fields outside the focal regions.)

Part I[17] of this work reviews more thoroughly the key references leading to GTD and PTD incremental diffraction coefficients, and provides a general and convenient method for determining incremental length diffraction coefficients directly from the conventional two-dimensional diffraction coefficients. The main purpose of this sequel (Part II) is to provide the detailed analysis of how the PTD incremental diffraction coefficients for the half-plane are integrated around the rims of reflectors to obtain the far fields produced by the nonuniform currents. These computed far fields of the nonuniform current are added to the far fields computed from the PO current. Excellent agreement with the far fields obtained from a method of moments solution to the electric field integral equation applied to a 20-wavelength-diameter reflector with an 8-wavelength focal length[7,20] shows that indeed the cross-polarization, further-out sidelobes, and fields near nulls of reflector antennas can be appreciably changed by the fields of the nonuniform currents.

Finally, we evaluate the fields of the nonuniform current of the reflector through conventional asymptotic evaluation of the diffraction integrals and compare these approximate resuults with the far fields obtained by numerically integrating the nonuniform incremental diffraction coefficients.

2. ANALYSIS

We wish to improve upon the PO approximation to the far field of a parabolic reflector antenna by taking into account the fact that, in the close vicinity of the rim of the reflector, the PO current does not accurately represent the total current excited on the reflector surface. The total current on the reflector surface, $\overline{K}$, can be represented as the sum of the PO current, $\overline{K}^{PO}$, and the nonuniform current, $\overline{K}^{nu}$, which is prominent only near the reflector rim and which decays rapidly away from the rim. Corresponding to the representation of the total current as

$$\overline{K} = \overline{K}^{PO} + \overline{K}^{nu}$$

is the representation of the total electric far field scattered by the reflector, $\overline{E}_s$, as the sum of the PO far field, $\overline{E}^{PO}$, and the far field of the nonuniform current, $\overline{E}^{nu}$; that is,

$$\bar{E}_s = \bar{E}^{PO} + \bar{E}^{nu} \tag{1}$$

with the far field given in terms of surface integrals of the respective currents. The far-field contribution of the nonuniform current can be found by subdividing the rim into differential lengths, determining the far field of each such differential length, and integrating this far field over the rim of the reflector.

The far field of a differential length (the incremental diffraction coefficient) can often be well approximated by the corresponding far field of a canonical scatterer that conforms to the reflector at the rim and that is excited by a plane wave whose propagation vector is in the direction from the feed to the rim element and whose amplitude and phase at the point of incidence are those of the feed radiation. In general, the rim of the reflector may not conform to a canonical scatterer with a known incremental diffraction coefficient. However, the rims of many reflectors are well approximated locally by perfectly conducting wedges. Incremental diffraction coefficients for the perfectly conducting wedge have been derived by Mitzner[10] for the nonuniform current, Michaeli[11] for the total current, and Knott[12] for the PO current. (Since the total current is the sum of the PO and nonuniform currents, any two of the coefficients determine the third.) For simplicity here, we will consider the special, though important, case of a parabolic reflector whose rim can be modeled locally by an infinitesimally thin, perfectly conducting half-plane. The correction, $\bar{E}^{nu}$, to the PO reflector far field is thus obtained by integrating the nonuniform current incremental diffraction coefficient for the half-plane around the reflector rim.

2.1 Incremental Diffraction Coefficients for the Nonuniform Current of the Half-Plane

The half-plane nonuniform current incremental diffraction coefficient, $\overline{dE}^{nu}\,(\bar{r})$, is given by

$$\overline{dE}^{nu}\,(\bar{r}) = \overline{dE}_s\,(\bar{r}) - \overline{dE}^{PO}\,(\bar{r}) \tag{2}$$

where $\overline{dE}_s\,(\bar{r})$ and $\overline{dE}^{PO}\,(\bar{r})$ are the half-plane incremental diffraction coefficients for the total current and PO current respectively, and $\bar{r}$ is the vector from the rim point to the far field point. Expressions for $\overline{dE}_s\,(\bar{r})$ and $\overline{dE}^{PO}\,(\bar{r})$ for the perfectly conducting wedge were derived in Part I and shown to agree with Michaeli and Knott (and thus indirectly with Mitzner) as a check on our general method for obtaining incremental diffraction coefficients. (The total incremental diffraction coefficients for a perfectly conducting half-plane were also derived directly in Part I.) Specifically, the half-plane incremental diffraction coefficients may be expressed as follows:

$$\overline{dE}_s^{TM}\,(\bar{r}) \xrightarrow{r \to \infty} -\,dz' E_{iz}\,\frac{e^{ikr}}{4\pi r}\,\frac{\sin\theta}{\sin^2\theta_0}\,\frac{4\sin\frac{\alpha}{2}\sin\frac{\phi_0}{2}}{\cos\alpha + \cos\phi_0}\,\hat{\theta} \tag{3}$$

$$\overline{dE}^{PO(TM)}\,(\bar{r}) \xrightarrow{r \to \infty} -\,dz'\,\text{sign}(\pi - \phi_0)E_{iz}\,\frac{e^{ikr}}{4\pi r}\,\frac{\sin\theta}{\sin^2\theta_0}\,\frac{2\sin\phi_0}{\cos\alpha + \cos\phi_0}\,\hat{\theta} \tag{4}$$

$$\overline{dE}_s^{TE}\,(\bar{r}) \xrightarrow{r \to \infty} -\,dz' Z_0 \frac{H_{iz}}{\sin\theta_0}\,\frac{e^{ikr}}{4\pi r}\,\frac{4\cos\frac{\alpha}{2}\cos\frac{\phi_0}{2}}{\cos\alpha + \cos\phi_0}\,\frac{1}{\sin\alpha}$$

$$\cdot\,[\sin\phi\,\hat{\phi} - (\cos\phi\cos\theta + \cos\alpha\sin\theta\cot\theta_0)\,\hat{\theta}] \tag{5}$$

3

and

$$\overline{dE}^{PO(TE)}(\bar{r}) \; {}_{r\to\infty} \; -dz' \; \text{sign}(\pi - \phi_0) \; Z_0 \frac{H_{iz}}{\sin\theta_0} \frac{e^{ikr}}{4\pi r} \frac{2}{\cos\alpha + \cos\phi_0}$$

$$\cdot \; [\sin\phi\hat{\phi} - (\cos\phi\cos\theta - \cos\phi_0\sin\theta\cot\theta_0)] \tag{6}$$

where $0 < \phi \leq 2\pi$ and

$$\alpha = \cos^{-1}\left(\frac{\sin\theta}{\sin\theta_0}\cos\phi\right). \tag{7}$$

In these expressions, $\overline{dE}_s^{TM}(\bar{r})$ and $\overline{dE}_s^{PO(TM)}(\bar{r})$ are the incremental diffraction coefficients for the total and PO currents, respectively, for a half-plane illuminated by a TM (E-polarized) plane wave, and $\overline{dE}_s^{TE}(\bar{r})$ and $\overline{dE}_s^{PO(TE)}(\bar{r})$ are the corresponding diffraction coefficients for TE (H-polarized) plane-wave illumination. The half-plane is defined in terms of Cartesian coordinates (x,y,z) by the equations $y = 0$, $x \geq 0$, so that the edge of the half-plane coincides with the z-axis. The origin of the coordinate system is taken to be at the differential element (incremental length) dz' of the half-plane edge. The directions of the incident plane wave and the point of observation are given by the spherical coordinate angles (θ_0, ϕ_0) and (θ, ϕ), respectively (see Figure 1). E_{iz} and H_{iz} are the complex amplitudes of the electric and magnetic components, respectively, of the illuminating plane waves parallel to the edge of the half-plane at the origin, Z_0 is the free-space impedance, and $r = |\bar{r}|$, the distance from the origin to the field point.
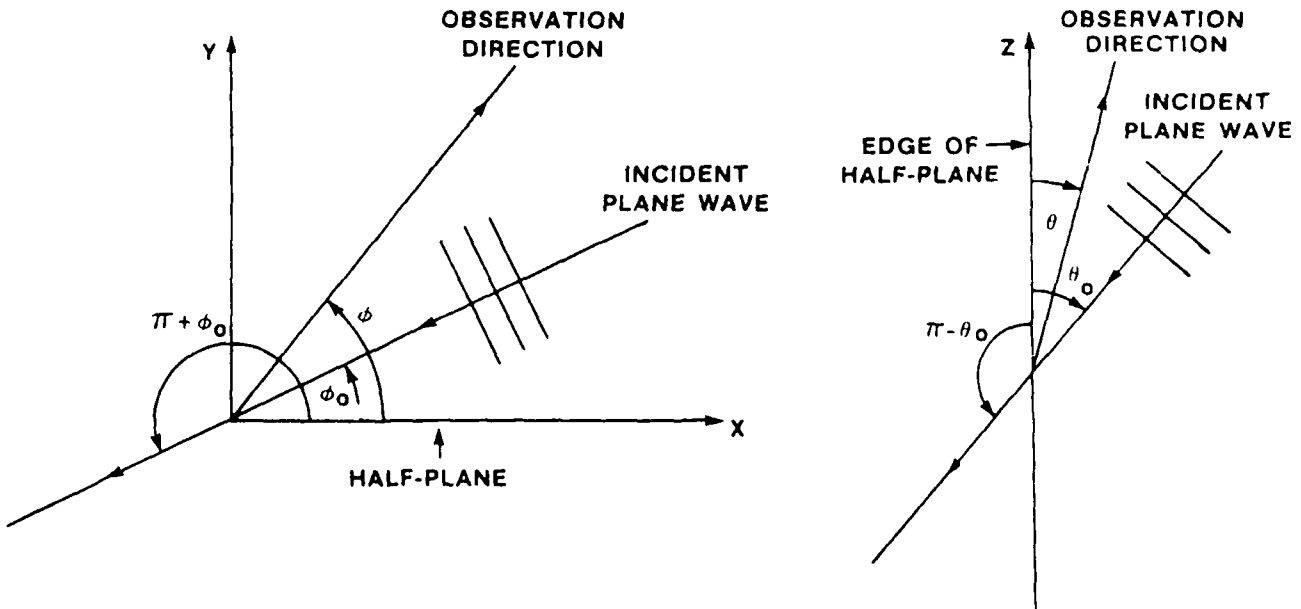
Figure 1. Geometry of a Half-Plane Illuminated by a Plane Wave

The half-plane incremental diffraction coefficient for the nonuniform current and TM plane-wave illumination is obtained by substituting Eq. (3) and Eq. (4) into Eq. (2) and using elementary trigonometric identities to simplify the resulting expression to

$$\overline{dE}^{\,nu(TM)}\,(\bar{r})\,{}^{r\rightarrow\infty}\,dz'\,E_{iz}\,\frac{e^{ikr}}{4\pi r}\,\frac{\sin\theta}{\sin^2\theta_0}\,\frac{2\sin\frac{\phi_0}{2}}{|\cos\frac{\phi_0}{2}|+\sin\frac{\alpha}{2}}\,\hat{\theta}.\tag{8}$$

Similarly, the half-plane incremental diffraction coefficient for the nonuniform current and TE plane-wave illumination is found, by substituting Eq. (5) and Eq. (6) into Eq. (2) and simplifying trigonometrically, to be

$$\overline{dE}^{\,nu(TE)}\,(\bar{r})\,{}^{r\rightarrow\infty}\,-\,dz'\,\text{sign}(\pi-\phi_0)Z_0\,\frac{H_{iz}}{\sin\theta_0}\,\frac{e^{ikr}}{4\pi r}\,\frac{1}{\sin\frac{\alpha}{2}\left(|\cos\frac{\phi_0}{2}|+\sin\frac{\alpha}{2}\right)}$$

$$\cdot\left\{\sin\phi\,\hat{\phi}-\left[\cos\phi\cos\theta+\left(1+2\,|\cos\frac{\phi_0}{2}|\,\sin\frac{\alpha}{2}\right)\sin\theta\cot\theta_0\right]\hat{\theta}\right\}\tag{9}$$

For arbitrarily polarized plane-wave illumination, the half-plane nonuniform incremental diffraction coefficient is then obtained by summing Eq. (8) and Eq. (9):

$$\overline{dE}^{\,nu}\,(\bar{r}_\ell)\,{}^{r\rightarrow\infty}dz'_\ell\,\frac{e^{ikr_\ell}}{4\pi r_\ell\sin\theta_{0\ell}}\,\frac{1}{|\cos\frac{\phi_{0\ell}}{2}|+\sin\frac{\alpha}{2}}$$

$$\left\{\left[E_{iz\ell}\,\frac{2\sin\theta_\ell}{\sin\theta_{0\ell}}\,\sin\frac{\phi_{0\ell}}{2}\right.\right.$$

$$+\,\text{sign}(\pi-\phi_{0\ell})\,Z_0\,\frac{H_{iz\ell}}{\sin\frac{\alpha}{2}}\left(\cos\phi_\ell\cos\theta_\ell+\left[1+2|\cos\frac{\phi_{0\ell}}{2}|\,\sin\frac{\alpha}{2}\right]\sin\theta_\ell\cot\theta_{0\ell}\right)\Big]\hat{\theta}_\ell$$

$$-\,\text{sign}\,(\pi-\phi_{0\ell})Z_0\frac{H_{iz\ell}}{\sin\frac{\alpha}{2}}\,\sin\phi_\ell\,\hat{\phi}_\ell\right\}\tag{10}$$

with

$$\alpha=\cos^{-1}\left(\frac{\sin\theta_\ell}{\sin\theta_{0\ell}}\,\cos\phi_\ell\right)\tag{11}$$

5

We have inserted the subscripts "ℓ" in Eq. (10) and Eq. (11), indicating that the subscripts are defined with reference to a local coordinate system with origin at the incremental length, to clearly distinguish these locally defined quantities from those defined with reference to the global coordinate system of the reflector antenna introduced in the next subsection.

2.2 Transformation to the Global Coordinate System of the Reflector

The correction to the PO electric far field of the reflector antenna is obtained as indicated above by integrating Eq. (10) around the rim of the reflector. Since all quantities in Eq. (10) are defined with respect to a local coordinate system with origin at the differential element of the reflector rim, it is first necessary to transform Eq. (10) to a global coordinate system which we will take here to be that shown in Figure 2.

The origin of the global coordinate system is the focus of the parabolic reflector of focal length F and diameter D, and the z-axis is the axis of the reflector directed towards the center of the reflector. Primed coordinates are used to indicate integration points on the reflector rim, and unprimed coordinates to indicate the field points. It is also necessary to define the local coordinate system with origin at the point of integration on the reflector rim. Since we are modelling the rim locally by the half-plane defined as
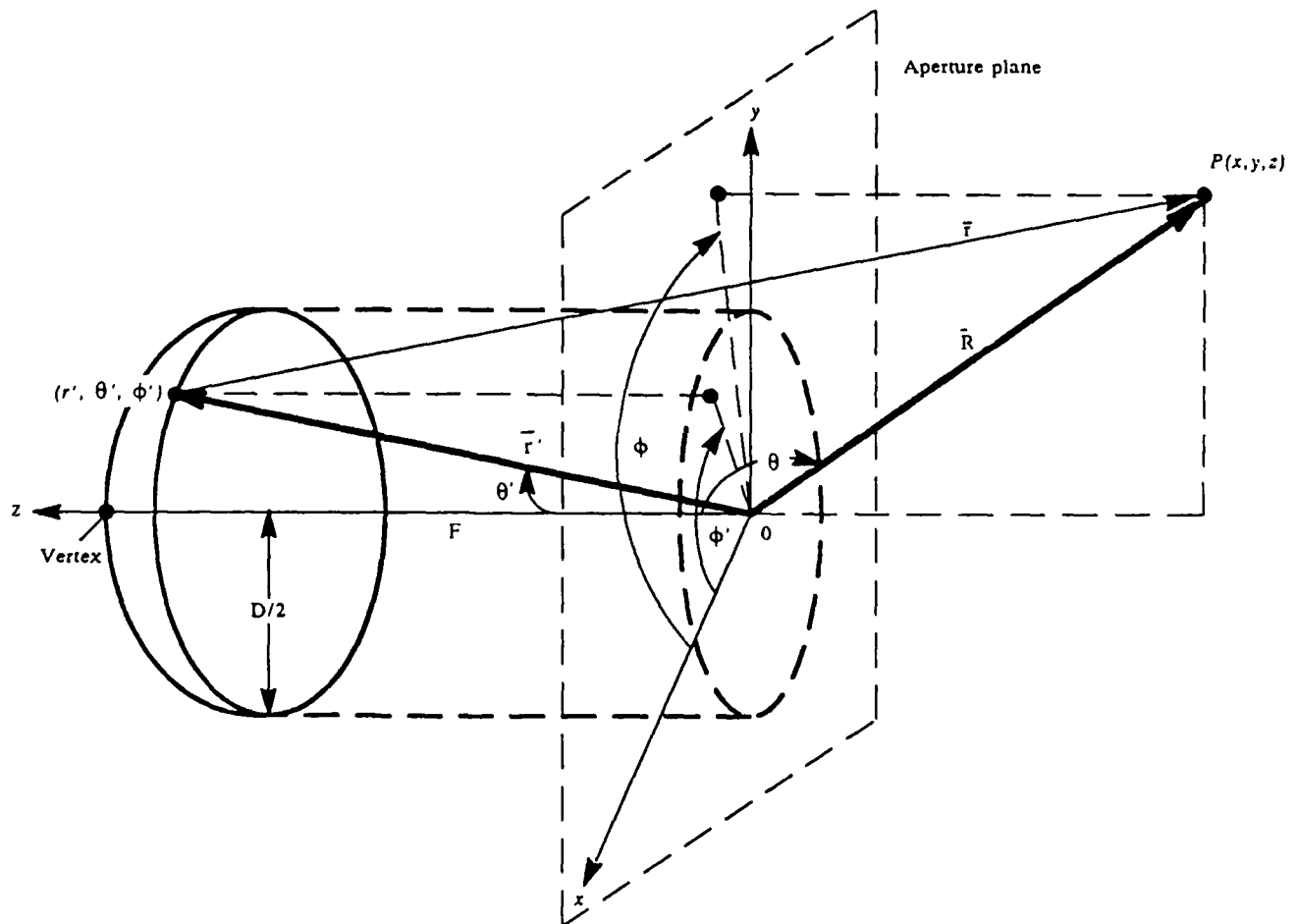
Figure 2. Global Coordinate System for Paraboloidal Reflector

6

shown in Figure 1 (the incident plane wave in Figure 1 corresponds to the ray from the feed at the focus to the rim point), we want the local x-axis to be tangent to the reflector at the rim, normal to the rim, and directed inward from the rim; and the local y-axis to be the inwardly directed normal to the paraboloid at the rim. Thus

$$\hat{x}_\ell = -\sin \frac{\theta'}{2}\hat{r}' - \cos \frac{\theta'}{2} \hat{\theta}' \tag{12}$$

and

$$\hat{y}_\ell = -\cos \frac{\theta'}{2} \hat{r}' + \sin \frac{\theta'}{2}\hat{\theta}' \tag{13}$$

with θ', the angle at the focus subtended by points on the rim, given by

$$\theta' = \tan^{-1}\left[\frac{\frac{1}{2}\frac{F}{D}}{\left(\frac{F}{D}\right)^2 - \frac{1}{16}}\right] = 2 \cot^{-1}\left(\frac{4F}{D}\right) . \tag{14}$$

Hence

$$\hat{z}_\ell = \hat{x}_\ell \times \hat{y}_\ell = -\hat{\phi}' . \tag{15}$$

We now systematically express the locally defined quantities of Eq. (10) and Eq. (11) in the global coordinate system. Starting with $\theta_{0\ell}$, the angle between the local unit z-vector, $-\hat{\phi}'$, and the ray $-\hat{r}'$ from the rim point to the feed at the focus, it is apparent that $\theta_{0\ell} = \pi/2$ so that

$$\cos \theta_{0\ell} = 0 \tag{16a}$$

and

$$\sin \theta_{0\ell} = 1 . \tag{16b}$$

Next, since $\phi_{0\ell}$ is the angle between $\hat{x}_\ell$ and the projection of $-\hat{r}'$ on the $x_\ell y_\ell$-plane (see Figure 2), we have

$$\cos \phi_{0\ell} = -\hat{r}' \cdot \hat{x}_\ell/\sin \theta_{0\ell} = \sin \frac{\theta'}{2} \tag{17a}$$

and

$$\sin \phi_{0\ell} = -\hat{r}' \cdot \hat{y}_{\ell}/\sin \theta_{0\ell} = \cos \frac{\theta'}{2} \qquad (17b)$$

from which

$$\cos \frac{\phi_{0\ell}}{2} = \left(\frac{1 + \sin \frac{\theta'}{2}}{2} \right)^{1/2} \qquad (18a)$$

and

$$\sin \frac{\phi_{0\ell}}{2} = \left(\frac{1 - \sin \frac{\theta'}{2}}{2} \right)^{1/2} . \qquad (18b)$$

Proceeding to θ_{ℓ}, the angle between $\hat{z}_{\ell}$ and the ray from the rim point to the far-field point,

$$\cos \theta_{\ell} = -\hat{\phi}' \cdot \hat{r}_{\ell} .$$

But $\hat{r}_{\ell}$, the unit vector from the rim point to the far-field point, is parallel to $\hat{R}$, the unit vector from the focus to the far field point. Hence

$$\begin{aligned}
\cos \theta_{\ell} &= -\hat{\phi}' \cdot \hat{R} \\
&= (\sin \phi' \, \hat{x} - \cos \phi' \, \hat{y}) \cdot (\sin \theta \cos \phi \hat{x} + \sin \theta \sin \phi \hat{y} + \cos \theta \hat{z}) \\
&= \sin \theta \sin (\phi' - \phi) \qquad (19a)
\end{aligned}$$

and

$$\sin \theta_{\ell} = [1 - \sin^2\theta \sin^2(\phi' - \phi)]^{1/2} \qquad (19b)$$

where the positive root must be taken since $0 \le \theta_{\ell} \le \pi$. (For $\theta = \pi/2$, $\sin \theta_{\ell} = |\cos(\phi' - \phi)|$.) The cosine and sine of ϕ are given by

$$\cos \phi_{\ell} = \hat{r}_{\ell} \cdot \hat{x}_{\ell}/\sin \theta_{\ell}$$

and

$$\sin \phi_{\ell} = \hat{r}_{\ell} \cdot \hat{y}_{\ell}/\sin \theta_{\ell} .$$

Again, replacing $\hat{r}_\ell$ by $\hat{R}$ and then switching to Cartesian components and simplifying trigonometrically, we obtain

$$\cos \phi_\ell = \left[-\cos \frac{\theta'}{2} \sin \theta \cos(\phi' - \phi) + \sin \frac{\theta'}{2} \cos \theta \right]\Big/ \sin \theta_\ell \tag{20a}$$

and

$$\sin \phi_\ell = \left[-\sin \frac{\theta'}{2} \sin \theta \cos(\phi' - \phi) - \cos \frac{\theta'}{2} \cos \theta \right]\Big/ \sin \theta_\ell \tag{20b}$$

with $\sin \theta_\ell$ given by Eq. (19b). The angle α given by Eq. (11) is now also expressed in the global coordinate system since $\sin \theta_{0\ell}$, $\sin \theta_\ell$, and $\cos \phi_\ell$ are given by Eq. (16b), Eq. (19b), and Eq. (20a), respectively. In particular,

$$\sin \frac{\alpha}{2} = \left(\frac{1 - \cos \alpha}{2} \right)^{1/2} \tag{21}$$

with

$$\cos \alpha = \sin \theta_\ell \cos \phi_\ell .$$

The unit vector $\hat{\theta}_\ell$ is transformed to the global coordinate system by starting with

$$\hat{\theta}_\ell = \cos \theta_\ell \cos \phi_\ell \hat{x}_\ell + \cos \theta_\ell \sin \phi_\ell \hat{y}_\ell - \sin \theta_\ell \hat{z}_\ell ,$$

substituting global Cartesian component expressions for $\hat{x}_\ell$, $\hat{y}_\ell$, and $\hat{z}_\ell$, and simplifying trigonometrically, thereby obtaining

$$\hat{\theta}_\ell = - \left[\cos \theta_\ell \cos \phi' \left(\cos \frac{\theta'}{2} \cos \phi_\ell + \sin \frac{\theta'}{2} \sin \phi_\ell \right) + \sin \theta_\ell \sin \phi' \right] \hat{x}$$

$$- \left[\cos \theta_\ell \sin \phi' \left(\cos \frac{\theta'}{2} \cos \phi_\ell + \sin \frac{\theta'}{2} \sin \phi_\ell \right) - \sin \theta_\ell \cos \phi' \right] \hat{y}$$

$$- \cos \theta_\ell \left(\cos \frac{\theta'}{2} \sin \phi_\ell - \sin \frac{\theta'}{2} \cos \phi_\ell \right) \hat{z} \tag{22}$$

with $\cos \theta_\ell$, $\sin \theta_\ell$, $\cos \phi_\ell$, and $\sin \phi_\ell$ given by Eq. (19a), Eq. (19b), Eq. (20a), and Eq. (20b) respectively. A similar procedure gives

$$\hat{\phi}_\ell = \cos\phi'\left(\cos\frac{\theta'}{2}\sin\phi_\ell - \sin\frac{\theta'}{2}\cos\phi_\ell\right)\hat{x}$$

$$+ \sin\phi'\left(\cos\frac{\theta'}{2}\sin\phi_\ell - \sin\frac{\theta'}{2}\cos\phi_\ell\right)\hat{y}$$

$$- \left(\sin\frac{\theta'}{2}\sin\phi_\ell + \cos\frac{\theta'}{2}\cos\phi_\ell\right)\hat{z}. \tag{23}$$

Next, proceeding to e^{ikr_ℓ}/r_1 and replacing r_ℓ by r (see Figure 2),

$$\frac{e^{ikr_\ell}}{r_\ell} = \frac{e^{ikr}}{r}\,_{r\to\infty}\,\frac{e^{ik(R - \bar{r}'\cdot\hat{R})}}{R} \tag{24}$$

where R is the distance from the reflector focus to the far-field oint. It is then simple to find that

$$\bar{r}'\cdot\hat{R} = r'\left[\sin\theta'\sin\theta\cos(\phi' - \phi) + \cos\theta'\cos\theta\right] \tag{25}$$

where

$$r' = \frac{2F}{1 + \cos\theta'} = F\sec^2\left(\frac{\theta'}{2}\right) \tag{26}$$

and θ' is given by Eq. (14). The differential length dz'_ℓ is given by

$$dz'_\ell = -r'\sin\theta'd\phi' = -2F\tan\frac{\theta'}{2}\,d\phi' \tag{27}$$

and, referring to Eq. (15), $E_{iz\ell}$ and $H_{iz\ell}$ become

$$E_{iz\ell} = -E_{i\phi'} \tag{28a}$$

and

$$H_{iz\ell} = -H_{i\phi'} \tag{28b}$$

in the global coordinate system. Substituting explicit expressions for $\cos\phi_{0\ell}$, $\sin\theta_{0\ell}$, r_ℓ, dz'_ℓ, $E_{iz\ell}$, and $H_{iz\ell}$ in Eq. (9), and noting from Eqs. (17a, b) that $\theta_{0\ell}$, and hence also $\phi_{0\ell}/2$, lies in the first quadrant for the reflector geometry we are considering, gives

$$\overline{dE}^{nu}(\vec{r}) \xrightarrow{r \to \infty} \frac{e^{ikR}}{4\pi R} \, r' \sin \theta' d\phi' e^{-ik\vec{r}' \cdot \hat{R}} \, \frac{1}{\cos \frac{\phi_{0\ell}}{2} + \sin \frac{\alpha}{2}}$$

$$\cdot \left[\left(E_{i\phi'} \, 2 \sin \theta_\ell \sin \frac{\phi_{0\ell}}{2} + Z_0 H_{i\phi'} \, \frac{\cos \phi_\ell \cos \theta_\ell}{\sin \frac{\alpha}{2}} \right) \hat{\theta}_\ell - Z_0 H_{i\phi'} \, \frac{\sin \phi_\ell}{\sin \frac{\alpha}{2}} \, \hat{\phi}_\ell \right] \tag{29}$$

where expressions in global coordinates have been derived above for all locally subscripted quantities.

2.3 Incremental Transverse Far-Field Components

Before integrating with respect to ϕ', it is desirable to obtain explicit expressions for $dE_\theta^{nu}(\vec{r})$ and $dE_\phi^{nu}(\vec{r})$, since, when integrated, these will yield the θ- and ϕ-components of the nonuniform current electric far field (the radial component of the far field is, of course, zero). Thus, we let

$$\sigma = \hat{\theta}_\ell \cdot \hat{\theta}, \ \tau = \hat{\theta}_\ell \cdot \hat{\phi}, \ \mu = \hat{\phi}_\ell \cdot \hat{\theta}, \ \nu = \hat{\phi}_\ell \cdot \hat{\phi} \ . \tag{30}$$

Substituting Eq. (30) in Eq. (29) gives

$$dE_\theta^{nu}(\vec{r}) \xrightarrow{r \to \infty} \frac{e^{ikR}}{4\pi R} \, r' \sin \theta' d\phi' e^{-ik\vec{r}' \cdot \hat{R}} \, \frac{1}{\cos \frac{\phi_{0\ell}}{2} + \sin \frac{\alpha}{2}}$$

$$\cdot \left[\left(E_{i\phi'} \, 2 \sin \theta_\ell \sin \frac{\phi_{0\ell}}{2} + Z_0 H_{i\phi'} \, \frac{\cos \phi_\ell \cos \theta_\ell}{\sin \frac{\alpha}{2}} \right) \sigma - Z_0 H_{i\phi'} \, \frac{\sin \phi_\ell}{\sin \frac{\alpha}{2}} \, \mu \right] . \tag{31}$$

and

$$dE_\phi^{nu}(\vec{r}) \xrightarrow{r \to \infty} \frac{e^{ikR}}{4\pi R} \, r' \sin \theta' d\phi' e^{-ik\vec{r}' \cdot \hat{R}} \, \frac{1}{\cos \frac{\phi_{0\ell}}{2} + \sin \frac{\alpha}{2}}$$

$$\cdot \left[\left(E_{i\phi'} \, 2 \sin \theta_\ell \sin \frac{\phi_{0\ell}}{2} + Z_0 H_{i\phi'} \, \frac{\cos \phi_\ell \cos \theta_\ell}{\sin \frac{\alpha}{2}} \right) \tau - Z_0 H_{i\phi'} \, \frac{\sin \phi_\ell}{\sin \frac{\alpha}{2}} \, \nu \right] . \tag{32}$$

To find σ and τ, we start with Eq. (22), which can be represented as

$$\hat{\theta}_\ell = a\hat{x} + b\hat{y} + c\hat{z}$$

so that

$$\sigma = a \cos \theta \cos \phi + b \cos \theta \sin \phi - c \sin \theta \tag{33}$$

11

and

$$\tau = -a \sin \phi + b \cos \phi .$$ (34)

Substituting explicit expressions for a, b, and c from Eq. (22) into Eq. (33) and Eq. (34), and making the convenient change of variable

$$u = \phi' - \phi$$ (35)

(suggested by the $\phi' - \phi$ dependence of $\cos \theta_\ell$, $\sin \theta_\ell$, $\cos \phi_\ell$, $\sin \phi_\ell$, α, and $\bar{r}' \cdot \hat{R}$) so that

$$\cos \phi' = \cos \phi \cos u - \sin \phi \sin u$$ (36a)

and

$$\sin \phi' = \sin \phi \cos u + \cos \phi \sin u,$$ (36b)

and substituting for $\cos \theta_\ell$, $\sin \theta_\ell$, $\cos \phi_\ell$, $\sin \phi_\ell$ from Eqs. (19) and (20) leads to

$$\sigma = -\frac{\cos \theta \sin u}{(1 - \sin^2 \theta \sin^2 u)^{1/2}}$$ (37)

and

$$\tau = \frac{\cos u}{(1 - \sin^2 \theta \sin^2 u)^{1/2}}$$ (38)

Similarly, by starting with Eq. (23) for $\hat{\phi}_\ell$, we obtain

$$\mu = -\frac{\cos u}{(1 - \sin^2 \theta \sin^2 u)^{1/2}}$$ (39)

and

$$\nu = -\frac{\cos \theta \sin u}{(1 - \sin^2 \theta \sin^2 u)^{1/2}} \tag{40}$$

2.4 Feed Illumination

It is now necessary to specify the form of the feed illumination of the reflector. This is chosen to be

$$\bar{E}_i = \frac{e^{ikr'}}{r'} [a(\theta')\cos \phi' \hat{\theta}' + d(\theta')\sin \phi' \hat{\phi}'] \tag{41a}$$

and

$$\bar{H}_i = \frac{e^{ikr'}}{Z_0 r'} [a(\theta')\cos \phi' \hat{\phi}' - d(\theta')\sin \phi' \hat{\theta}'] \tag{41b}$$

so that the E-plane is the xz-plane and the H-plane is the yz-plane. For an x-directed electric dipole source

$$a(\theta') = \cos \theta', d(\theta') = -1, \tag{42}$$

while for a Huygens source with an x-directed electric dipole and a y-directed magnetic dipole

$$a(\theta') = 1 + \cos \theta', d(\theta') = -(1 + \cos \theta'). \tag{43}$$

Thus

$$E_{i\phi'} = \frac{e^{ikr'}}{r'} d(\theta')\sin \phi' = \frac{e^{ikr'}}{r'} d(\theta')(\sin \phi \cos u + \cos \phi \sin u) \tag{44a}$$

and

$$H_{i\phi'} = \frac{e^{ikr'}}{Z_0 r'} a(\theta')\cos \phi' = \frac{e^{ikr'}}{Z_0 r'} a(\theta')(\cos \phi \cos u - \sin \phi \sin u), \tag{44b}$$

applying Eq. (35). Substituting Eq. (44a) and Eq. (44b) in Eq. (31) and Eq. (32) and replacing $d\phi'$ by du gives

$$dE_\theta^{nu}(\bar{r}) \xrightarrow{r \to \infty} \frac{e^{ikR}}{4\pi R} \sin\theta' \, du \, e^{ik(r' - \hat{r}' \cdot \hat{R})} \frac{1}{\cos\frac{\phi_{0\ell}}{2} + \sin\frac{\alpha}{2}}$$

$$\cdot \left[2d(\theta')\sin\theta_\ell \sin\frac{\phi_{0\ell}}{2} (\sin\phi\cos u + \cos\phi\sin u)\sigma \right.$$

$$\left. + a(\theta') \left(\frac{\cos\phi\cos u - \sin\phi\sin u}{\sin\frac{\alpha}{2}} \right)(\cos\theta_\ell\cos\phi_\ell\,\sigma - \sin\phi_\ell\,\mu) \right] \qquad (45)$$

and

$$dE_\phi^{nu}(\bar{r}) \xrightarrow{r \to \infty} \frac{e^{ikR}}{4\pi R} \sin\theta' \, du \, e^{ik(r' - \hat{r}' \cdot \hat{R})} \frac{1}{\cos\frac{\phi_{0\ell}}{2} + \sin\frac{\alpha}{2}}$$

$$\cdot \left[2d(\theta')\sin\theta_\ell \sin\frac{\phi_{0\ell}}{2} (\sin\phi\cos u + \cos\phi\sin u)\,\tau \right.$$

$$\left. + a(\theta') \left(\frac{\cos\phi\cos u - \sin\phi\sin u}{\sin\frac{\alpha}{2}} \right)(\cos\theta_\ell\cos\phi_\ell\,\tau - \sin\phi_\ell\,\nu) \right]. \qquad (46)$$

2.5 Integration of the Incremental Fields

While Eq. (45) and Eq. (46) can be integrated numerically as they stand, substantial simplification as well as analytic clarification can be effected by eliminating those parts of the integrands that are odd functions of u and hence vanish when integrated with respect to u from $-\pi$ to π. [Note from Eq. (15) that in order to obtain the proper sign of the far field components, the integration must be performed in the negative u or negative ϕ' direction, since this corresponds to integration in the positive z_ℓ direction; see Eq. (15).] It is straightforward to show that all terms in $dE_\phi^{nu}(\bar{r})$ containing $\sin\phi$ and all terms in $dE_\theta^{nu}(\bar{r})$ containing $\cos\phi$ are odd functions of u so that

$$E_\theta^{nu}(\bar{R}) \xrightarrow{r \to \infty} \cos\phi \, \frac{e^{ikR}}{4\pi R} \sin\theta' \int_\pi^{-\pi} du \, e^{ik(r' - \hat{r}' \cdot \hat{R})} \frac{1}{\cos\frac{\phi_{0\ell}}{2} + \sin\frac{\alpha}{2}}$$

$$\cdot \left[2d(\theta')\sin\theta_\ell \sin\frac{\phi_{0\ell}}{2} \sin u \, \sigma + a(\theta') \frac{\cos u}{\sin\frac{\alpha}{2}} (\cos\theta_\ell\cos\phi_\ell\,\sigma - \sin\phi_\ell\,\mu) \right] \qquad (47)$$

and

$$E_\phi^{nu}(\bar{R}) \xrightarrow{r \to \infty} \sin\phi \, \frac{e^{ikR}}{4\pi R} \sin\theta' \int_\pi^{-\pi} du \, e^{ik(r' - \hat{r}' \cdot \hat{R})} \frac{1}{\cos\frac{\phi_{0\ell}}{2} + \sin\frac{\alpha}{2}}$$

$$\cdot \left[2d(\theta')\sin\theta_\ell \sin\frac{\phi_{0\ell}}{2} \cos u \, \tau - a(\theta') \frac{\sin u}{\sin\frac{\alpha}{2}} (\cos\theta_\ell\cos\phi_\ell\,\tau - \sin\phi_\ell\,\nu) \right]. \qquad (48)$$

14

Thus $E_\theta^{nu}(\bar{R})$ and $E_\phi^{nu}(\bar{R})$ vary as $\cos\phi$ and $\sin\phi$ respectively. If the co- and cross-polarized field components, E_{co} and E_{cr}, are defined according to Ludwig's third definition[18]

$$E_{co} = E_\theta \cos\phi + E_\phi \sin\phi , \qquad (49a)$$

and

$$E_{cr} = E_\theta \sin\phi - E_\phi \cos\phi , \qquad (49b)$$

then there is no cross-polarized field in either the E- or H-planes.

3. CALCULATIONS

In Section 3.1, we enhance the accuracy of the far field of the paraboloid reflector by numerically integrating the nonuniform incremental diffraction coefficient around the rim of the reflector and adding this correction or "nonuniform" field to the PO fields of the reflector. The E-plane, H-plane, and 45°-plane amplitude and phase patterns of a 20λ diameter reflector with F/D = 0.4 are computed for both electric-dipole and Huygens sources feeding the reflector. Plots of the PO far fields and the PO plus nonuniform far fields are shown with and without the primary far fields of the feed included. Excellent agreement is found with the patterns obtained from the method of moments (surface integral equation) solution of Bach, Viskum and Frandsen.[7,20]

In Section 3.2, we compare the amplitude and phase of the nonuniform far field calculated by numerical integration of the nonuniform diffraction coefficient with that calculated by conventional asymptotic evaluation of the diffraction integrals. Expected good agreement is seen except in the forward and back caustic regions where the asymptotic expressions diverge to infinity.

3.1 Far Fields of a Thin Metal Paraboloid Reflector

The field of a paraboloid reflector was calculated by integrating the nonuniform current incremental diffraction coefficient around the reflector rim and adding the result to the PO reflector field. The PO field was obtained from the following formulation due to Rusch:[19]

$$E_\theta^{PO} = ikF \cos\phi \, \frac{e^{ikR}}{R} \int_0^{\theta_0} \frac{e^{ikr'(1-\cos\theta\cos\theta')}}{1+\cos\theta'}$$

$$\cdot \left\{ a(\theta') \cos\theta \, [J_0(\beta) - J_2(\beta)] - d(\theta')\cos\theta \, [J_0(\beta) + J_2(\beta)] \right.$$

$$\left. - 2ia(\theta') \sin\theta \, \tan\!\left(\frac{\theta'}{2}\right) J_1(\beta) \right\} \sin\theta' d\theta' . \qquad (50)$$

15

$$E_\phi^{PO} = -ikF \sin \phi \; \frac{e^{ikR}}{R} \int_0^{\theta_0} \frac{e^{ikr'(1-\cos\theta\cos\theta')}}{1+\cos\theta'}$$

$$\cdot \{a(\theta') [J_0(\beta) + J_2(\beta)] - d(\theta') [J_0(\beta) - J_2(\beta)]\} \sin\theta' d\theta' \; . \tag{51}$$

In these equations, R, θ and ϕ are the spherical polar coordinates of the field point; θ' is now a variable instead of being fixed at the angle subtended by the reflector rim as in Section 2; θ_0 is the angle at the focus between the z-axis and a ray from the focus to a point on the rim; $a(\theta')$ and $d(\theta')$ specify the feed illumination [cf. Eqs. (41a,b)]; J_0 and J_2 are the Bessel functions of order 0 and 2, respectively; $\beta = kr'$ $\sin\theta \sin\theta'$; and $r' = 2F/(1 + \cos\theta')$.

To enable comparison with the calculations made by Bach and Viskum[7,20] using a moment method, the reflector diameter and focal length were taken equal to 20 and 8 wavelengths, respectively, and two different feeds located at the reflector focus were used: a Hertzian x-directed electric dipole, and a Huygens source with an x-directed electric dipole and a y-directed magnetic dipole. The co- and cross-polarized field components, E_{co} and E_{cr}, were calculated from Eqs. (49a, b). In the results presented below, the amplitude and phase are normalized to the amplitude and phase, respectively, of the sum of the copolarized PO and nonuniform current field in the mainbeam direction of $\theta = 180°$.

First, we show the results of calculations in which the primary feed field is added to the secondary reflector field, as was done in the calculations of Bach and Viskum. Figures 3a, b, c show, respectively, the dipole-feed antenna (co-polar) amplitude pattern for θ from 180° to 155° in the E and H-planes (recall that the cross-polar field is zero in these planes), and the cross-polar amplitude pattern in the $\phi = 45°$ plane. Figures 4a, b, c show the corresponding phase patterns. Figures 5a, b, c show the same dipole-feed antenna amplitude patterns for θ from 180° to 0°, and Figures 6a, b, c show the corresponding phase patterns. Figures 7a, b, c through 10a, b, c show the corresponding amplitude and phase patterns for the Huygens-feed antenna. In all these patterns, the dashed line is the PO plus feed field, and the solid line is the sum of the PO, nonuniform current, and feed fields, so that the difference between the two curves is a measure of the importance of the nonuniform current field correction to the PO plus feed field.

Comparison of our total (PO plus nonuniform plus feed) field patterns with the corresponding patterns obtained by Bach and Viskum using a moment method, shown in Reference 7 as well as in a more detailed and complete set of curves,[20] shows very close agreement, in general, throughout. (Note that in Bach and Viskum the main beam direction is given by $\theta = 0°$, and an exp($j\omega t$) time dependence is used, so that their phases are the negative of ours.) As an example we have reproduced in Figure 11 the cross-polar amplitude patterns in the $\phi = 45°$ plane obtained by Bach and Viskum[20] for the Huygens-feed reflector antenna. Comparing Figure 11 with Figure 7c it is seen that the levels of the sidelobe peaks of our total field pattern agree closely with those of Bach and Viskum's method of moments pattern. Our null depths are somewhat deeper than theirs, however. [This discrepancy in cross-polar null depths for the Huygens source may be caused by the limited dynamic range of the method of moments program,[20] because the cross-polarized field in the 45° plane is the difference between the E- and H-plane fields see Eq. (49b), and the E- and H-plane fields for the Huygens source are especially close in the forward region from 0° to 25° shown in Figures 7c and 11.]
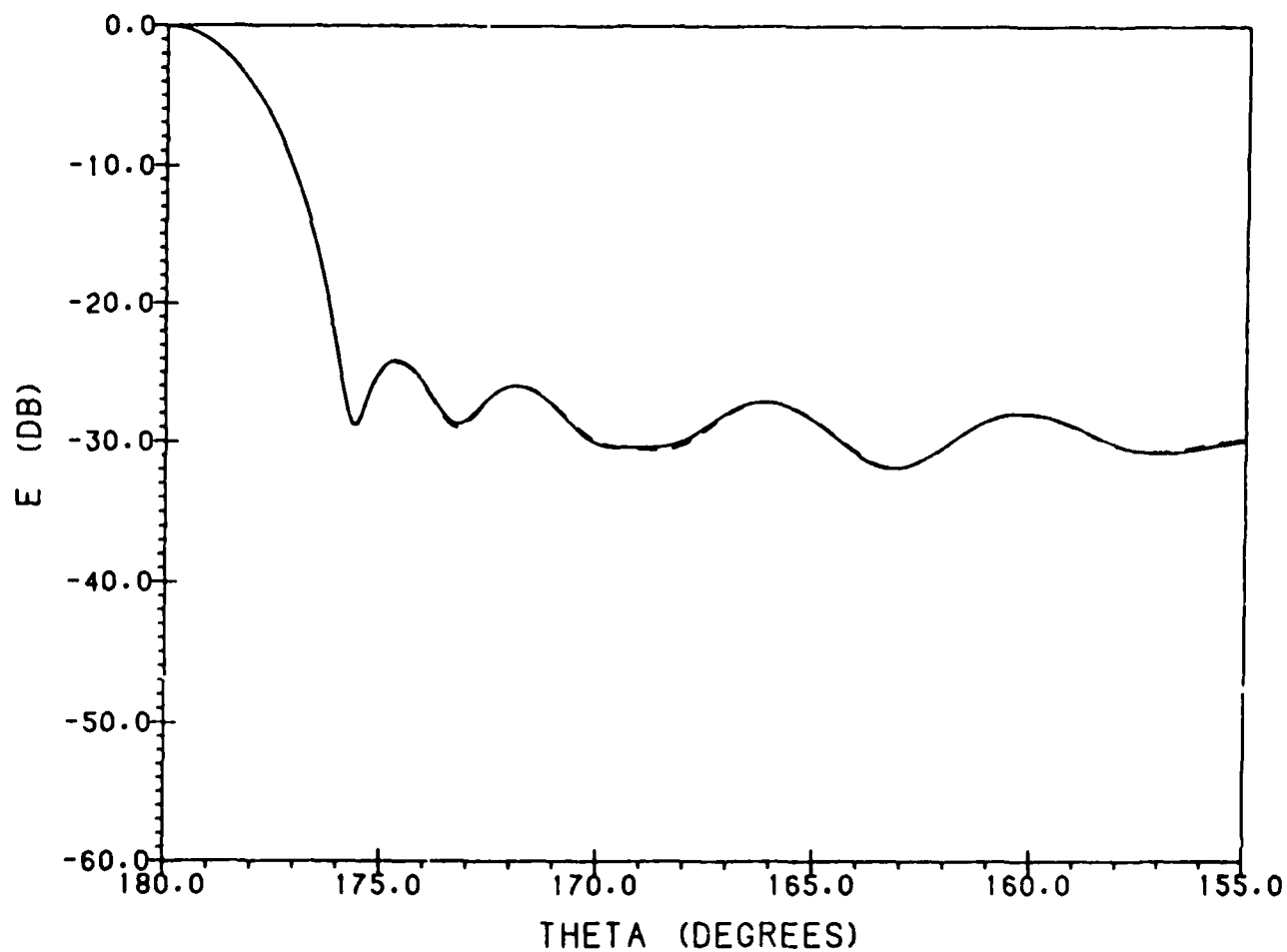
Figure 3a. E-Plane Amplitude Pattern of 20λ Dipole-Feed Paraboloid Antenna With Primary Field Included; — — — — PO, ———— PO + Nonuniform Current Field, F/D = 0.4, θ = [180°, 155°]
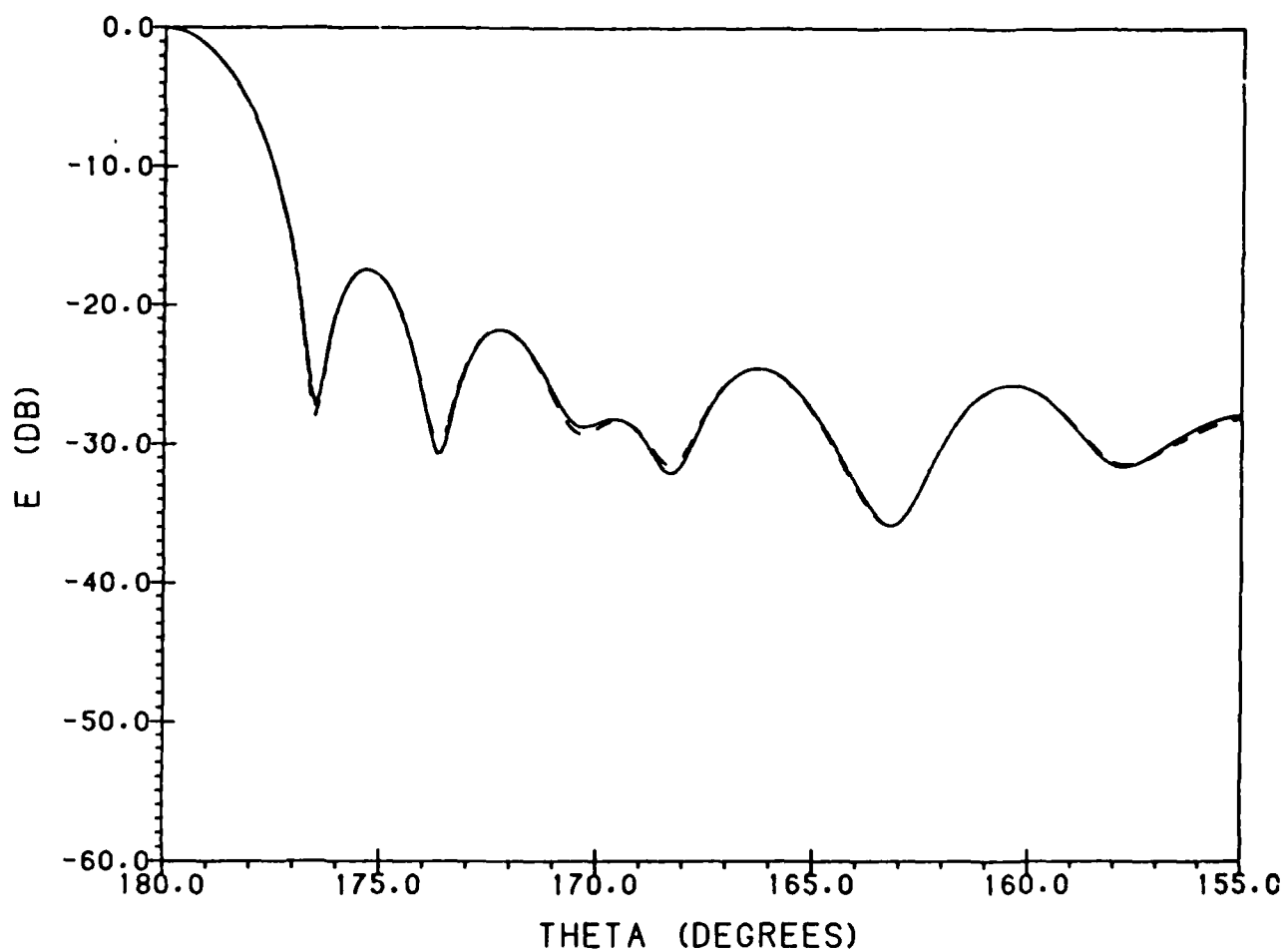
Figure 3b. H-Plane Amplitude Pattern of 20λ Dipole-Feed Paraboloid Antenna With Primary Field Included; – – – – PO, ——— PO + Nonuniform Current Field, F/D = 0.4, θ = [180°, 155°]
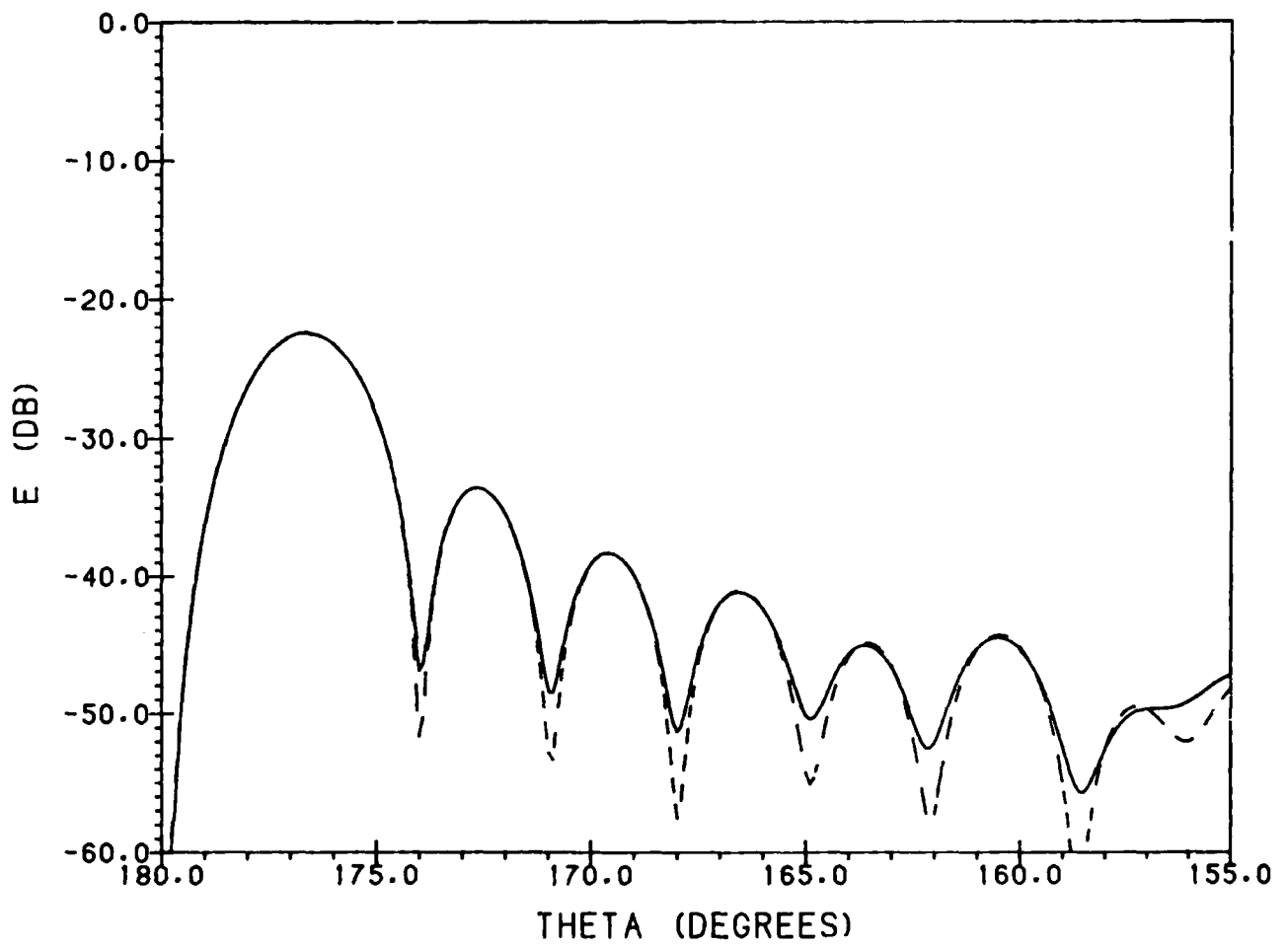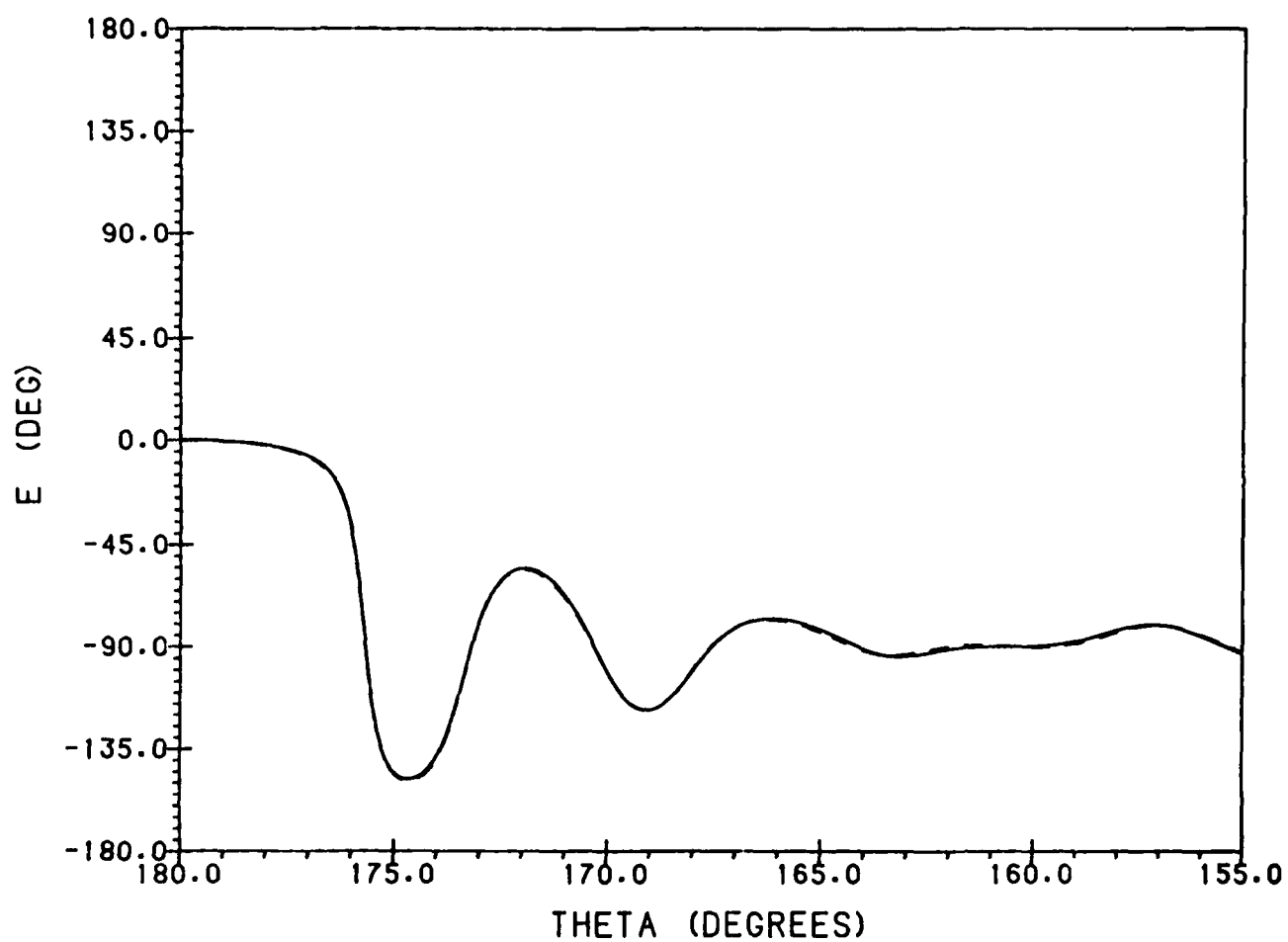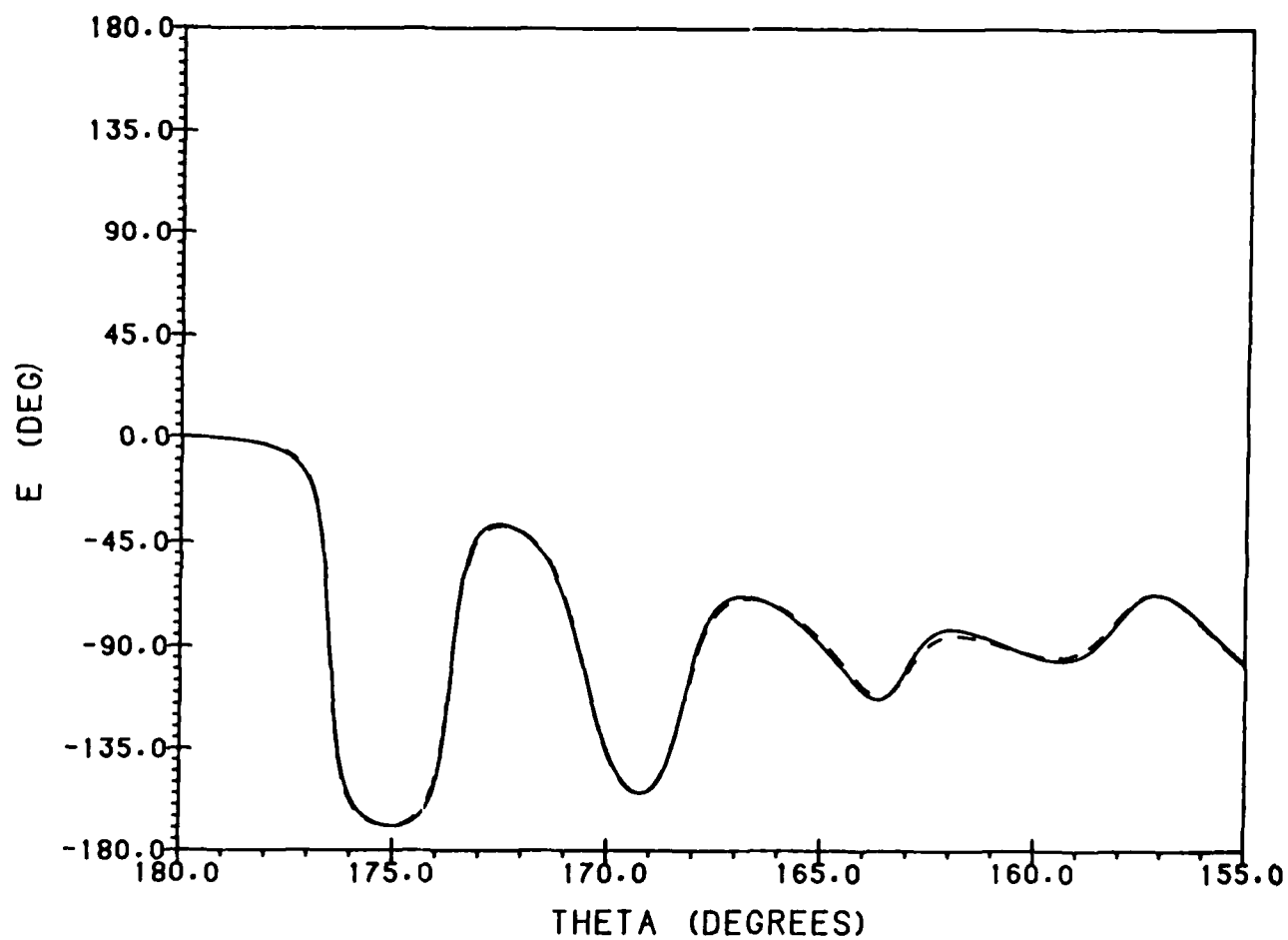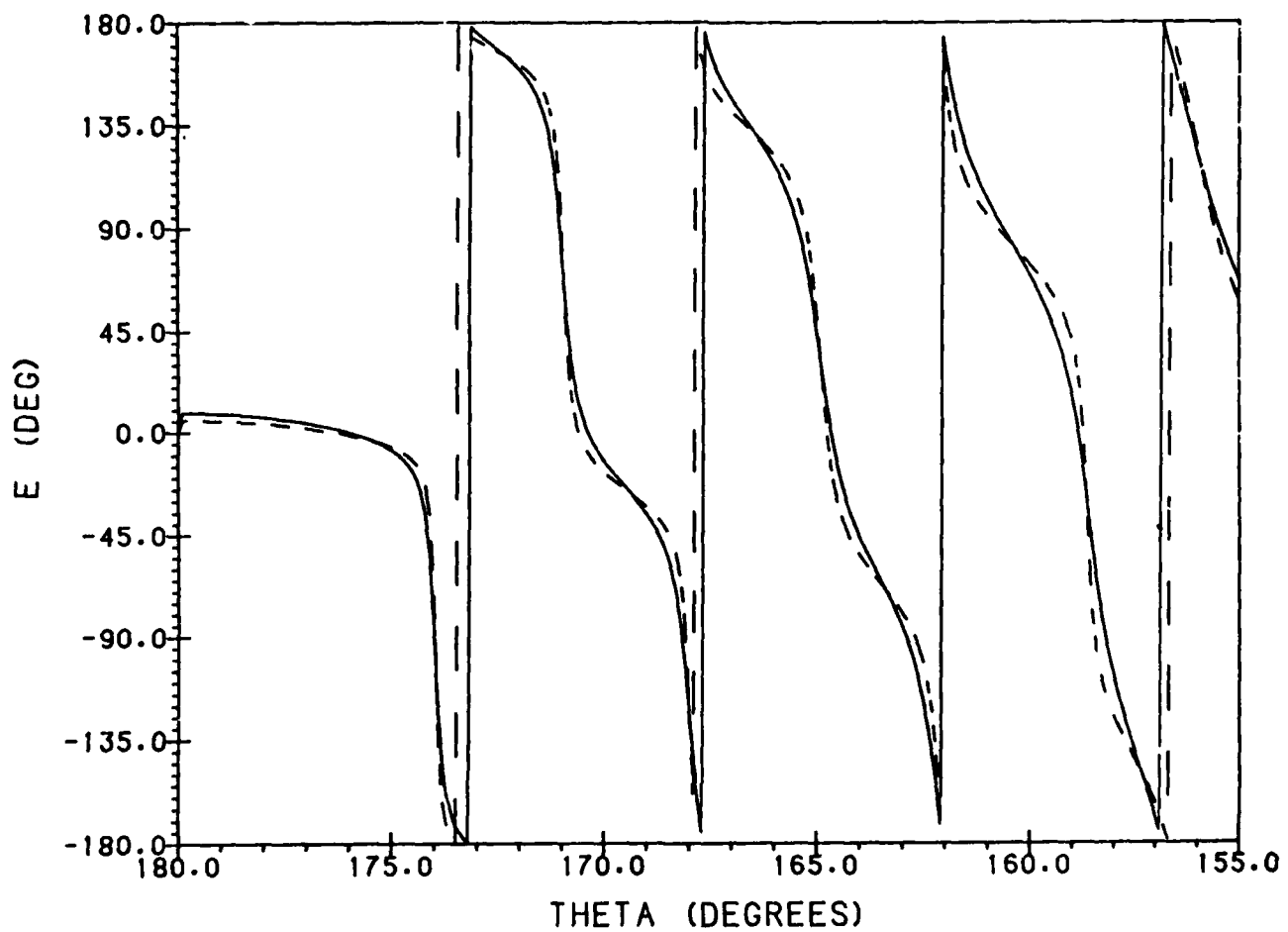
Figure 3c. $\phi = 45°$ Cross-Polar Amplitude Pattern of 20λ Dipole-Feed Paraboloid Antenna With Primary Field Included; ---- PO, ———— PO + Nonuniform Current Field, F/D = 0.4, θ = [180°, 150°]

19

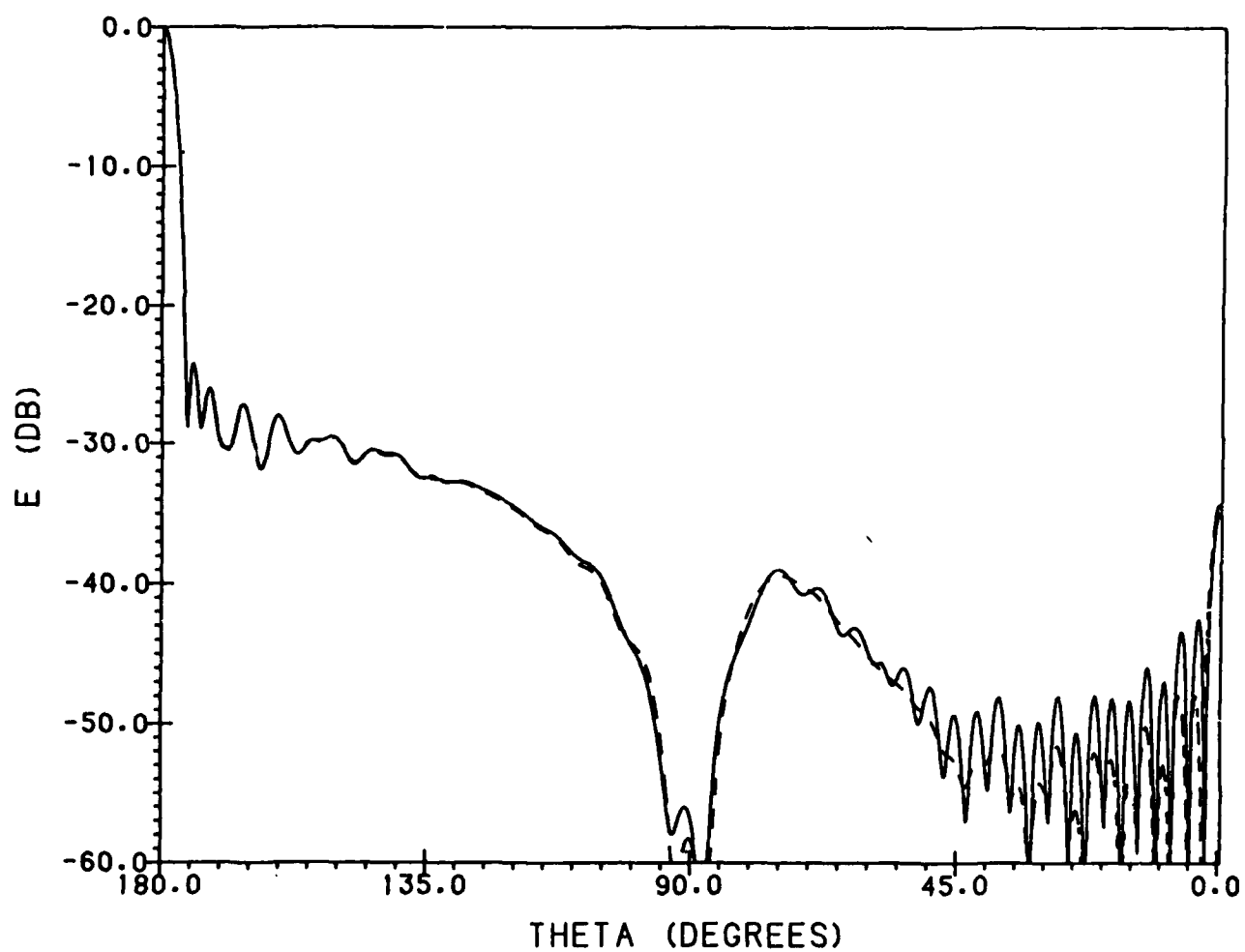Figure 4a. E-Plane Phase Pattern of 20λ Dipole-Feed Paraboloid Antenna With Primary Field Included; ---- PO, ——— PO + Nonuniform Current Field, F/D = 0.4, θ = [180°, 155°]
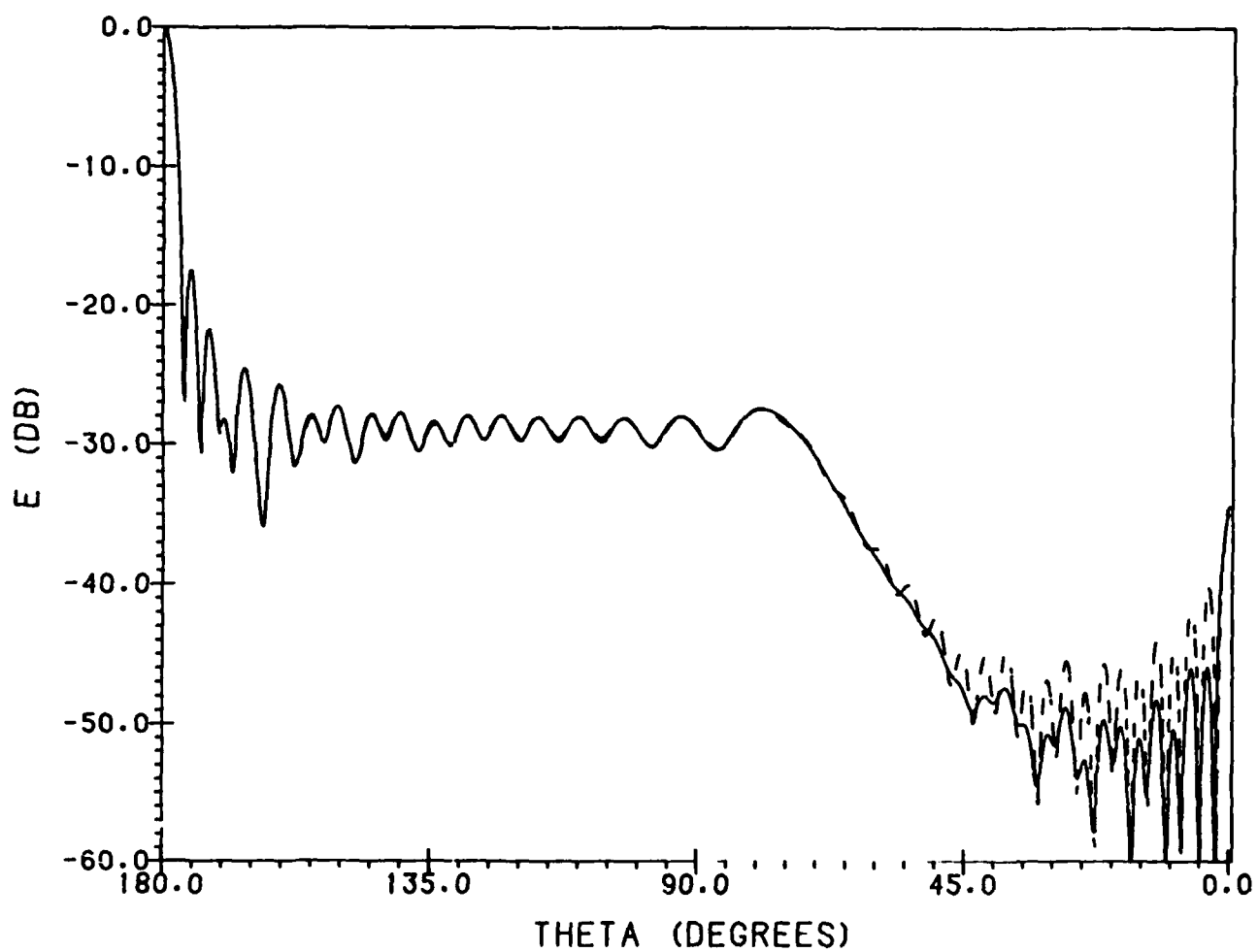
Figure 4b. H-Plane Phase Pattern of 20λ Dipole-Feed Paraboloid Antenna With Primary Field Included;
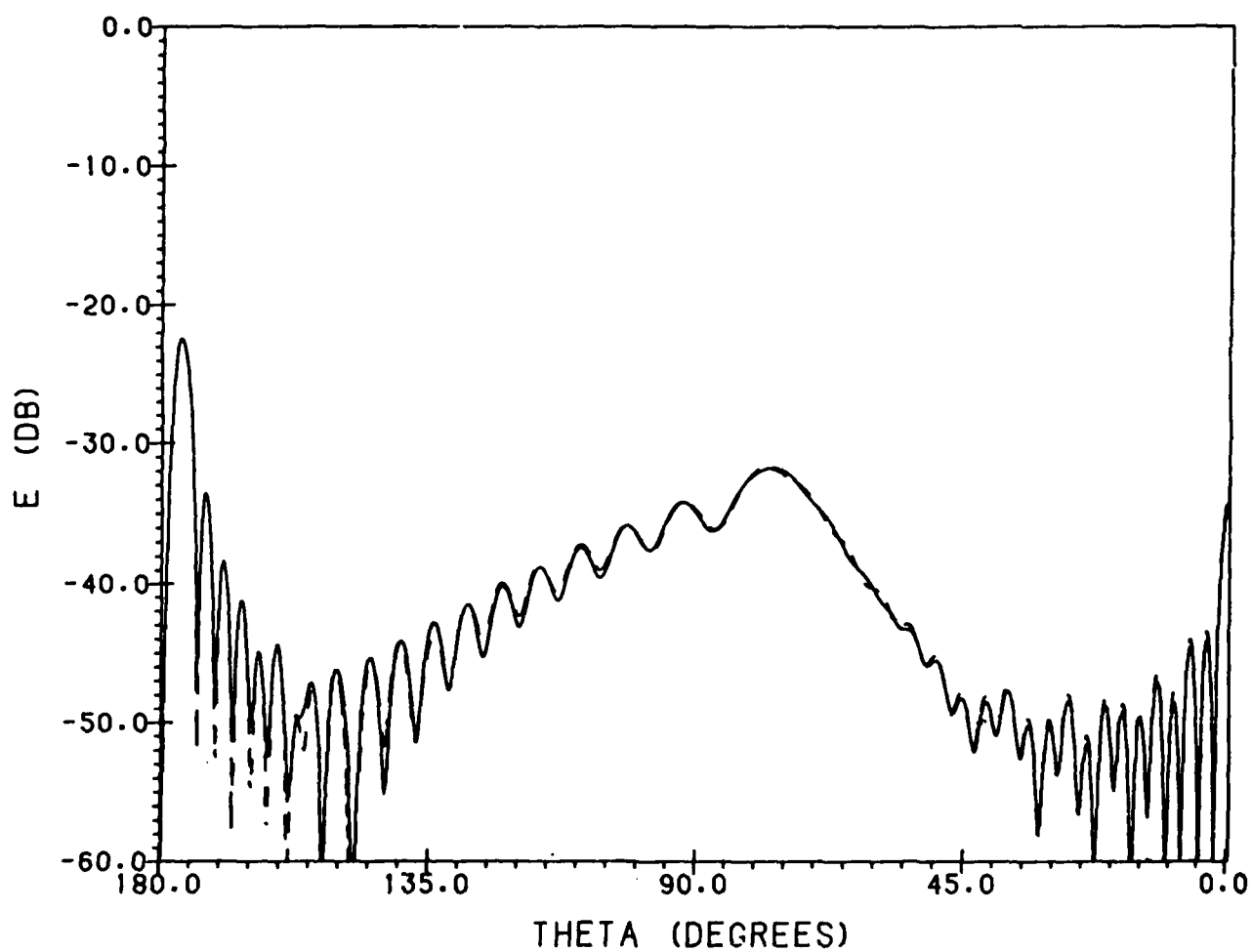— — — — PO, ——— PO + Nonuniform Current Field, F/D = 0.4, θ = [180°, 155°]

Figure 4c. ϕ = 45° Cross-Polar Phase Pattern of 20λ Dipole-Feed Paraboloid Antenna With Primary Field Included; – – – – PO, ———— PO + Nonuniform Current Field, F/D = 0.4, θ = [180°, 155°]
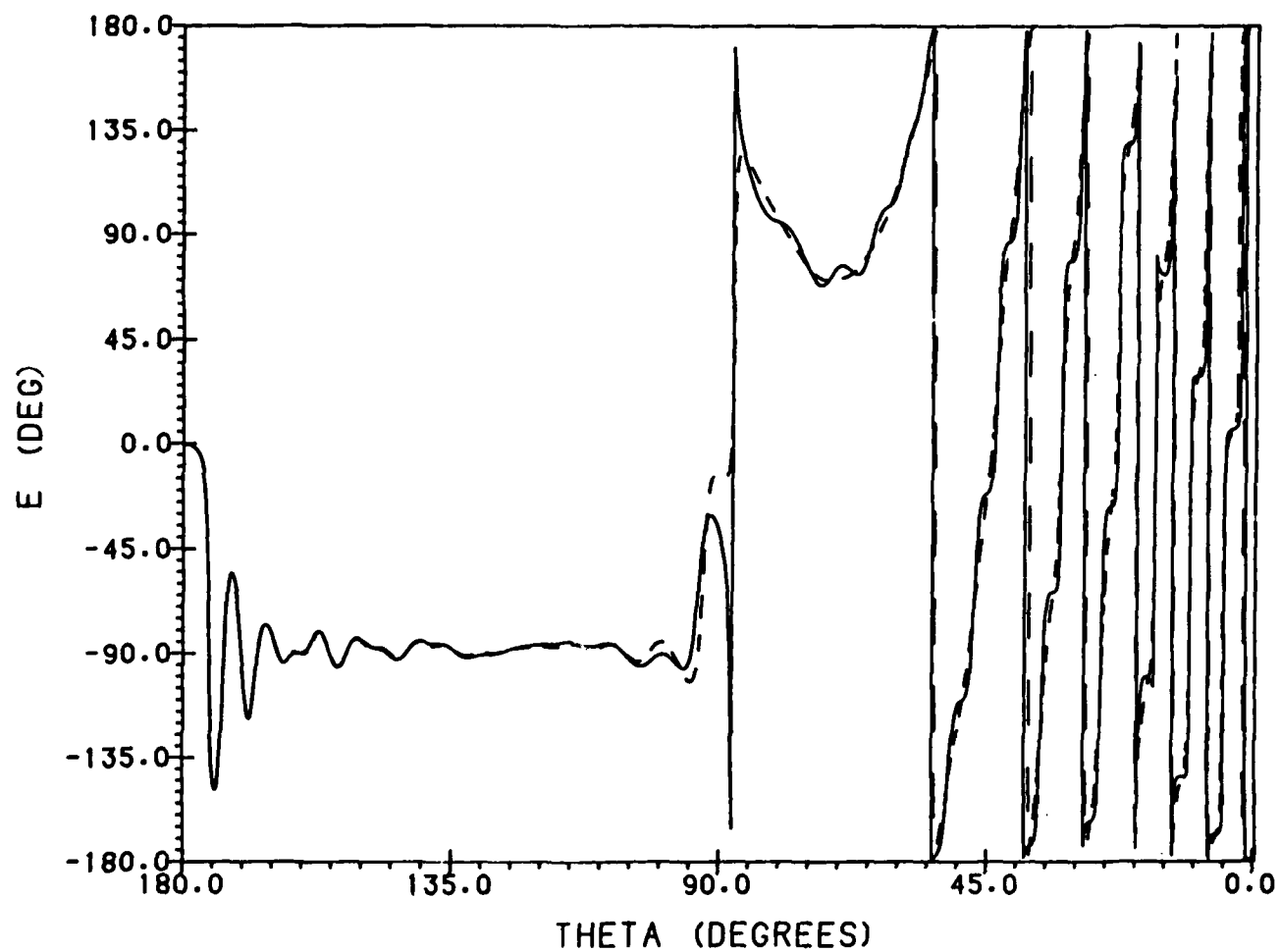
Figure 5a. E-Plane Amplitude Pattern of 20λ Dipole-Feed Paraboloid Antenna With Primary Field Included; ---- PO, ———— PO + Nonuniform Current Field, F/D = 0.4, θ = [180°, 0°]

23

Figure 5b. H-Plane Amplitude Pattern of 20λ Dipole-Feed Paraboloid Antenna With Primary Field Included; – – – – PO, ———— PO + Nonuniform Current Field, F/D = 0.4, θ = [180°, 0°]

24

Figure 5c. φ = 45° Cross-Polar Amplitude Pattern of 20λ Dipole-Feed Paraboloid Antenna With Primary Field Included; – – – – PO, ———— PO + Nonuniform Current Field, F/D = 0.4, θ = [180°, 0°]

Figure 6a. E-Plane Phase Pattern of 20λ Dipole-Feed Paraboloid Antenna With Primary Field Included; ‒ ‒ ‒ ‒ PO, ────── PO + Nonuniform Current Field, F/D = 0.4, θ = [180°, 0°]
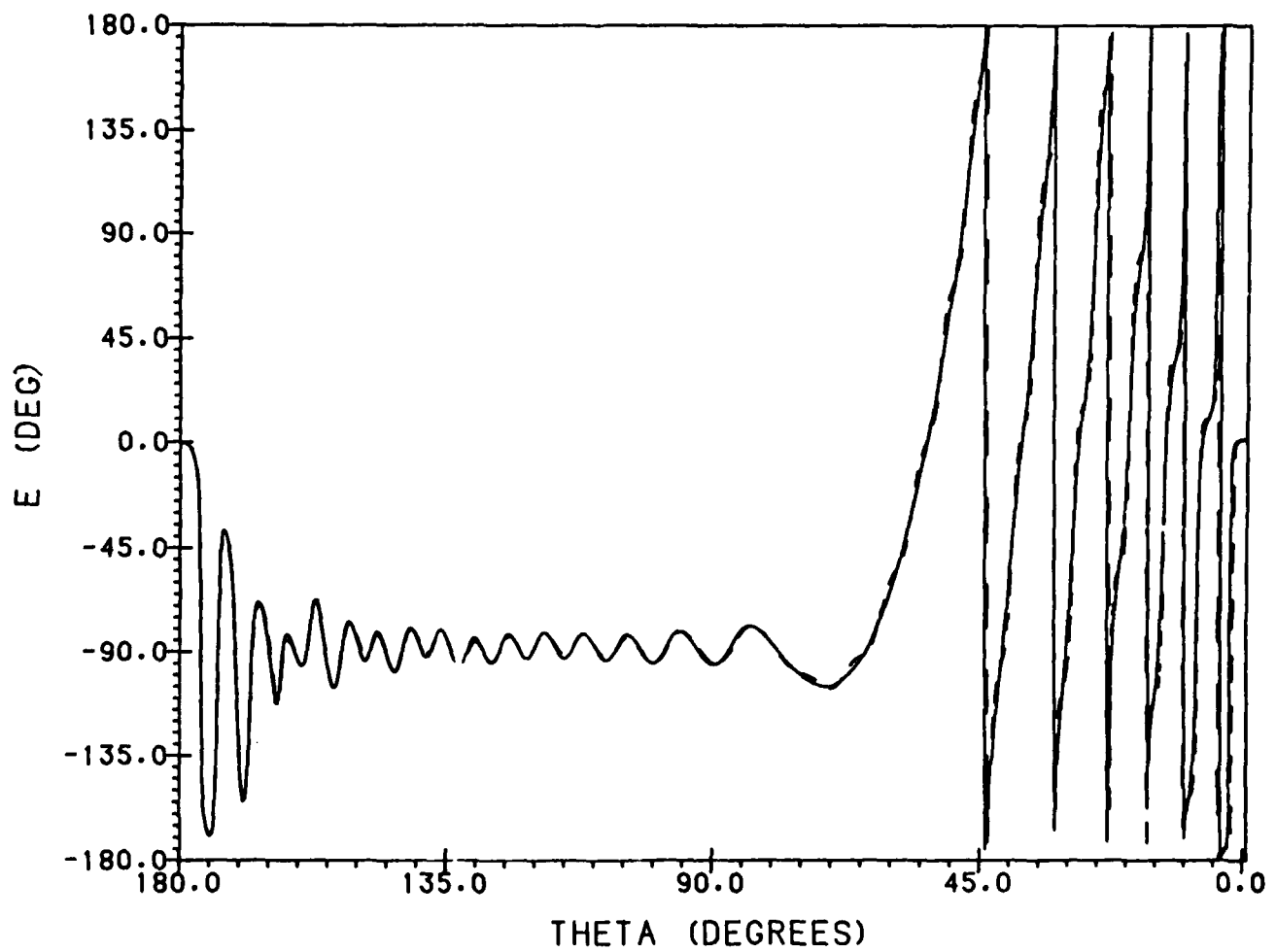
Figure 6b. H-Plane Phase Pattern of 20λ Dipole-Feed Paraboloid Antenna With Primary Field Included; ---- PO, ——— PO + Nonuniform Current Field, F/D = 0.4, θ = [180°, 0°]
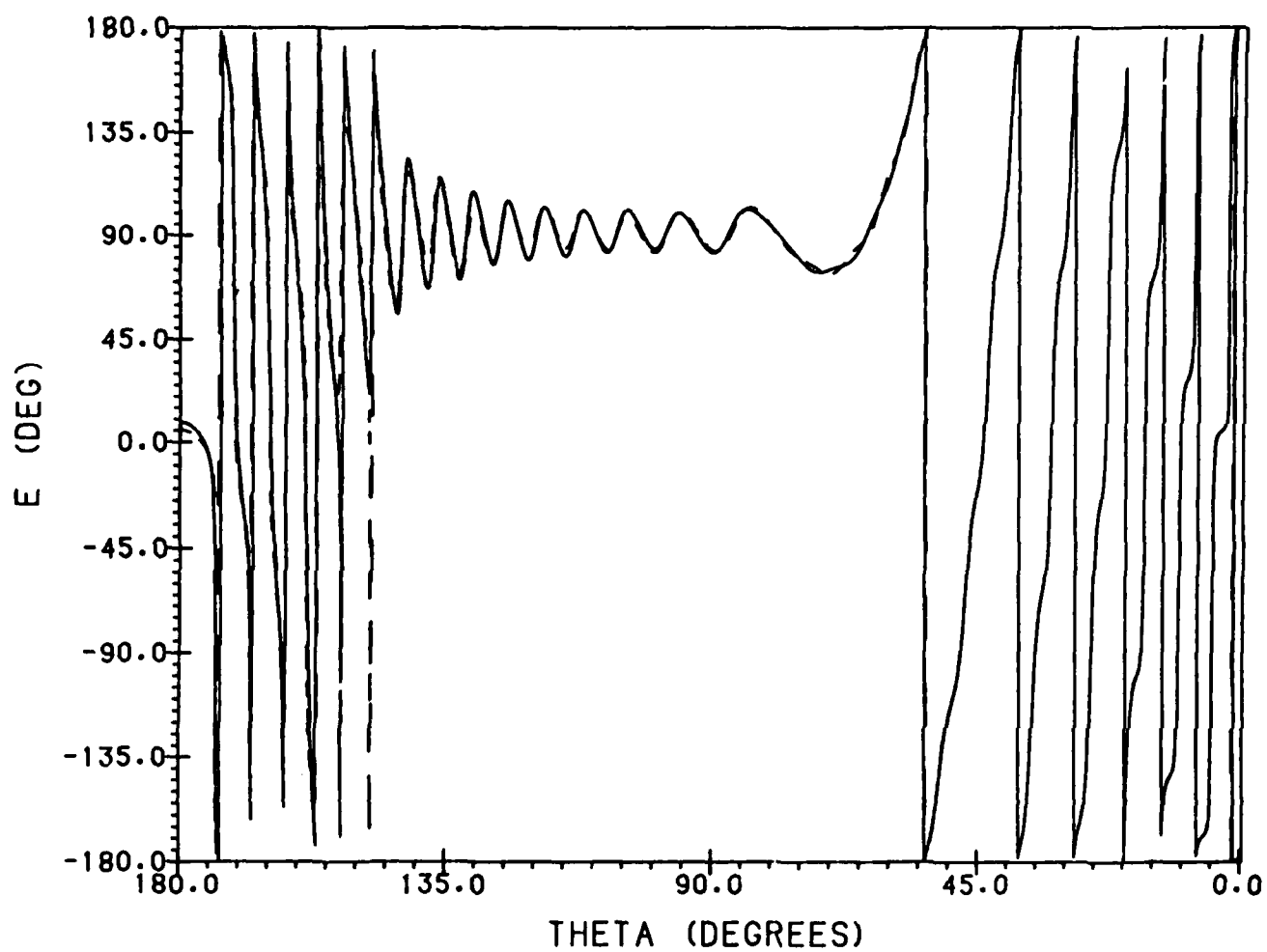
Figure 6c. φ = 45° Cross-Polar Phase Pattern of 20λ Dipole-Feed Paraboloid Antenna With Primary Field Included; − − − − PO, ———— PO + Nonuniform Current Field, F/D = 0.4, θ ≈ [180°, 0°]

Figure 7a. E-Plane Amplitude Pattern of 20λ Huygens-Feed Paraboloid Antenna With Primary Field Included; ─ ─ ─ ─ PO, ────── PO + Nonuniform Current Field, F/D = 0.4, θ = [180°, 155°]
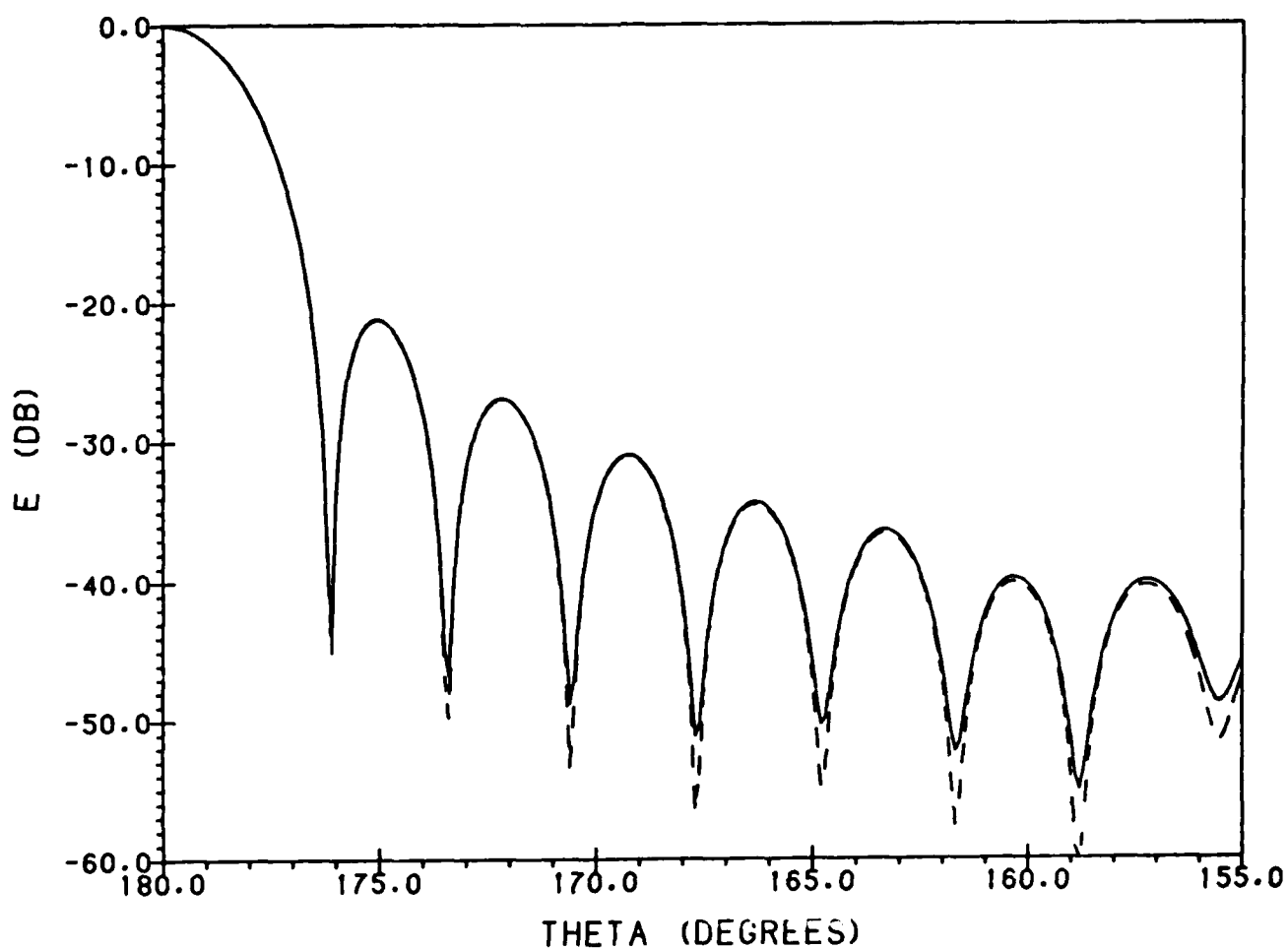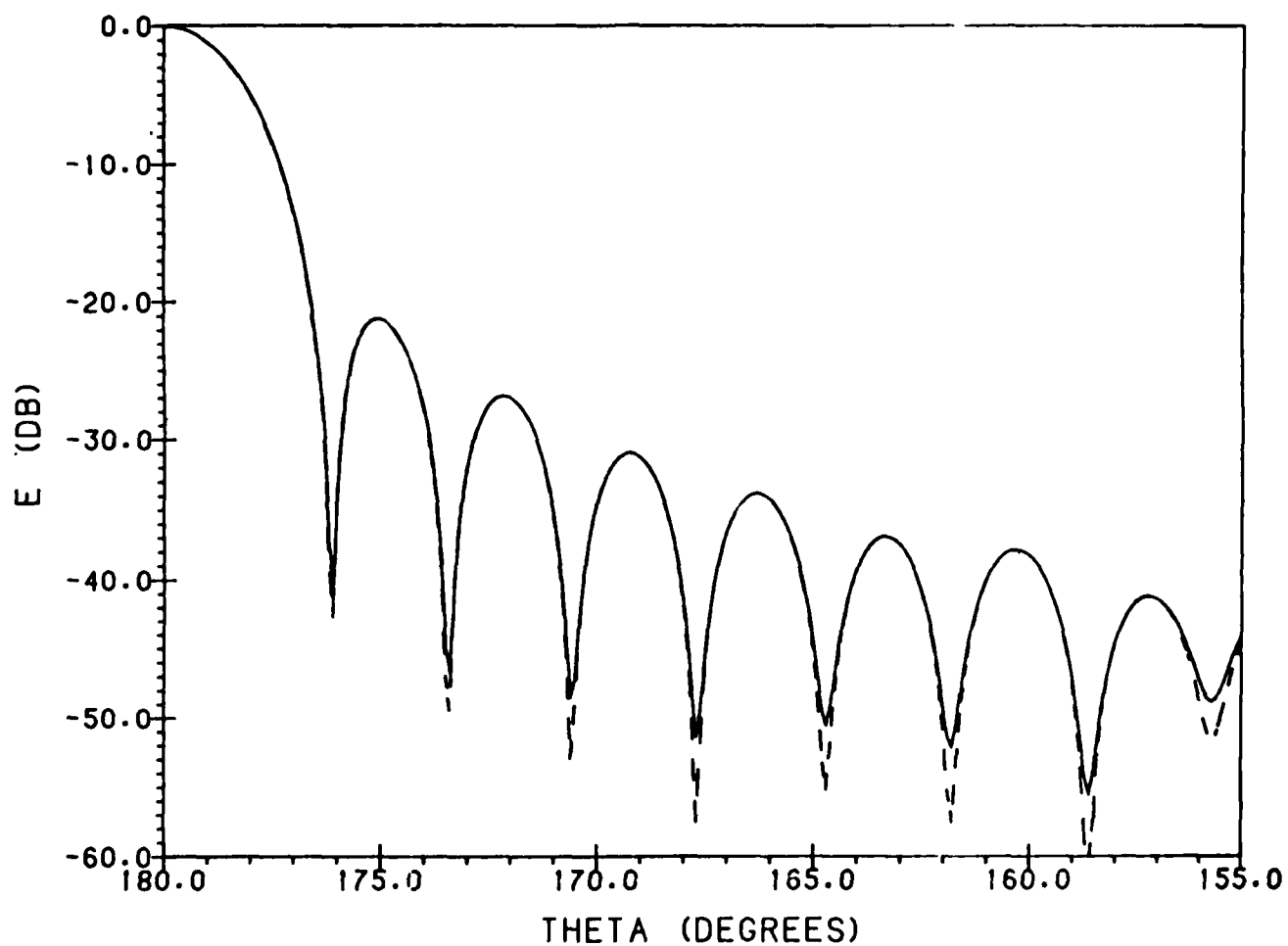
Figure 7b. H-Plane Amplitude Pattern of 20λ Huygens-Feed Paraboloid Antenna With Primary Field Included; – – – – PO, ———— PO + Nonuniform Current Field, F/D = 0.4, θ = [180°, 155°]
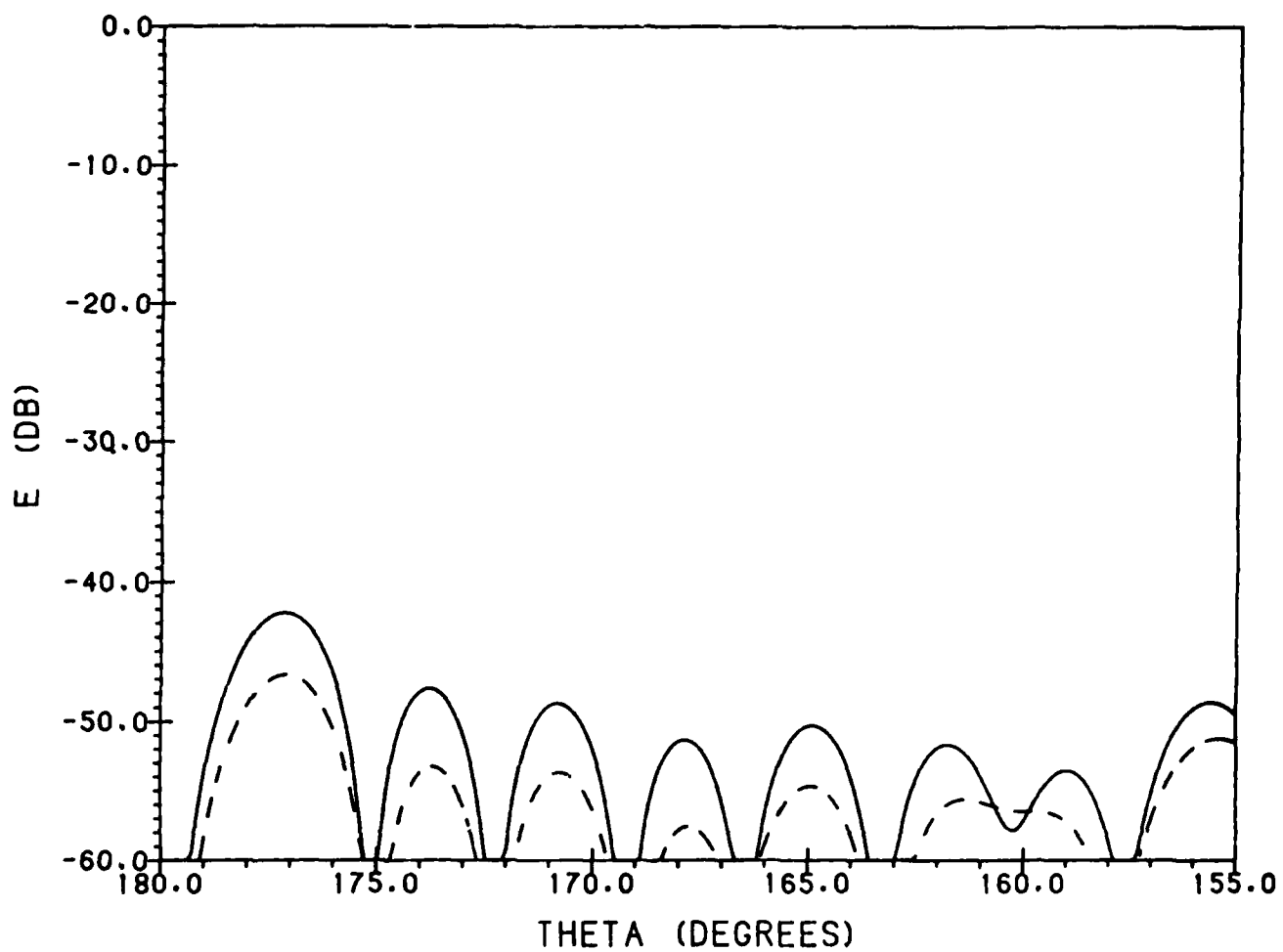
Figure 7c. $\phi = 45°$ Cross-Polar Amplitude Pattern of 20λ Huygens-Feed Paraboloid Antenna With Primary Field Included; – – – – PO, ———— PO + Nonuniform Current Field, F/D = 0.4, θ = [180°, 155°]
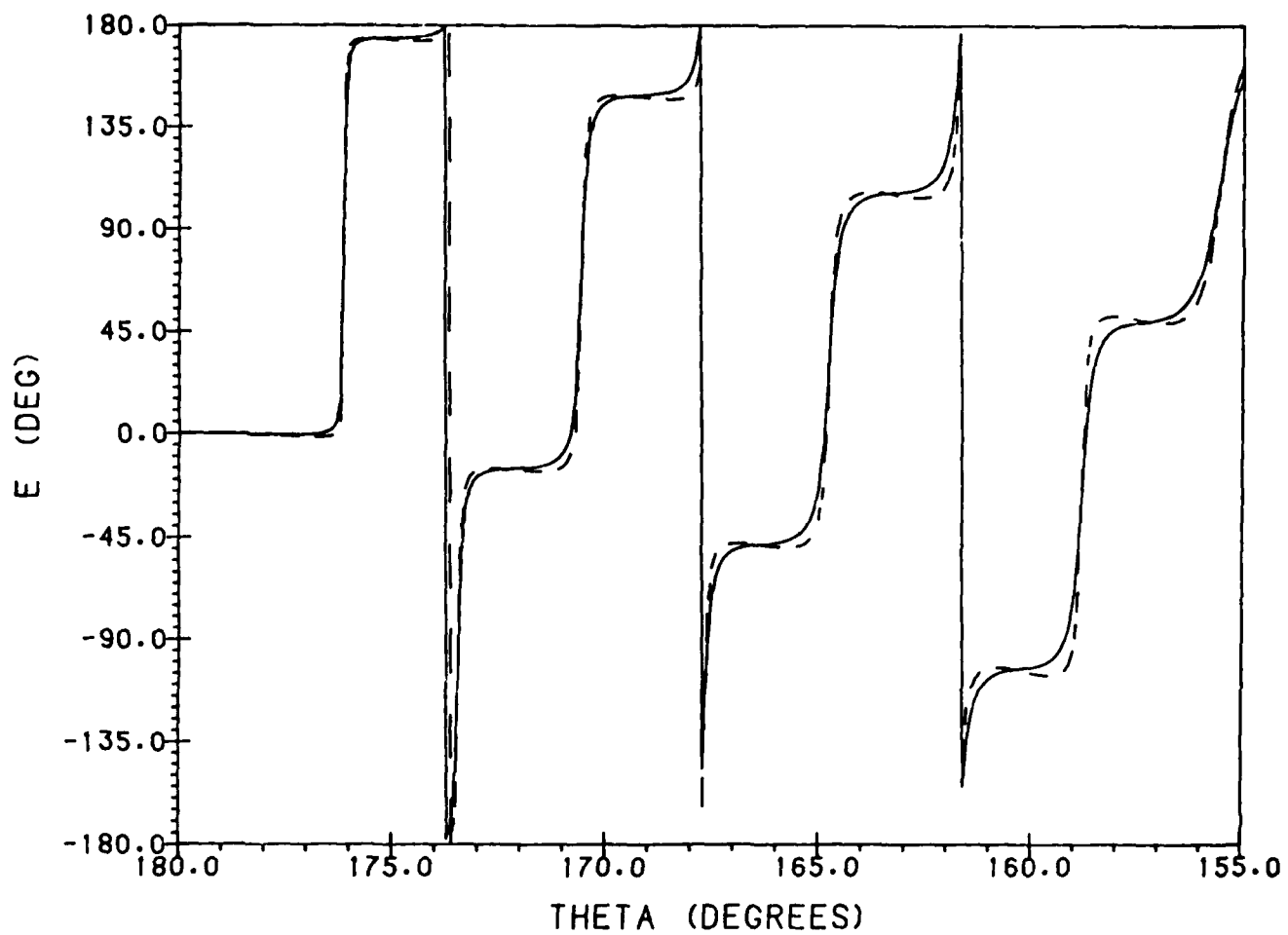
Figure 8a. E-Plane Phase Pattern of 20λ Huygens-Feed Paraboloid Antenna With Primary Field Included; ---- PO, ———— PO + Nonuniform Current Field, F/D = 0.4, θ = [180°, 155°]
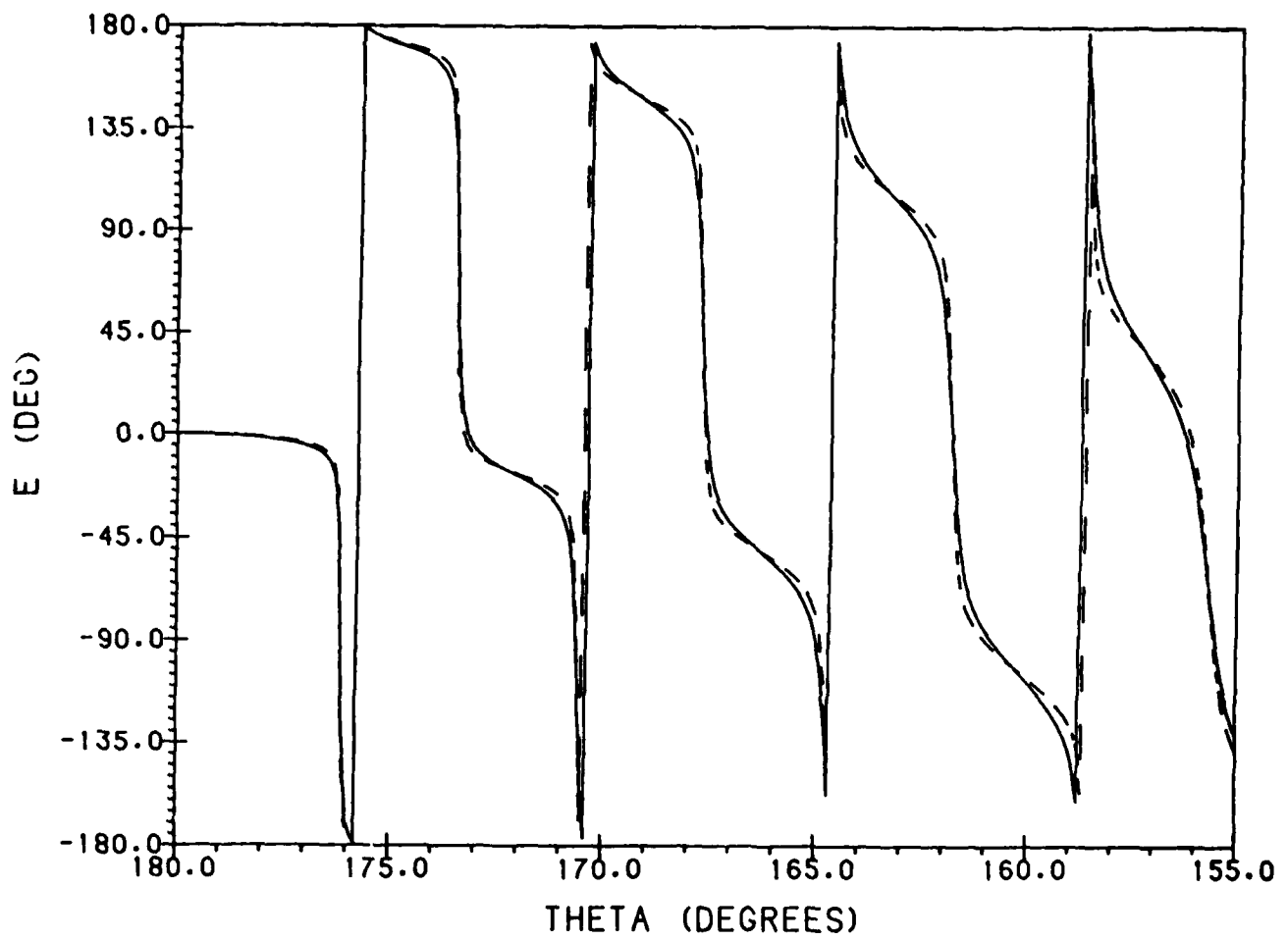
32

Figure 8b. H-Plane Phase Pattern of 20λ Huygens-Feed Paraboloid Antenna With Primary Field Included; ─ ─ ─ ─ PO, ───── PO + Nonuniform Current Field, F/D = 0.4, θ = [180°, 155°]

Figure 8c. ϕ = 45° Cross-Polar Phase Pattern of 20λ Huygens-Feed Paraboloid Antenna With Primary Field Included; ---- PO, ———— PO + Nonuniform Current Field, F/D = 0.4, θ = [180°, 155°]
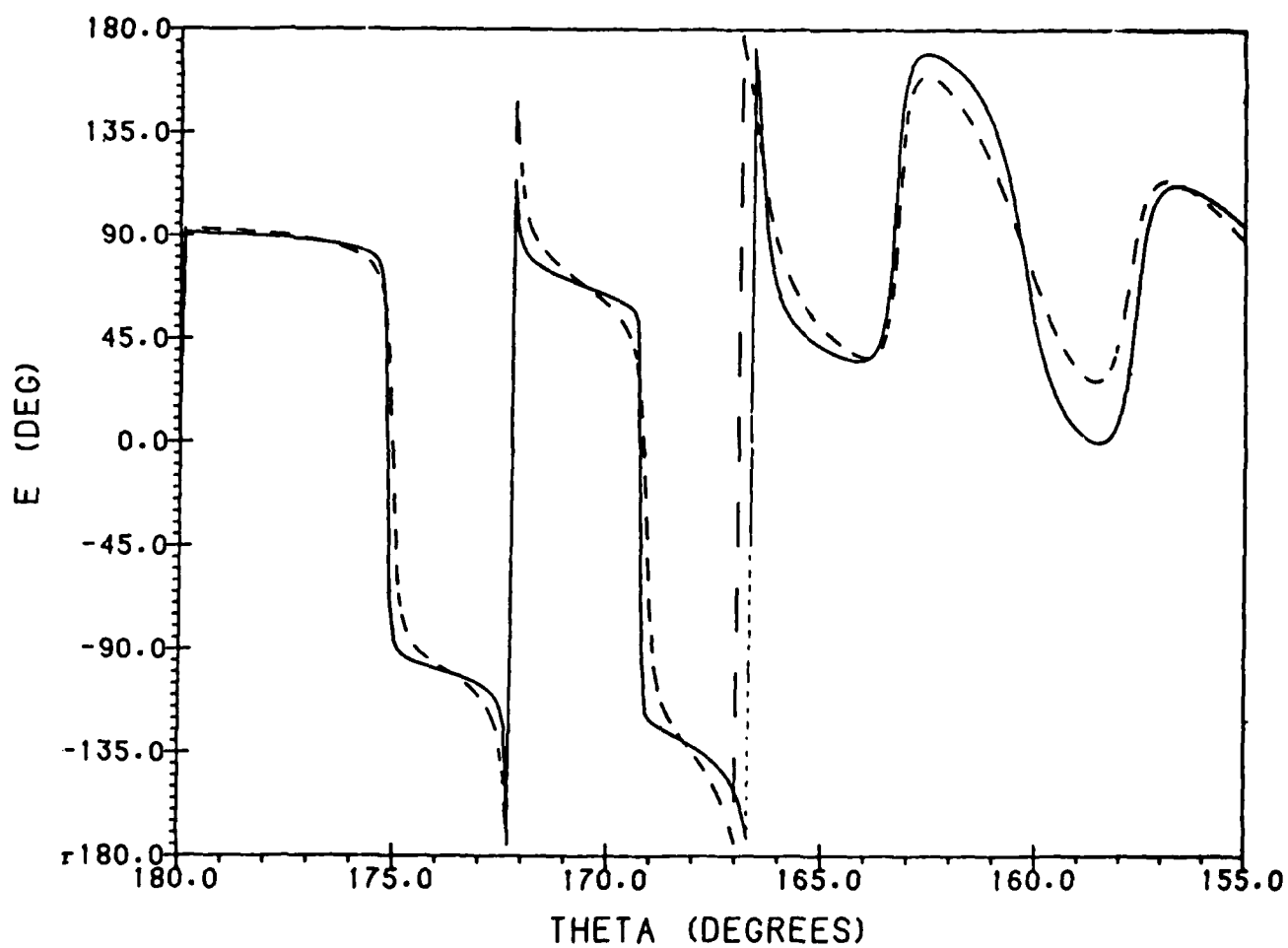
Figure 9a. E-Plane Amplitude Pattern of 20λ Huygens-Feed Paraboloid Antenna With Primary Field Included;
− − − − PO, ———— PO + Nonuniform Current Field, F/D = 0.4, θ = [180°, 0°]

Figure 9b. H-Plane Amplitude Pattern of 20λ Huygens-Feed Paraboloid Antenna With Primary Field Included; – – – – PO, ———— PO + Nonuniform Current Field, F/D = 0.4, θ = [180°, 0°]

36
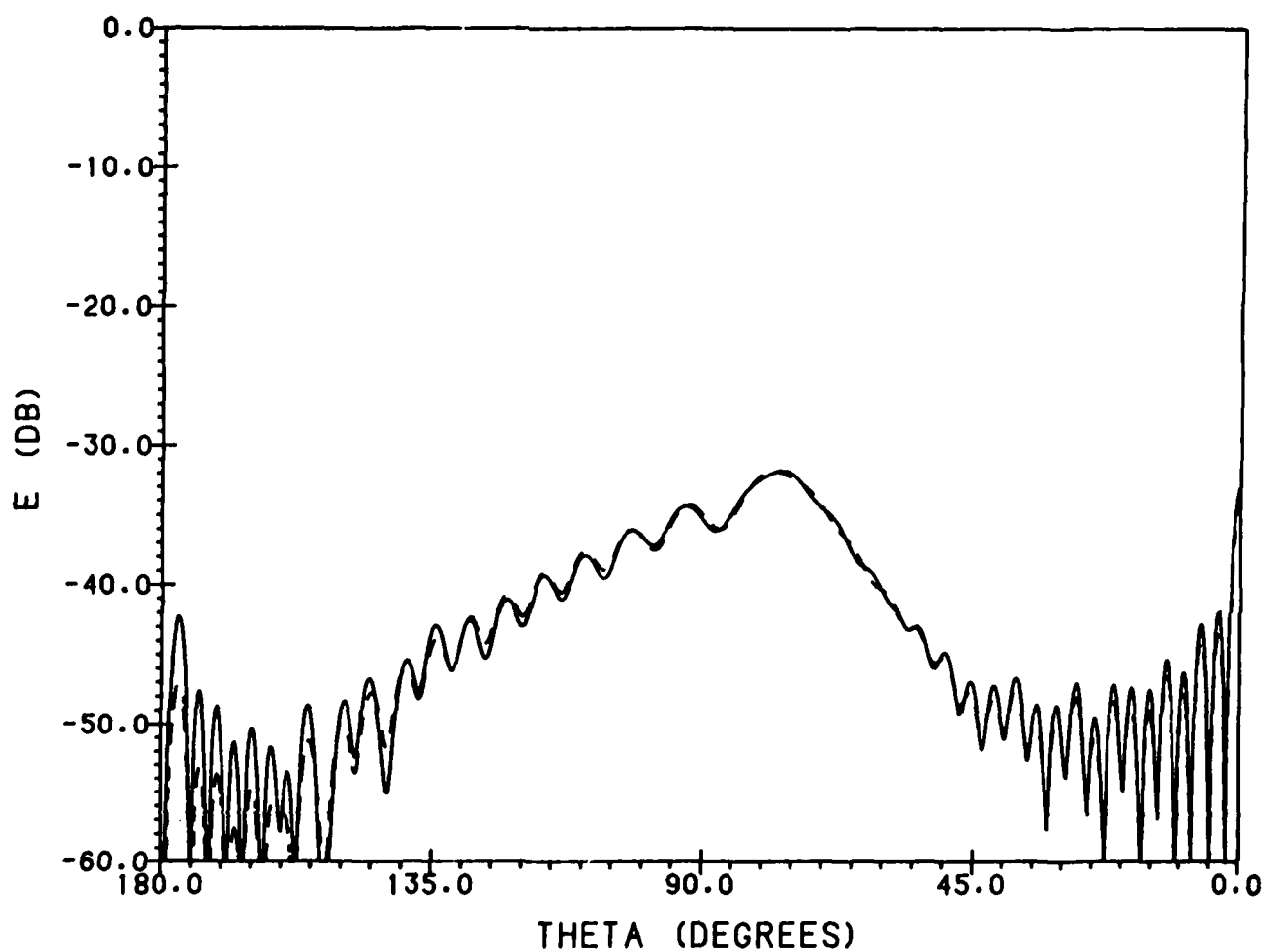
Figure 9c. $\phi = 45°$ Cross-Polar Amplitude Pattern of 20λ Huygens-Feed Paraboloid Antenna With Primary Field Included; – – – – PO, ———— PO + Nonuniform Current Field, F/D = 0.4, θ = [180°, 0°]
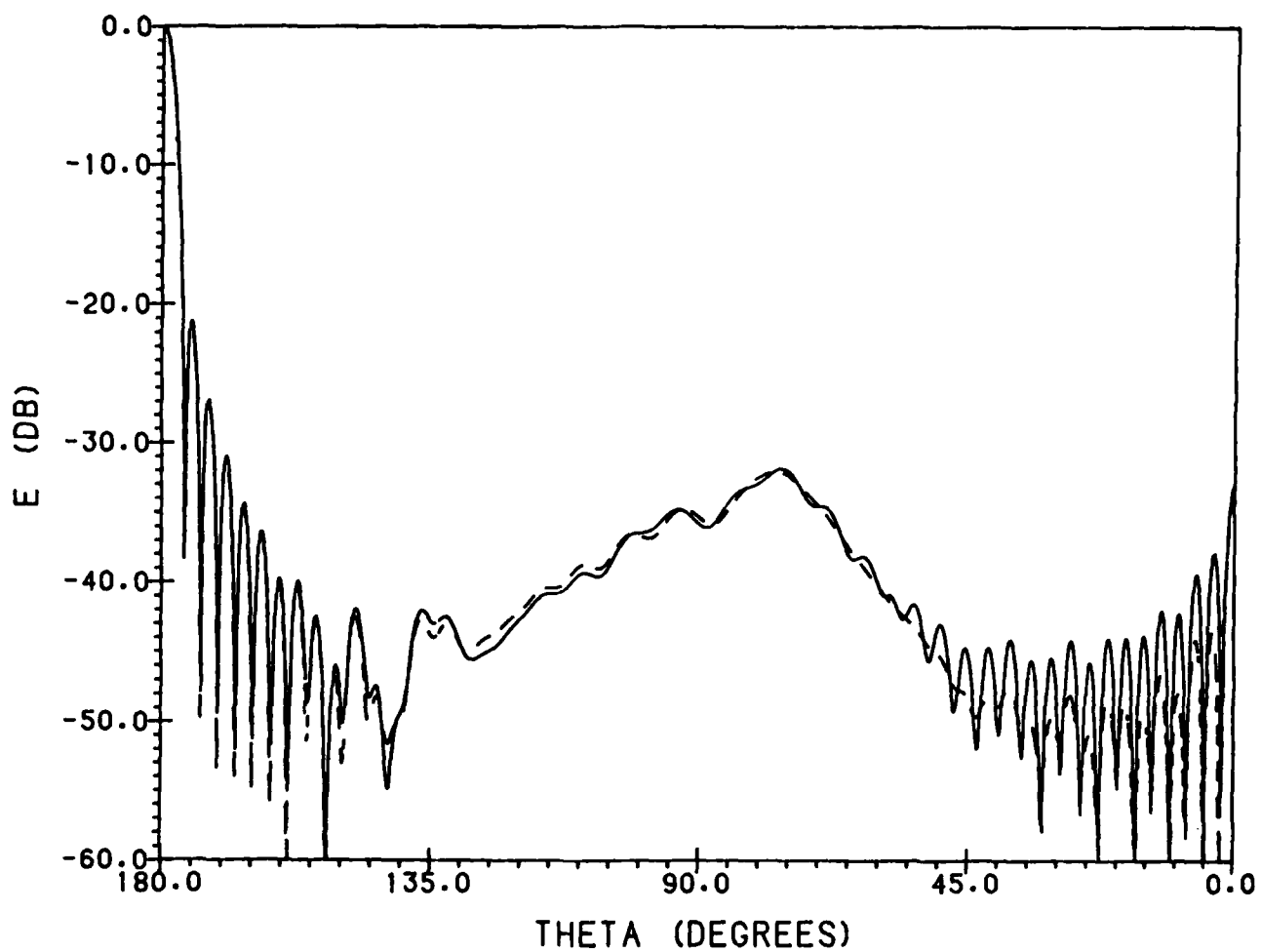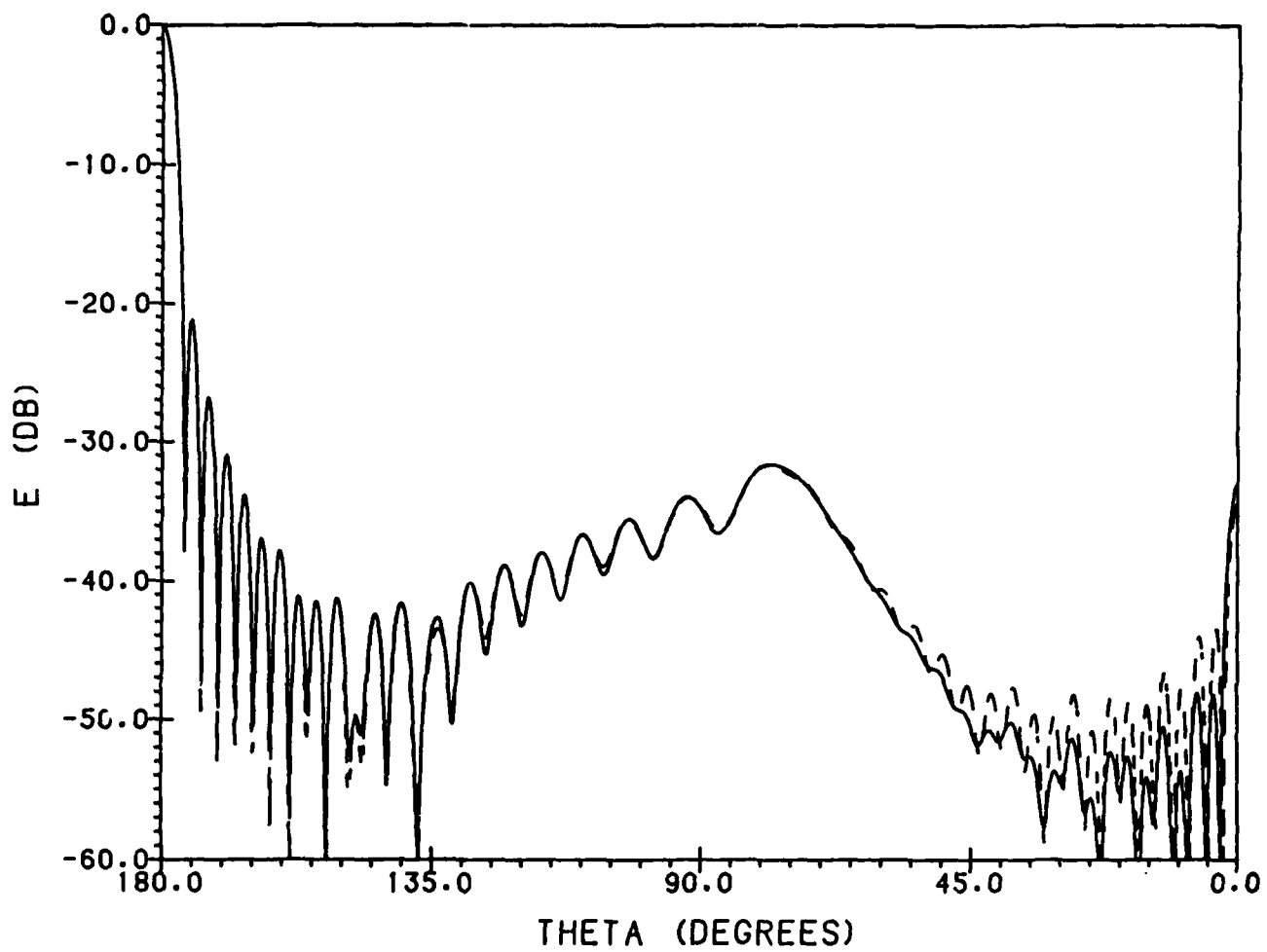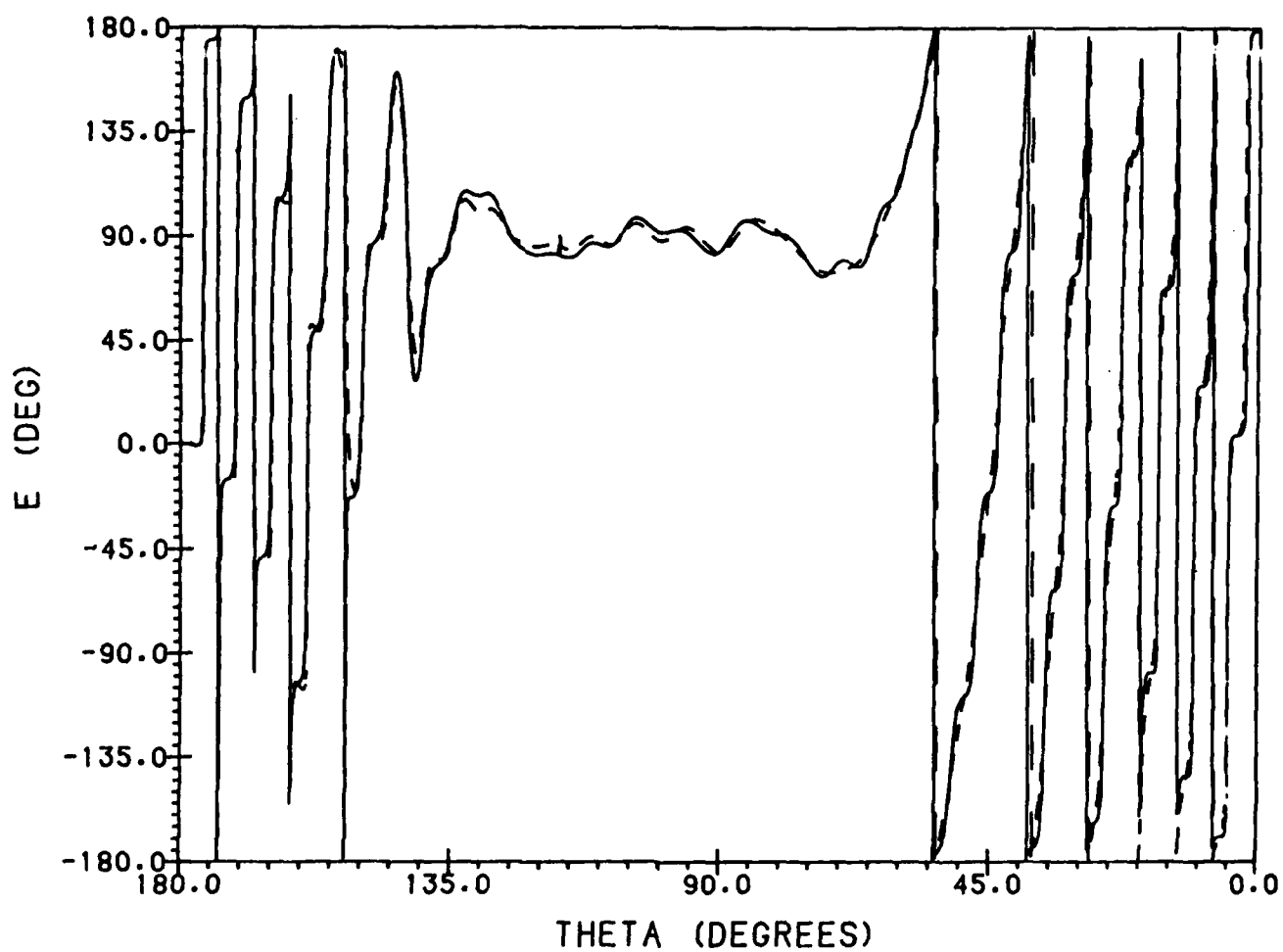
Figure 10a. E-Plane Phase Pattern of 20λ Huygens-Feed Paraboloid Antenna With Primary Field Included; ---- PO, —— PO + Nonuniform Current Field, F/D = 0.4, θ = [180°, 0°]

38

Figure 10b. H-Plane Phase Pattern of 20λ Huygens-Feed Paraboloid Antenna With Primary Field Included; − − − − PO, ——— PO + Nonuniform Current Field, F/D = 0.4, θ = [180°, 0°]

Figure 10c. φ = 45° Cross-Polar Phase Pattern of 20λ Huygens-Feed Paraboloid Antenna With Primary Field Included; — — — — PO, ————— PO + Nonuniform Current Field, F/D = 0.4, θ = [180°, 0°]

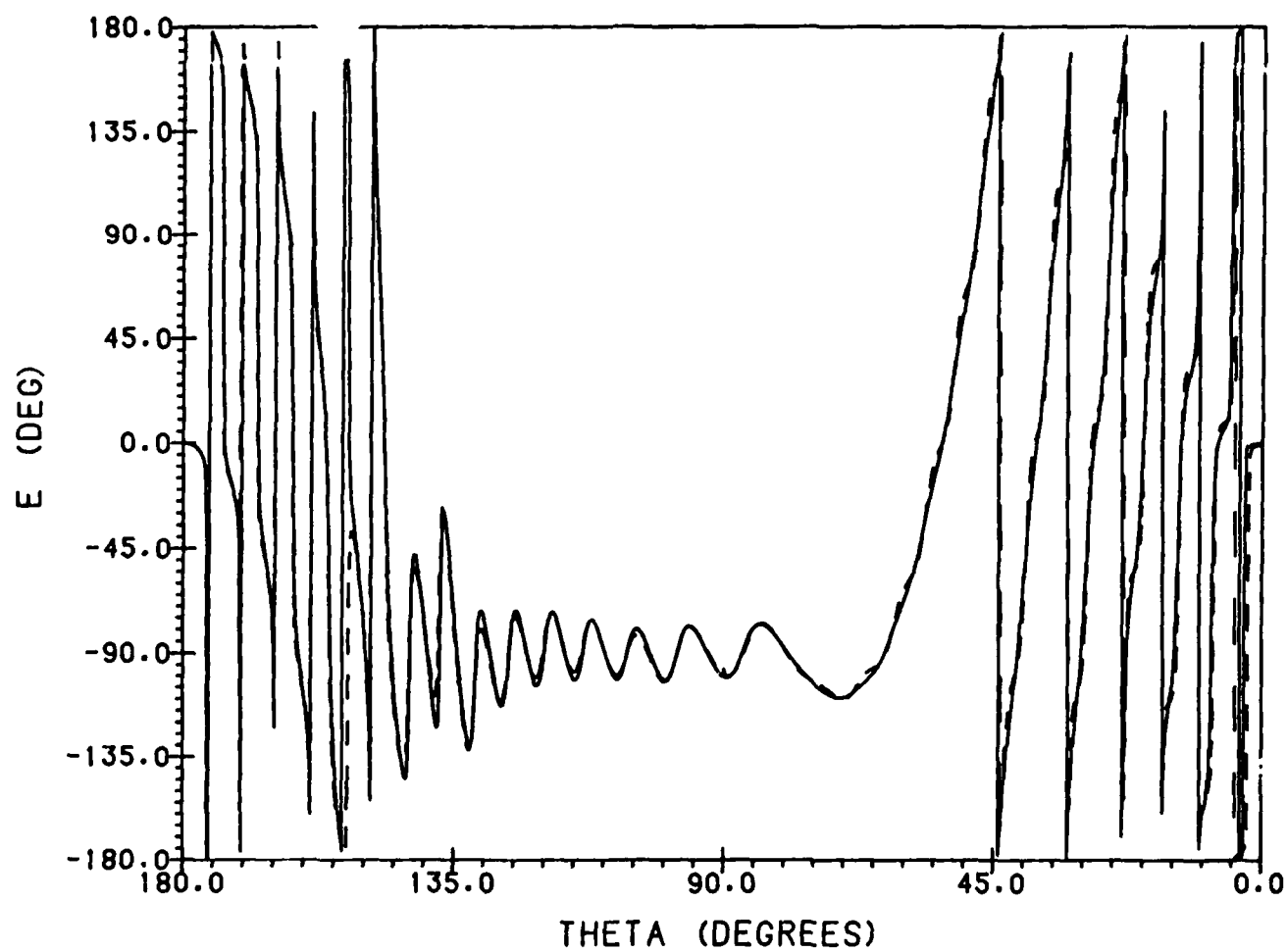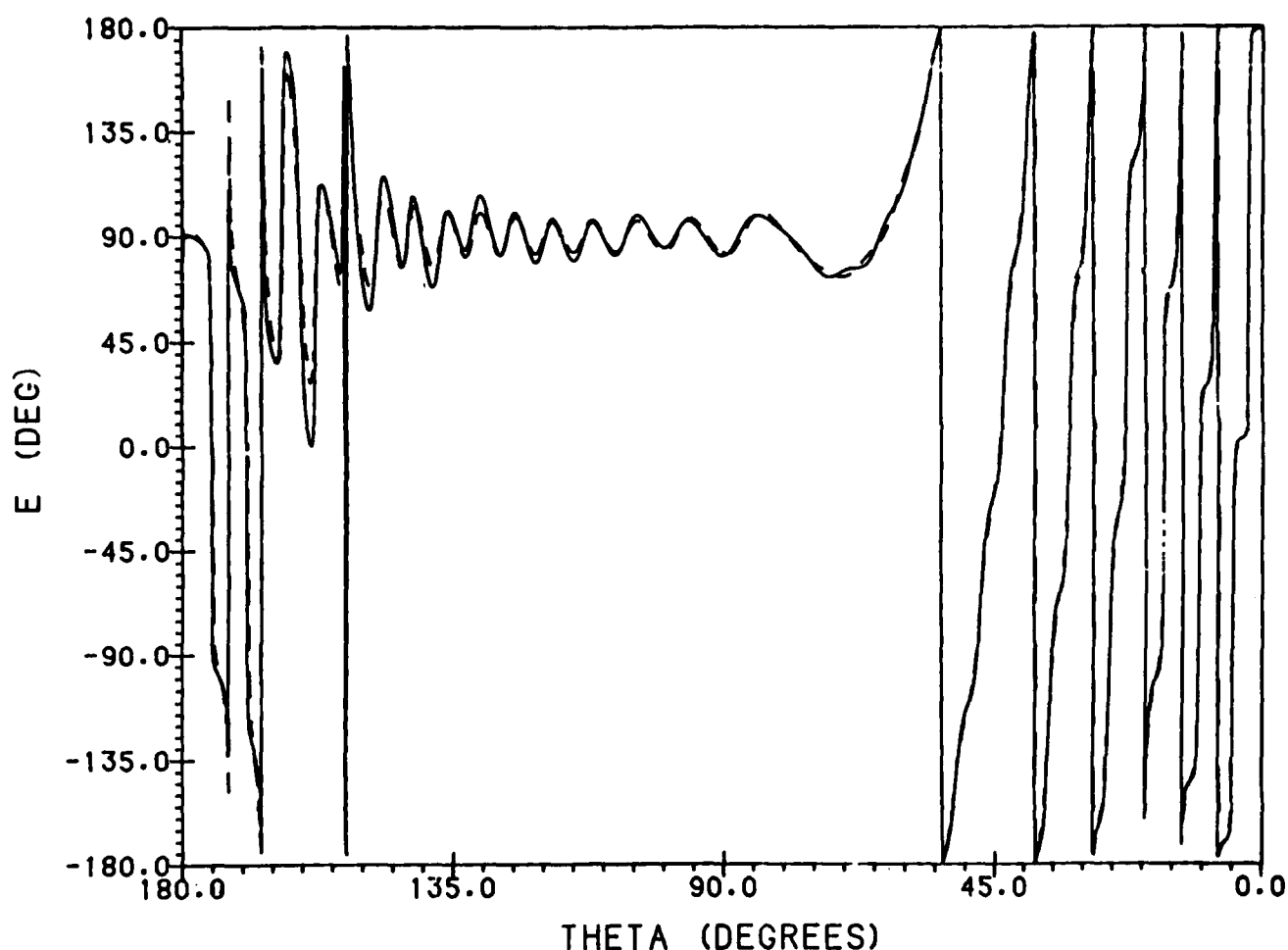We now make some general comments on the patterns shown in Figures 3 through 10. Referring to the dipole-feed antenna patterns of Figures 3 a, b, the effect of the nonuniform current field in the E- and H-planes is masked by the primary dipole-feed pattern. In the φ = 45° plane (Figure 3c), however, the primary dipole-feed cross-polar field is close to zero for θ close to 180°, and the effect of the nonuniform current field is clearly seen, resulting in a raising of the nulls. In contrast, for the Huygens-feed antenna, both the co- and cross-polar primary feed fields are close to zero near the forward direction and, referring to Figures 7 a, b, c, the effect of the nonuniform current field may be seen in the E- and H-planes as well as in the cross-polar field pattern for φ = 45°. The effect is most striking in the cross-polar pattern where the nonuniform current field corrects the PO plus feed sidelobe levels upwards by as much as 6 dB.

Turning next to the pattern plot for the full range of θ, it is seen from Figures 5 a, b and 9 a, b that the back lobes of the E- and H-plane patterns for both the dipole-feed and Huygens-feed antennas are strongly affected by the nonuniform current field. In the E-plane, the nonuniform current field raises the

40

back lobes, while in the H-plane the back lobes are lowered from the PO plus feed levels. In contrast, referring to Figures 5c and 9c, the back lobes of the cross-polar PO plus feed patterns are changed very little by adding the nonuniform current field.

In the next set of figures, we show the results of calculations in which the primary feed field is not added to the secondary reflector field. These patterns are of more practical interest near the forward direction, especially those for the dipole-feed antenna, since realistic feeds are highly directive and have negligibly small radiation in the forward reflector region. Figures 12 a, b, c show, respectively, the dipole-feed antenna amplitude pattern for θ from 180° to 155° in the E- and H-plane, and the cross-polar amplitude pattern in the φ = 45° plane. Figures 13 a, b, c show the corresponding phase patterns. Figures 14 a, b, c and 15 a, b, c show the same dipole-feed antenna amplitude and phase patterns for the full range of θ. Figures 16 a, b, c through 19 a, b, c show the corresponding amplitude and phase patterns of the Huygens-feed antenna.

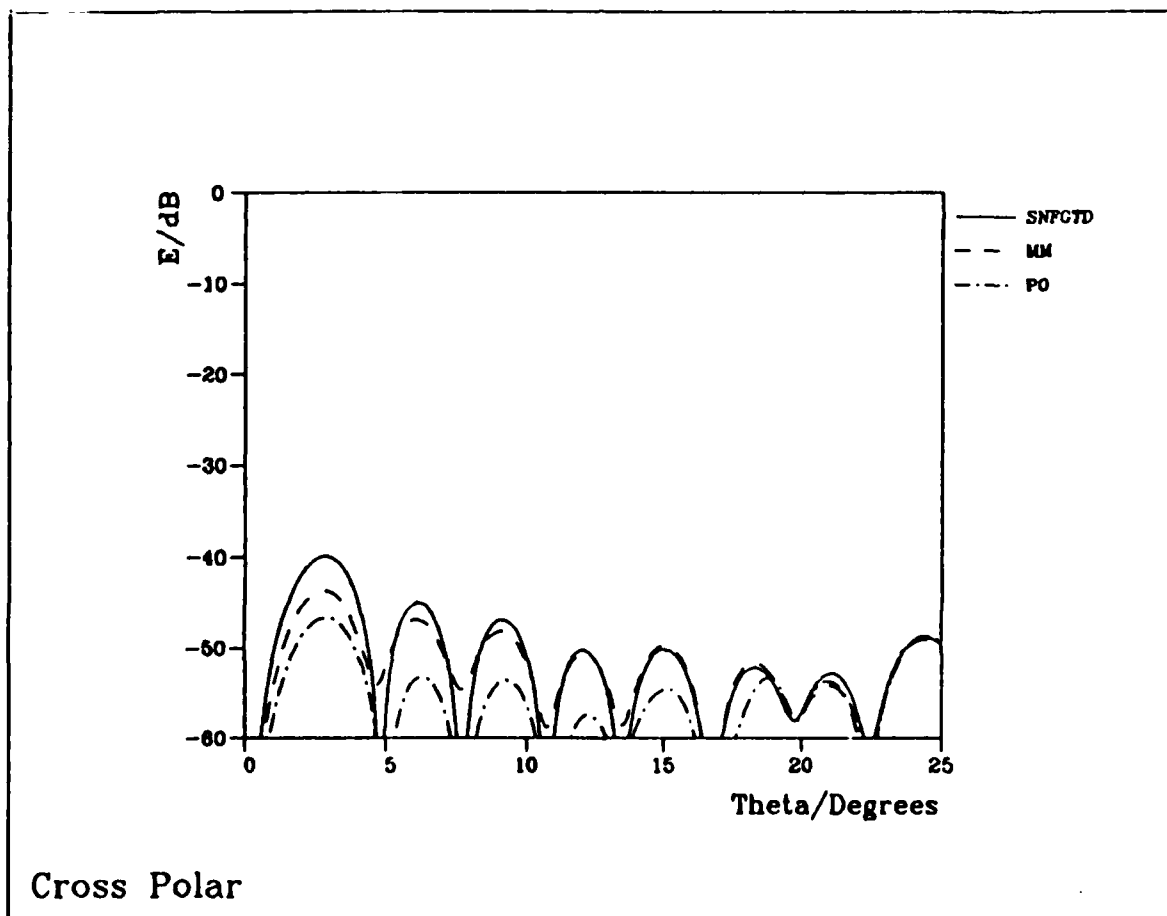

Figure 11. φ = 45° Cross-Polar Amplitude Pattern of 20λ Huygens-Feed Paraboloid Antenna With Primary Field Included; ———— Spherical Near-Field GTD, – – – – Moment Method, —·—·—·— PO. F/D = 0.4, (After Viskum and Bach[20])

41

Figure 12a. E-Plane Amplitude Pattern of 20λ Dipole-Feed Paraboloid Antenna, Primary Field Not Included; – – – – PO, ——— PO + Nonuniform Current Field, F/D = 0.4, θ = [180°, 155°]
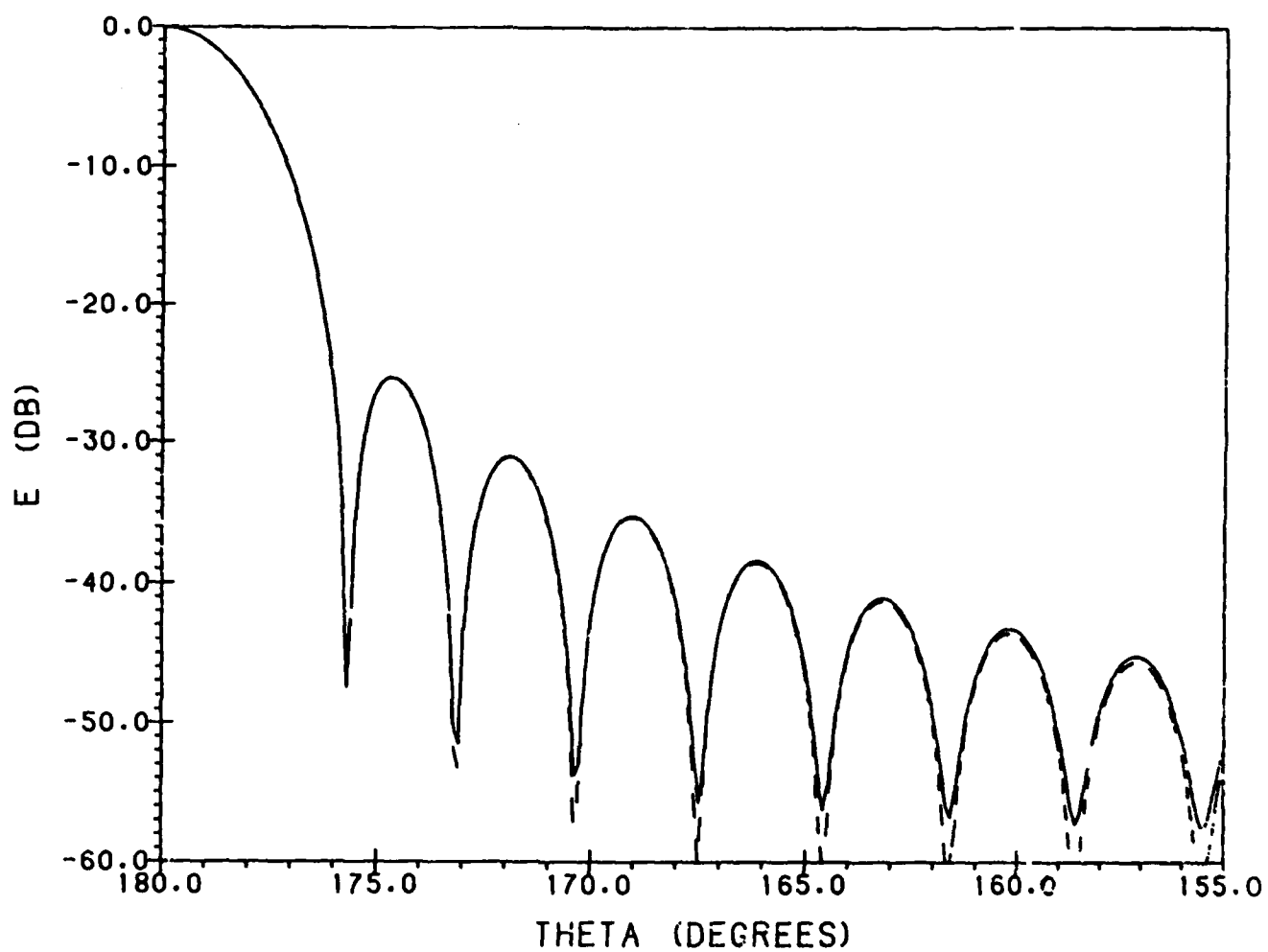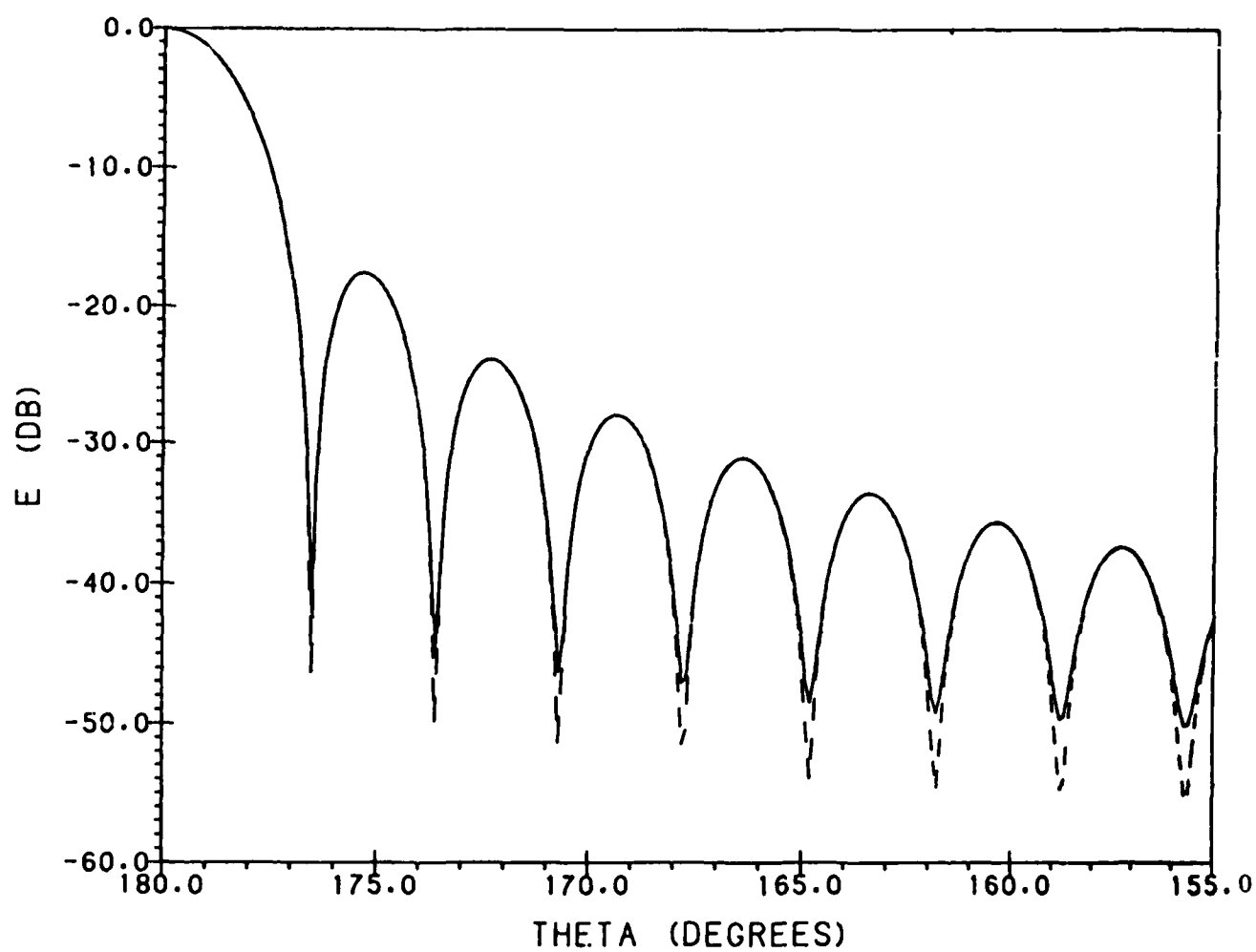
Figure 12b. H-Plane Amplitude Pattern of 20λ Dipole-Feed Paraboloid Antenna, Primary Field Not Included; ---- PO, ——— PO + Nonuniform Current Field, F/D = 0.4, θ = [180°, 155°]

Figure 12c. $\phi = 45°$ Cross-Polar Amplitude Pattern of 20λ Dipole-Feed Paraboloid Antenna, Primary Field Not Included; – – – – PO, ———— PO + Nonuniform Current Field, F/D = 0.4, θ = [180°, 155°]

Figure 13a. E-Plane Phase Pattern of 20λ Dipole-Feed Paraboloid Antenna, Primary Field Not Included;
— — — — PO, ————— PO + Nonuniform Current Field, F/D = 0.4, θ = [180°, 155°]

Figure 13b. H-Plane Phase Pattern of 20λ Dipole-Feed Paraboloid Antenna, Primary Field Not Included; ---- PO, ——— PO + Nonuniform Current Field, F/D = 0.4, θ = [180°, 155°]

46

Figure 13c. ϕ = 45° Cross-Polar Phase Pattern of 20λ Dipole-Feed Paraboloid Antenna, Primary Field Not Included; – – – – PO, ———— PO + Nonuniform Current Field, F/D = 0.4, θ = [180°, 155°]
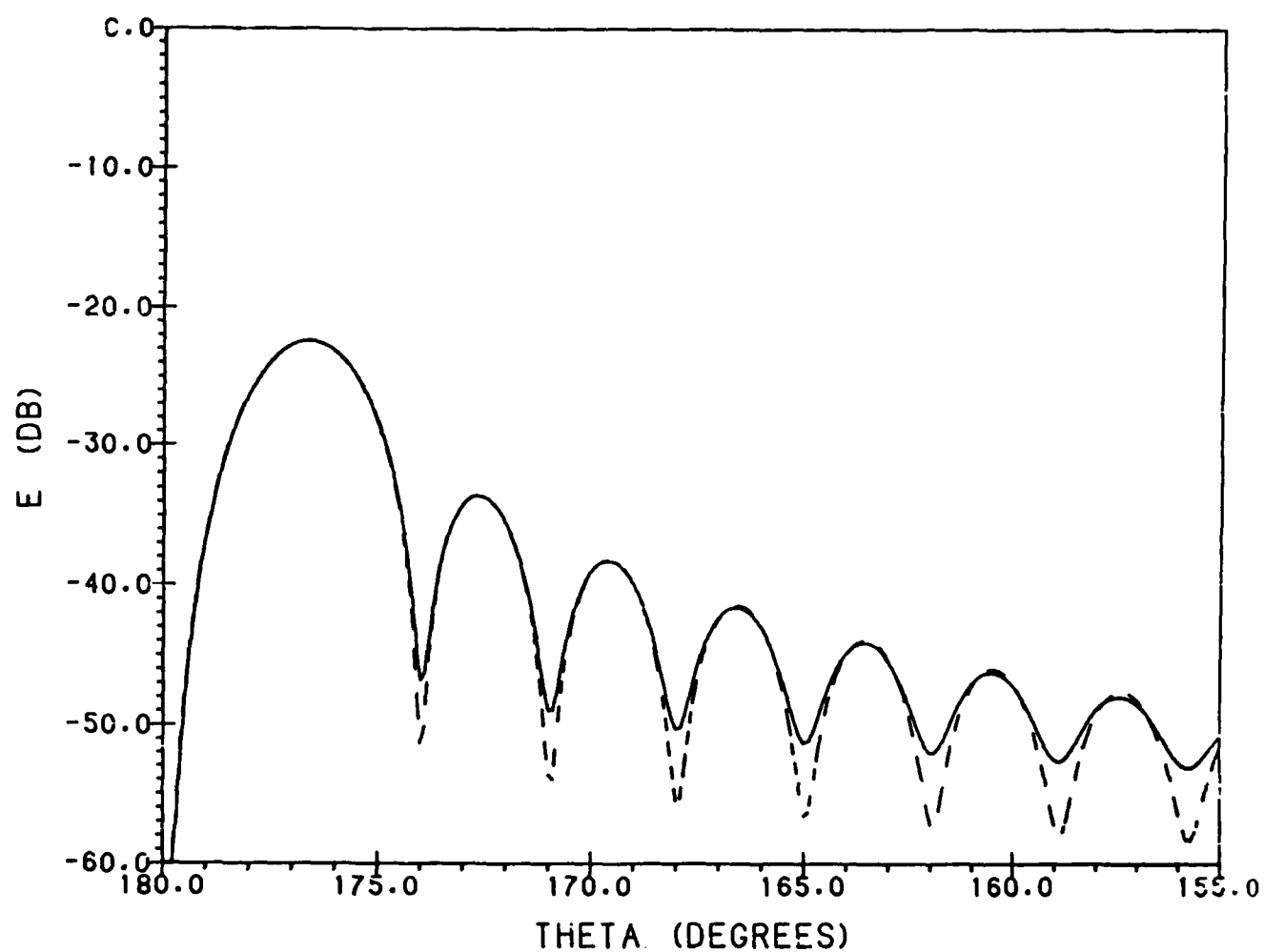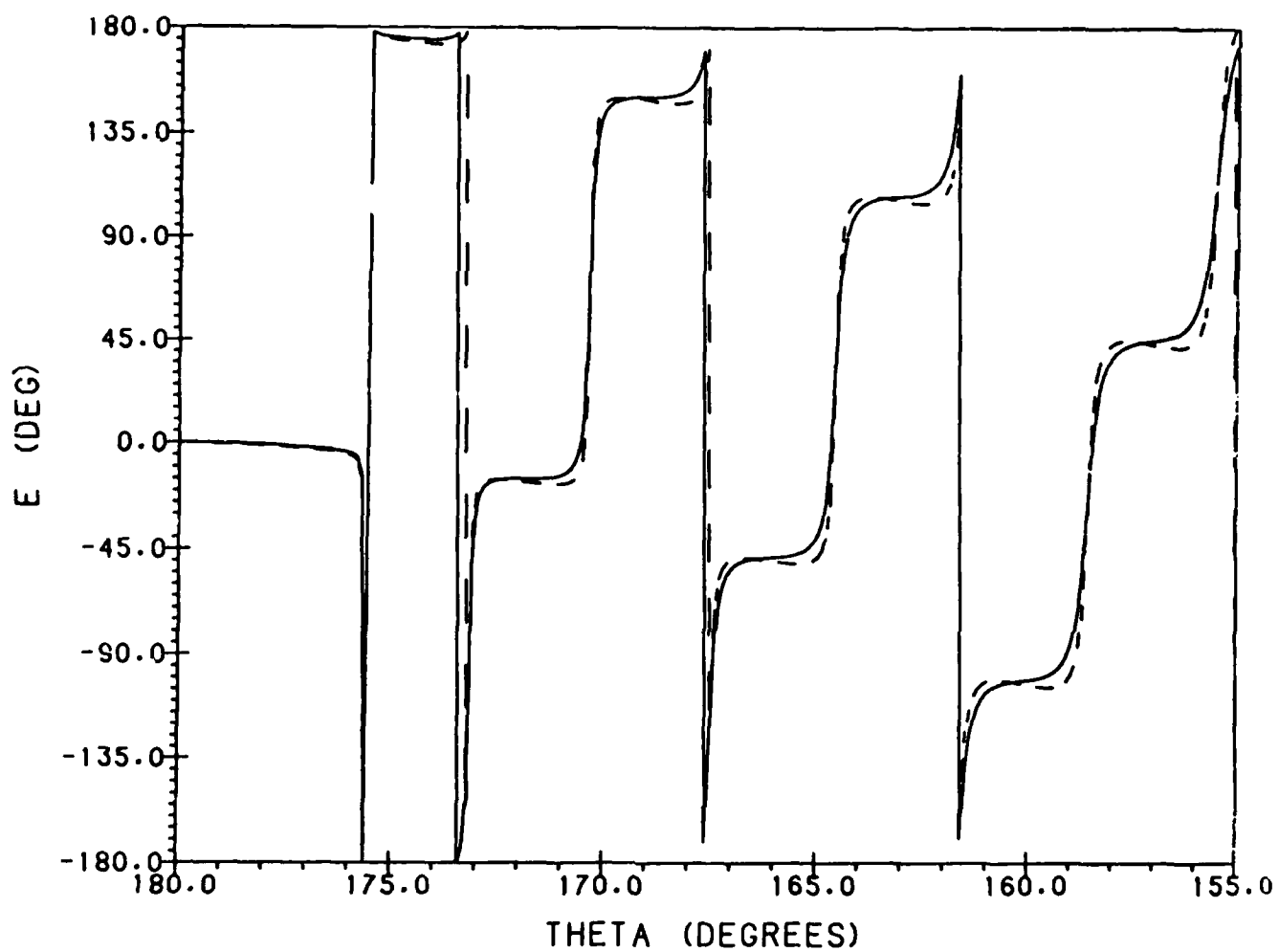
47

Figure 14a. E-Plane Amplitude Pattern of 20λ Dipole-Feed Faraboloid Antenna, Primary Field Not Included;
— — — — PO, ————— PO + Nonuniform Current Field, F/D = 0.4, θ = [180°, 0°]

48

Figure 14b. H-Plane Amplitude Pattern of 20λ Dipole-Feed Paraboloid Antenna, Primary Field Not Included; – – – – PO, ——— PO + Nonuniform Current Field, F/D = 0.4, θ = [180°, 0°]

Figure 14c. $\phi = 45°$ Cross-Polar Amplitude Pattern of 20λ Dipole-Feed Paraboloid Antenna, Primary Field Not Included; – – – – PO, ——— PO + Nonuniform Current Field, F/D = 0.4, θ = [180°, 0°]

50

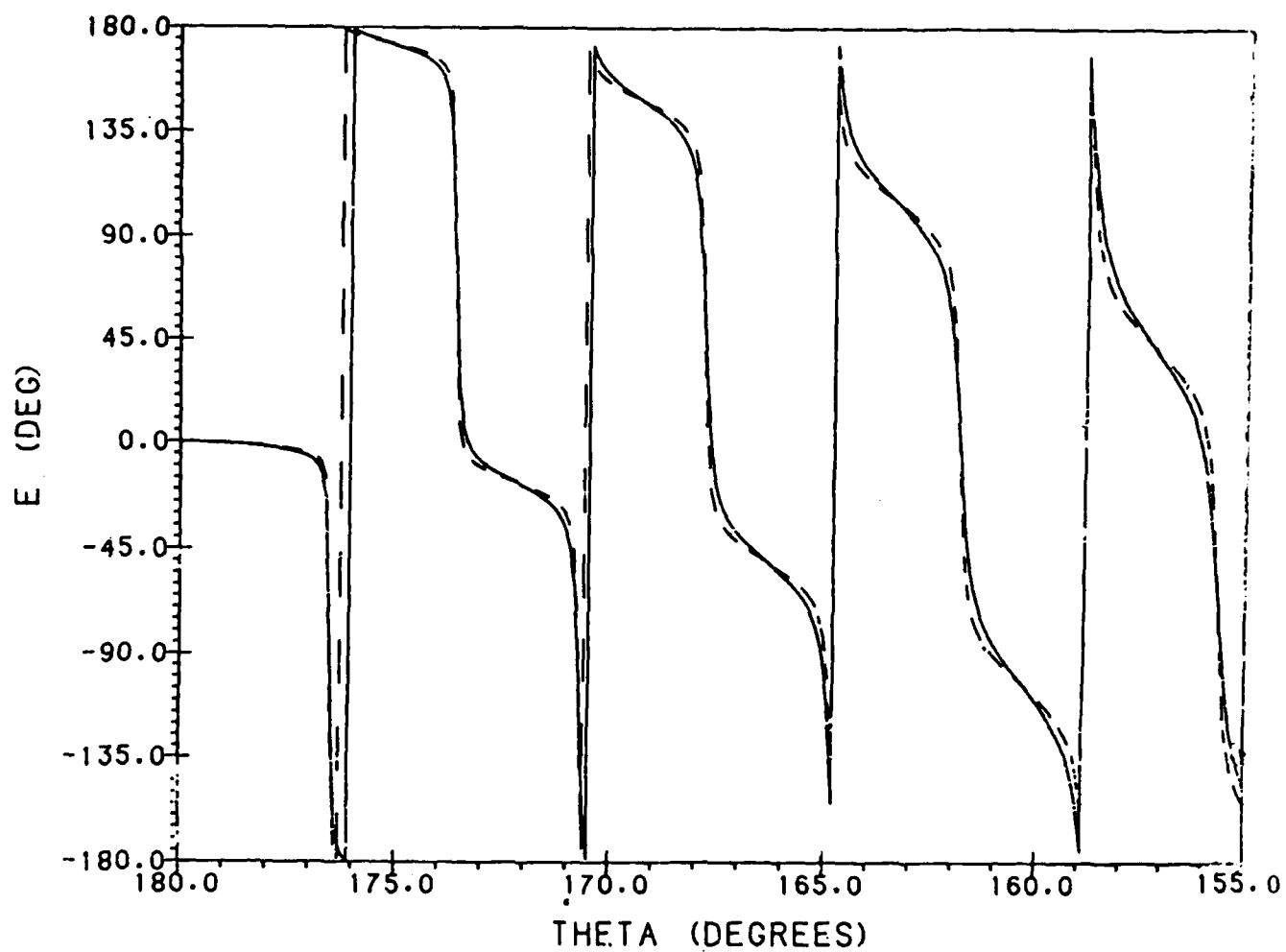Figure 15a. E-Plane Phase Pattern of 20λ Dipole-Feed Paraboloid Antenna, Primary Field Not Included;
- - - - PO, ——— PO + Nonuniform Current Field, F/D = 0.4, θ = [180°, 0°]

Figure 15b. H-Plane Phase Pattern of 20λ Dipole-Feed Paraboloid Antenna, Primary Field Not Included; ----PO, ——— PO + Nonuniform Current Field, F/D = 0.4, θ = [180°, 0°]
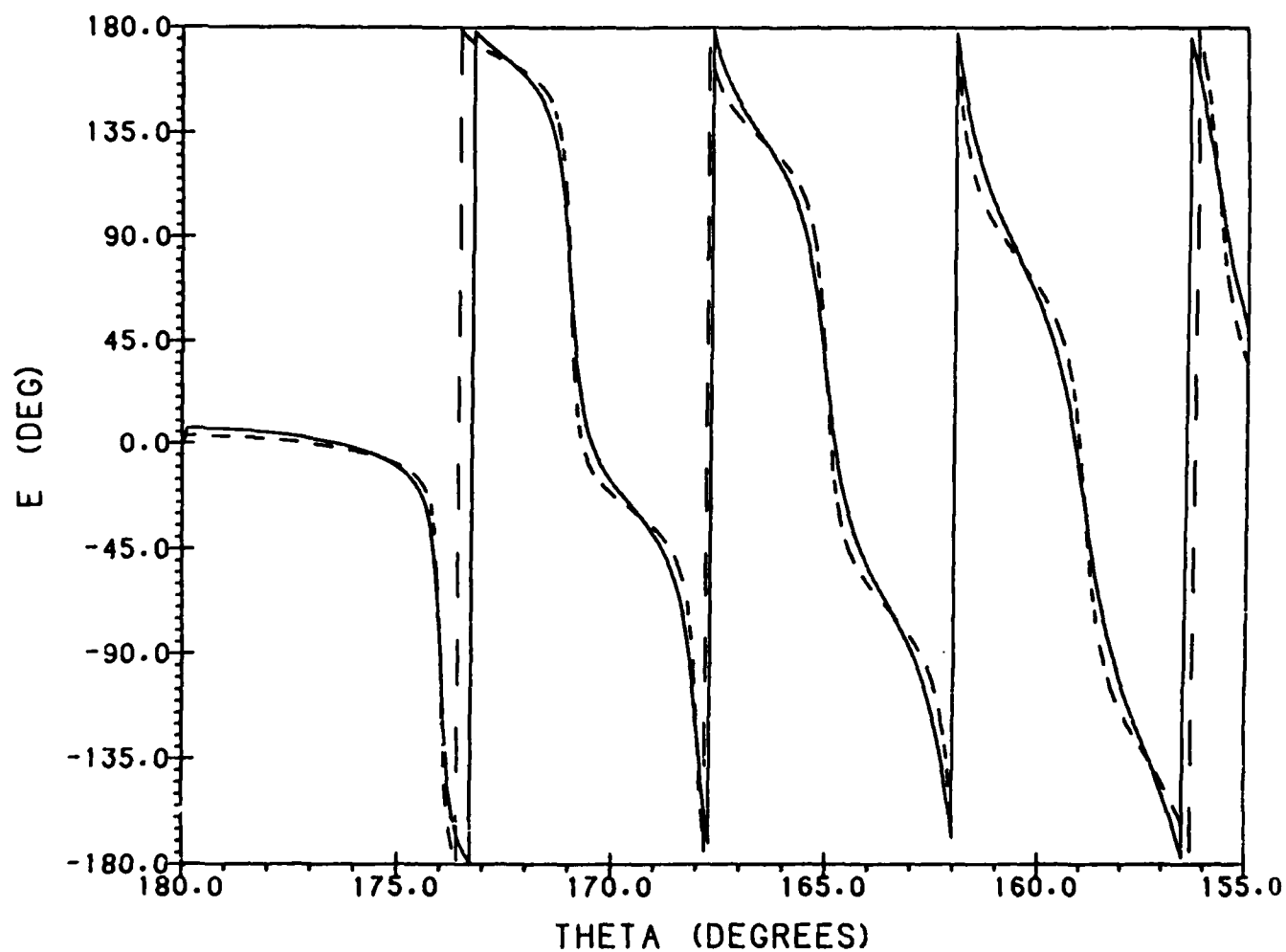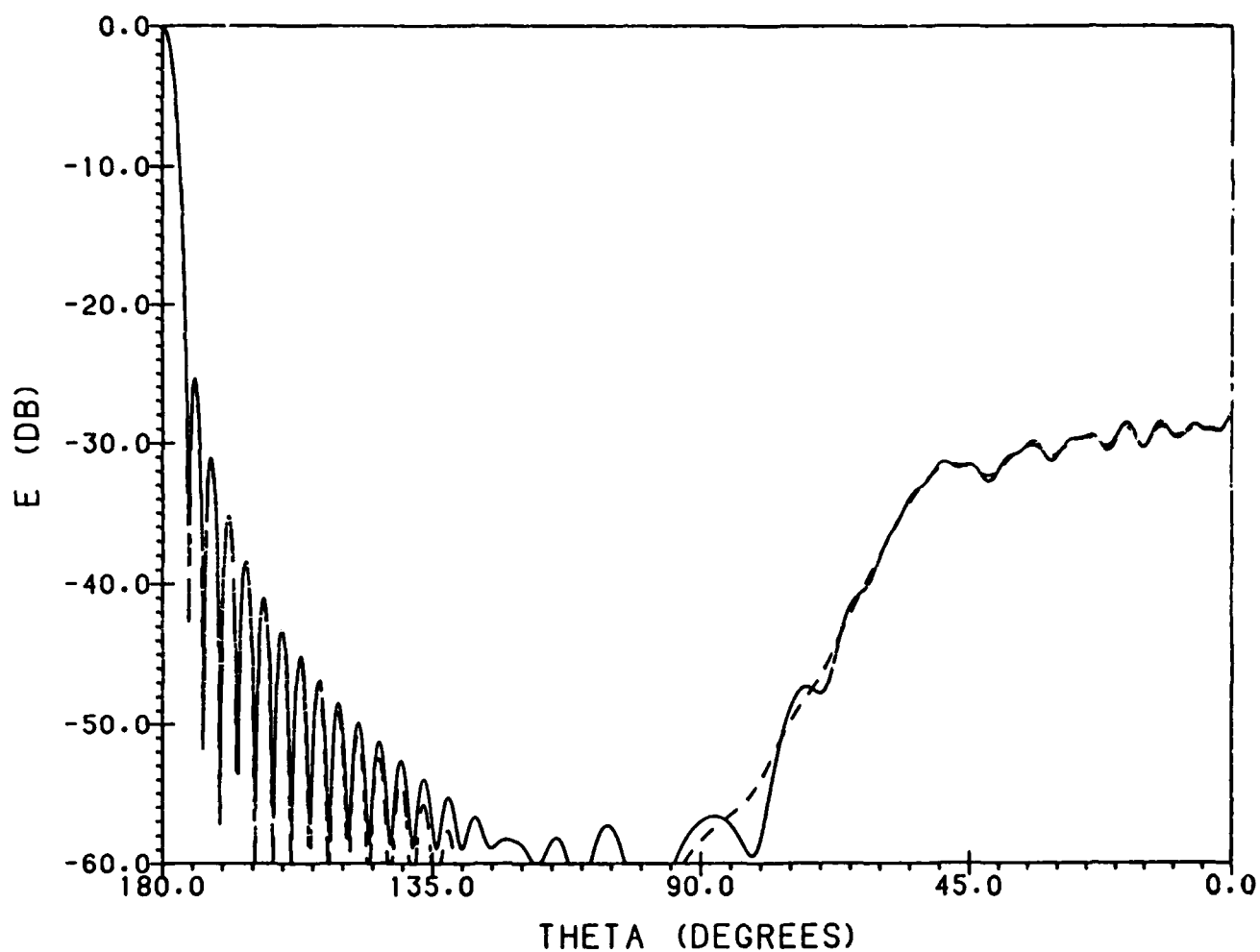
Figure 15c. ϕ = 45° Cross-Polar Phase Pattern of 20λ Dipole-Feed Paraboloid Antenna, Primary Field Not Included; — — — PO, ——— PO + Nonuniform Current Field, F/D = 0.4, θ = [180°, 0°]

Figure 16a. E-Plane Amplitude Pattern of 20λ Huygens-Feed Paraboloid Antenna, Primary Field Not Included; ─ ─ ─ ─ PO, ───── PO + Nonuniform Current Field, F/D = 0.4, θ = [180°, 155°]
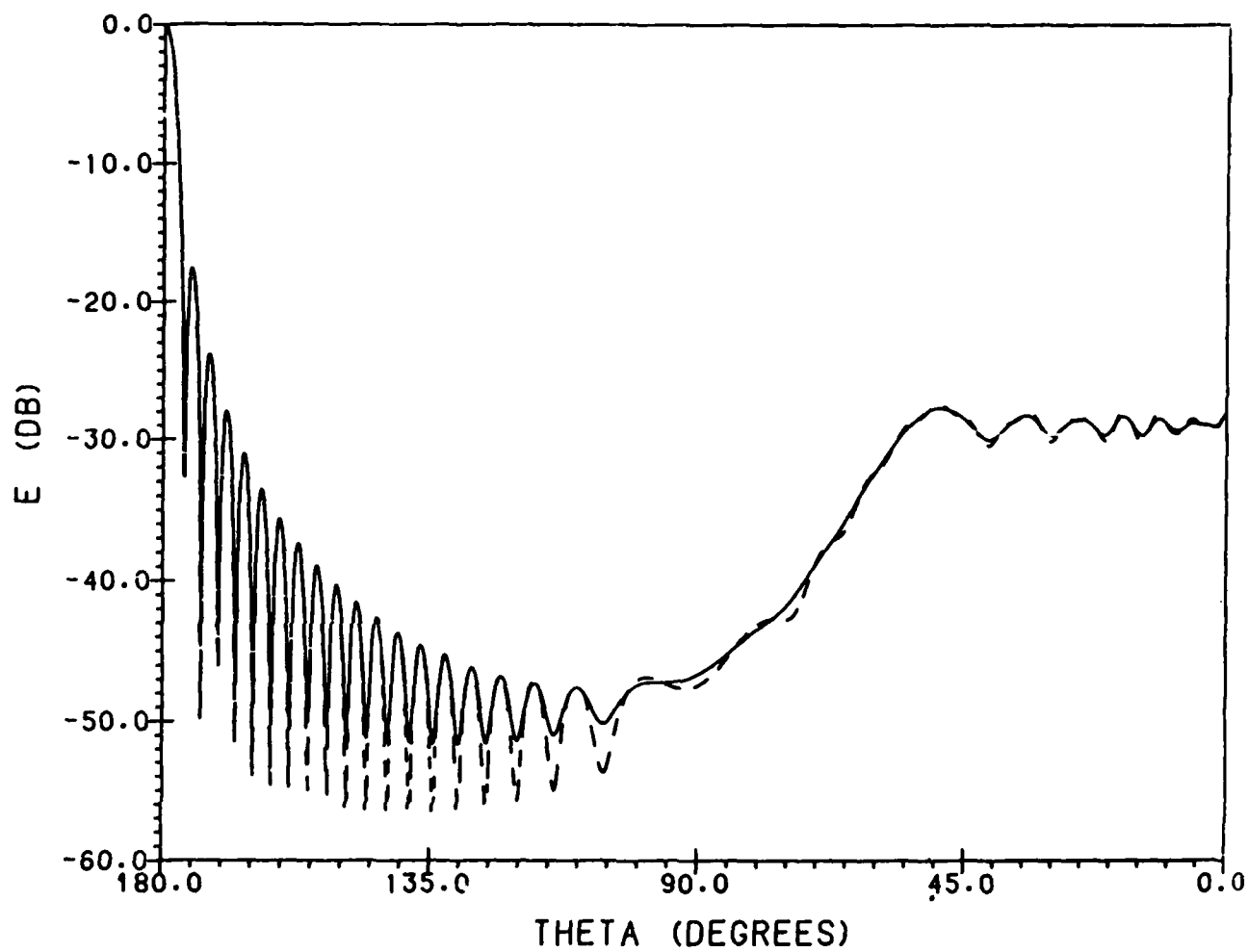
Figure 16b. H-Plane Amplitude Pattern of 20λ Huygens-Feed Paraboloid Antenna, Primary Field Not Included; – – – – PO, ———— PO + Nonuniform Current Field, F/D = 0.4, θ = [180°, 155°]

Figure 16c. $\phi = 45°$ Cross-Polar Amplitude Pattern of 20λ Huygens-Feed Paraboloid Antenna, Primary Field Not Included; $----$ PO, $———$ PO + Nonuniform Current Field, F/D = 0.4, $\theta = [180°, 155°]$

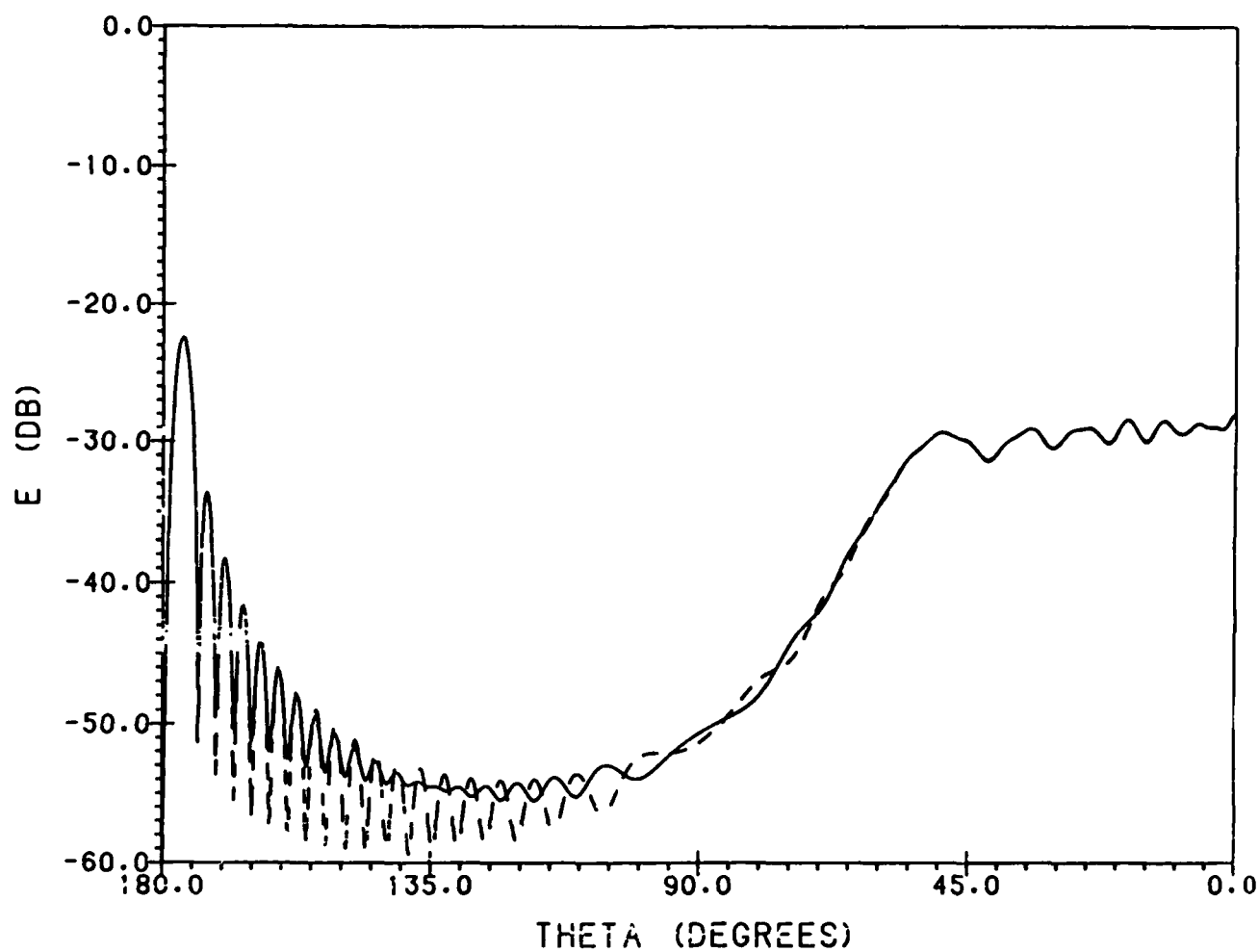Figure 17a. E-Plane Phase Pattern of 20λ Huygens-Feed Paraboloid Antenna, Primary Field Not Included; ---- PO, ——— PO + Nonuniform Current Field, F/D = 0.4, θ = [180°, 155°]
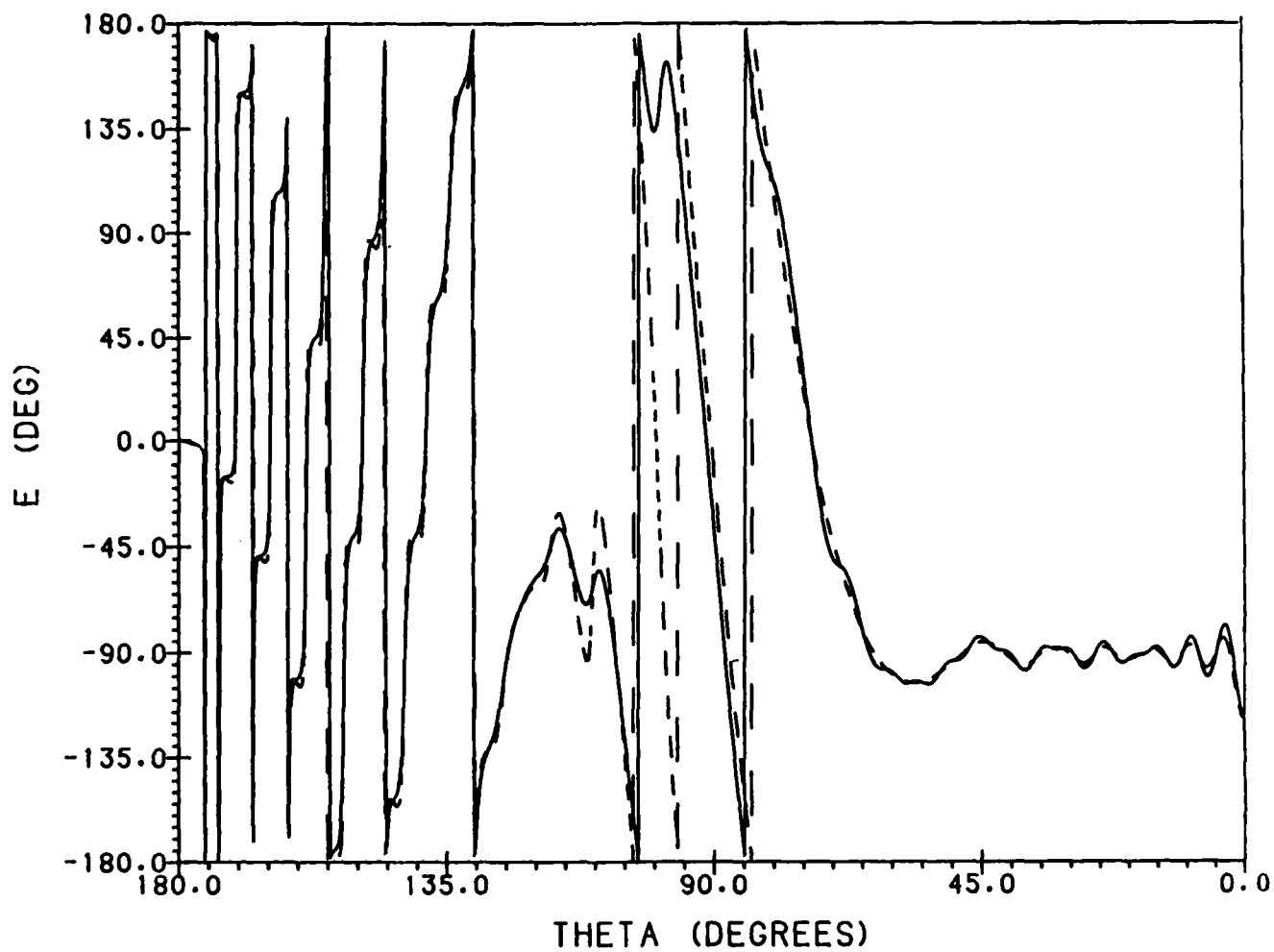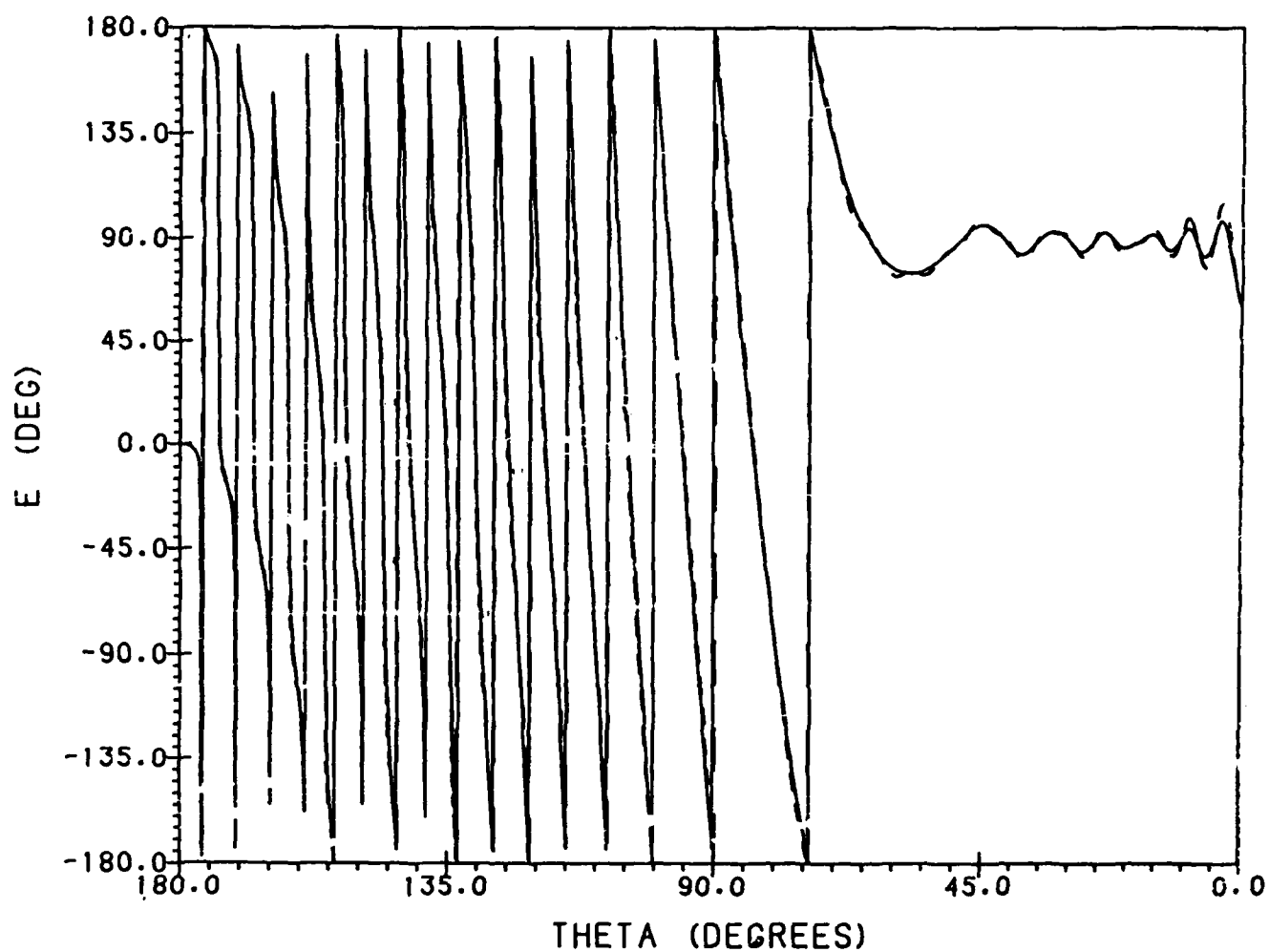
Figure 17b. H-Plane Phase Pattern of 20λ Huygens-Feed Paraboloid Antenna, Primary Field Not Included;
− − − − PO, ———— PO + Nonuniform Current Field, F/D = 0.4, θ = [180°, 155°]

Figure 17c. φ = 45° Cross-Polar Phase Pattern of 20λ Huygens-Feed Paraboloid Antenna, Primary Field Not Included; – – – – PO, ———— PO + Nonuniform Current Field, F/D = 0.4, θ = [180°, 155°]

Figure 18a. E-Plane Amplitude Pattern of 20λ Huygens-Feed Paraboloid Antenna, Primary Field Not Included; ---- PO, ———— PO + Nonuniform Current Field, F/D = 0.4, θ = [180°, 0°]

60
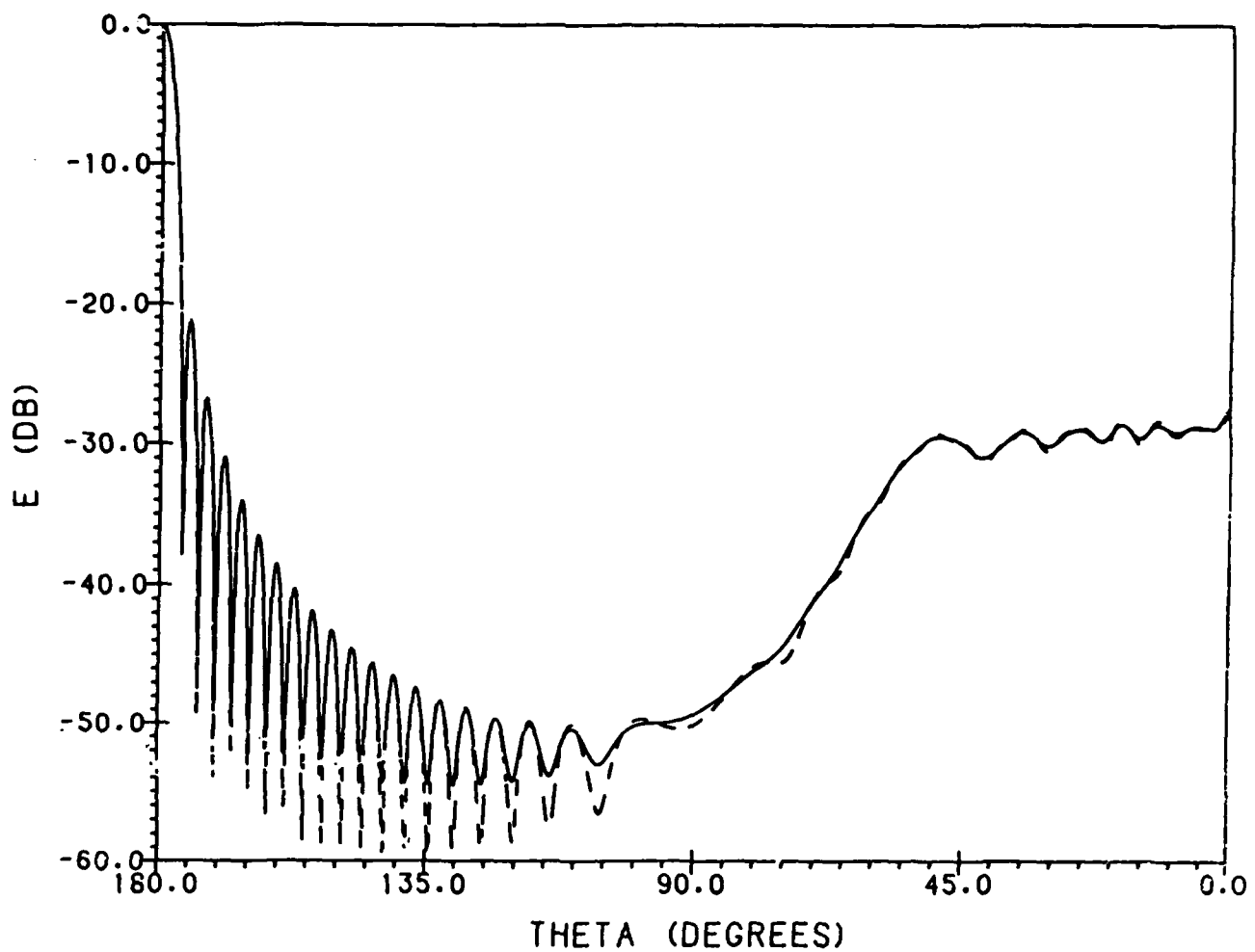
Figure 18b. H-Plane Amplitude Pattern of 20λ Huygens-Feed Paraboloid Antenna, Primary Field Not Included; - - - - PO, ———— PO + Nonuniform Current Field, F/D = 0.4, θ = [180°, 0°]
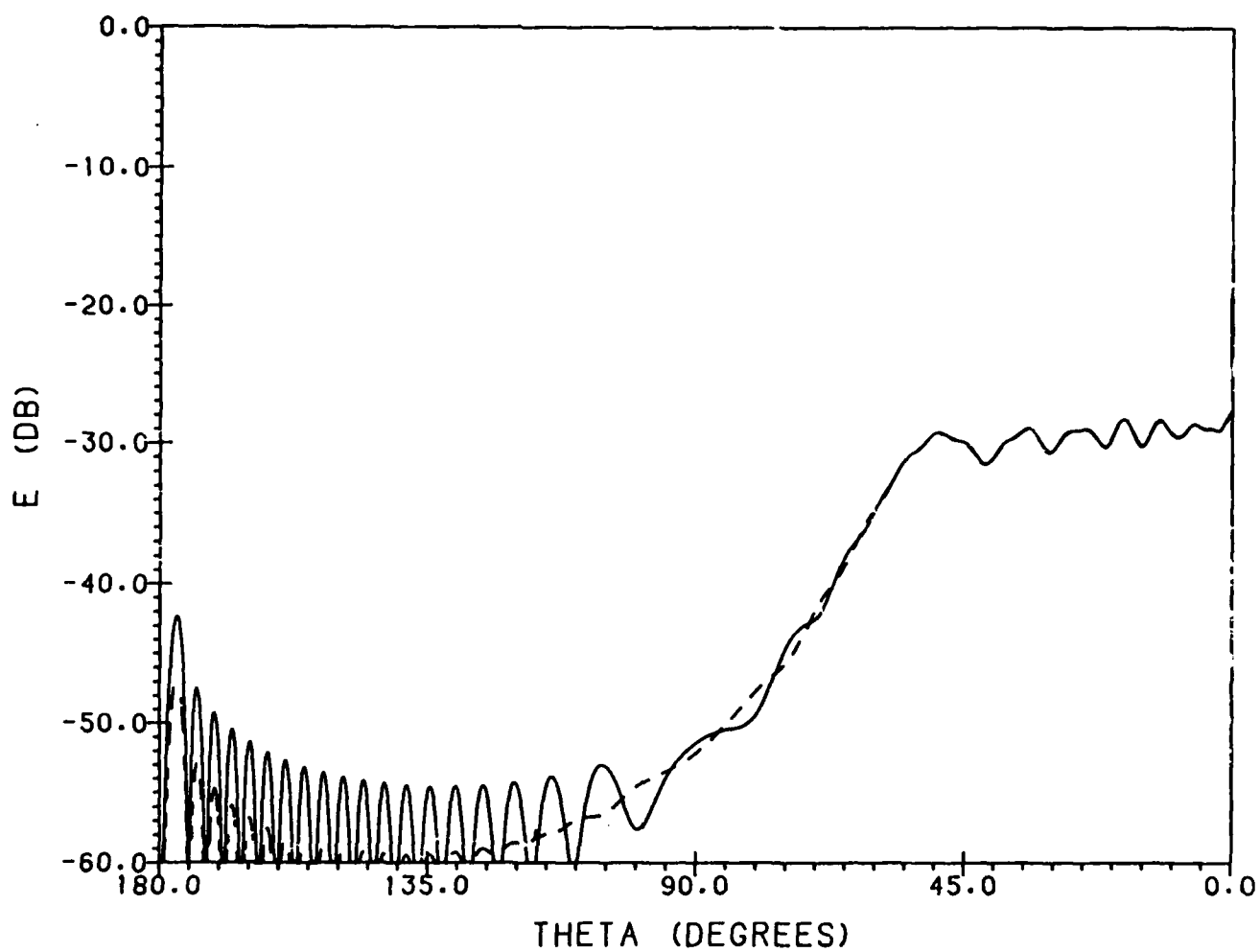
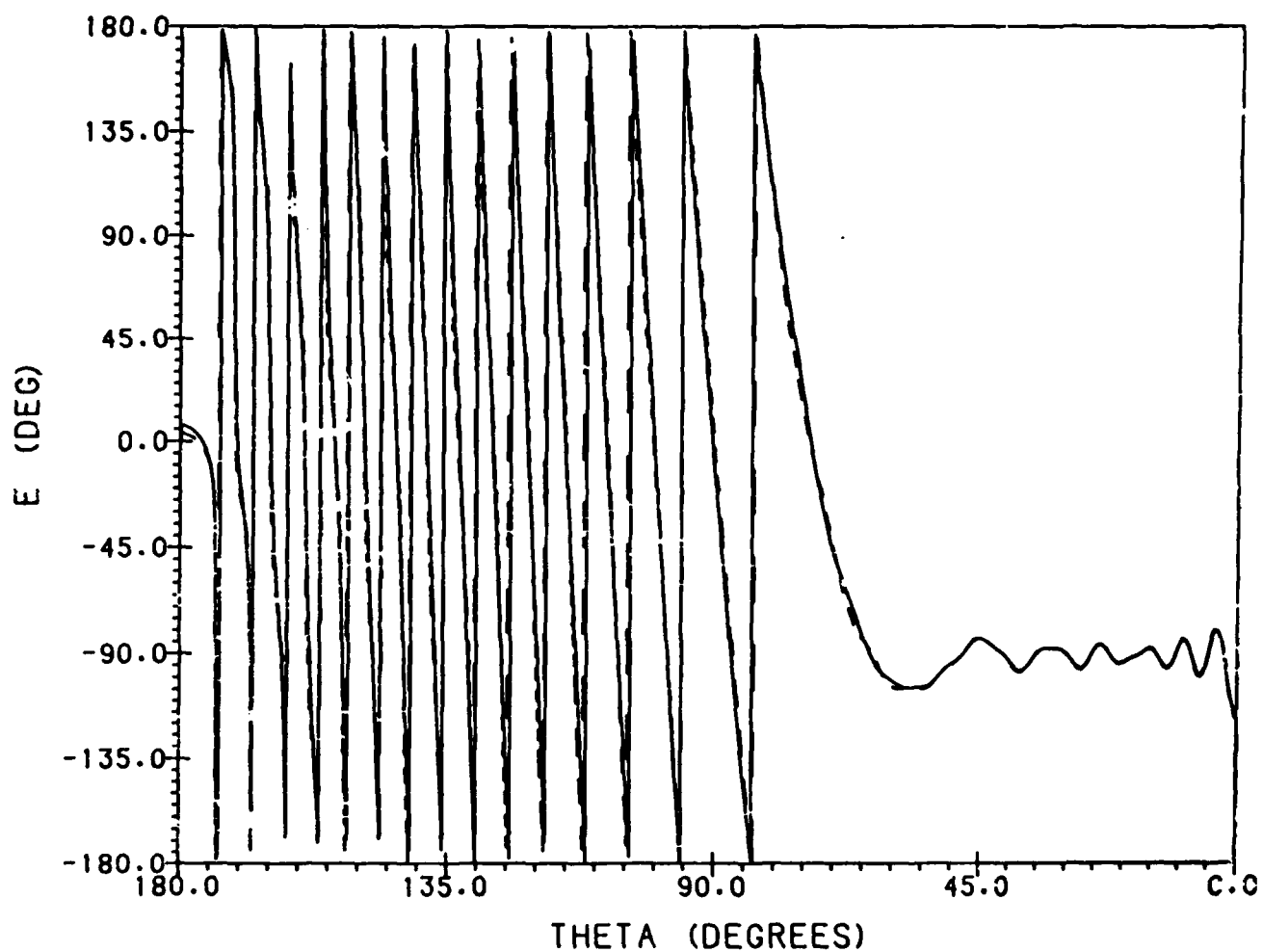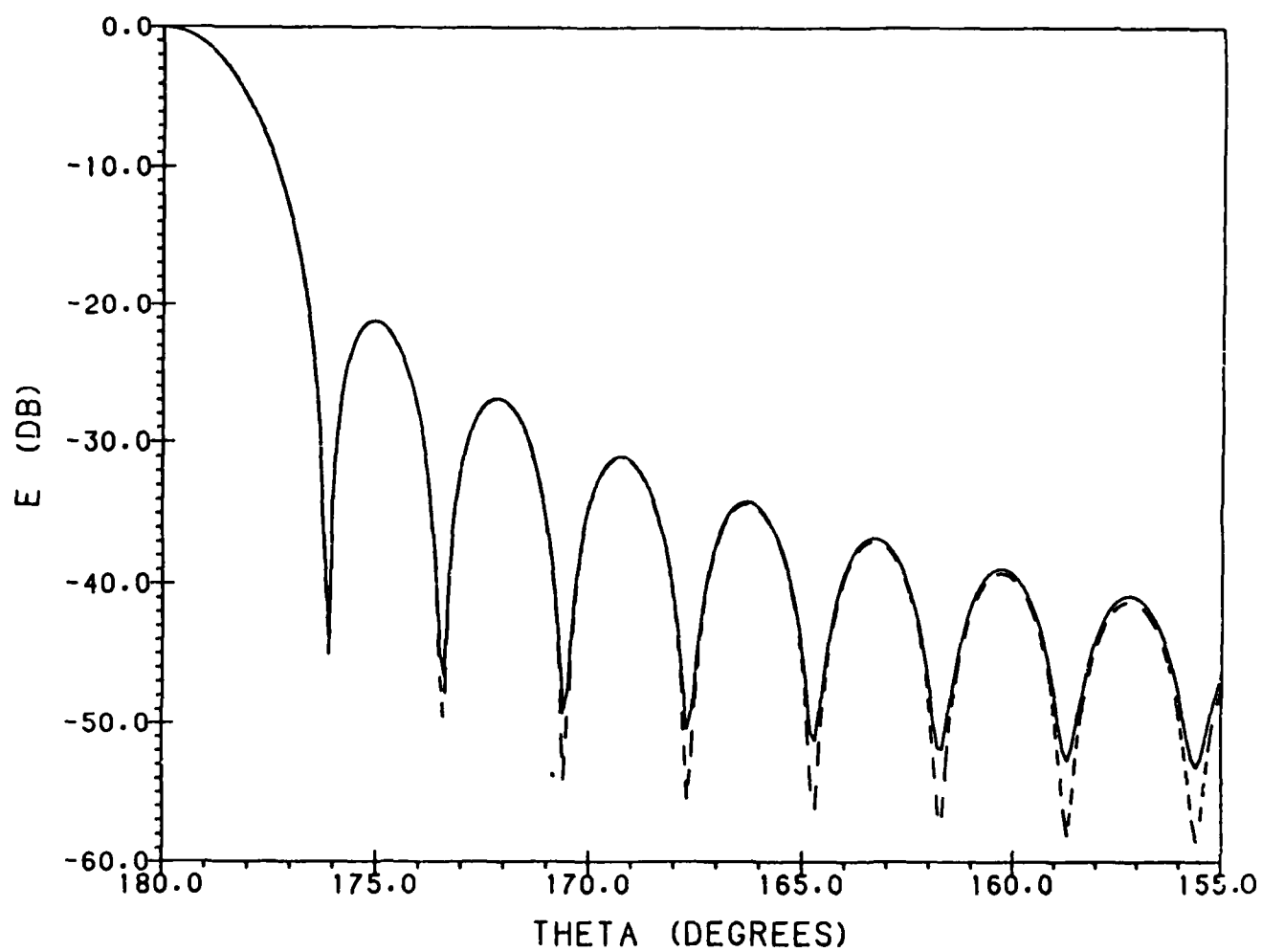Figure 18c. $\phi = 45°$ Cross-Polar Amplitude Pattern of 20λ Huygens-Feed Paraboloid Antenna, Primary Field Not Included; – – – – PO, ——— PO + Nonuniform Current Field, F/D = 0.4, θ = [180°, 0°]
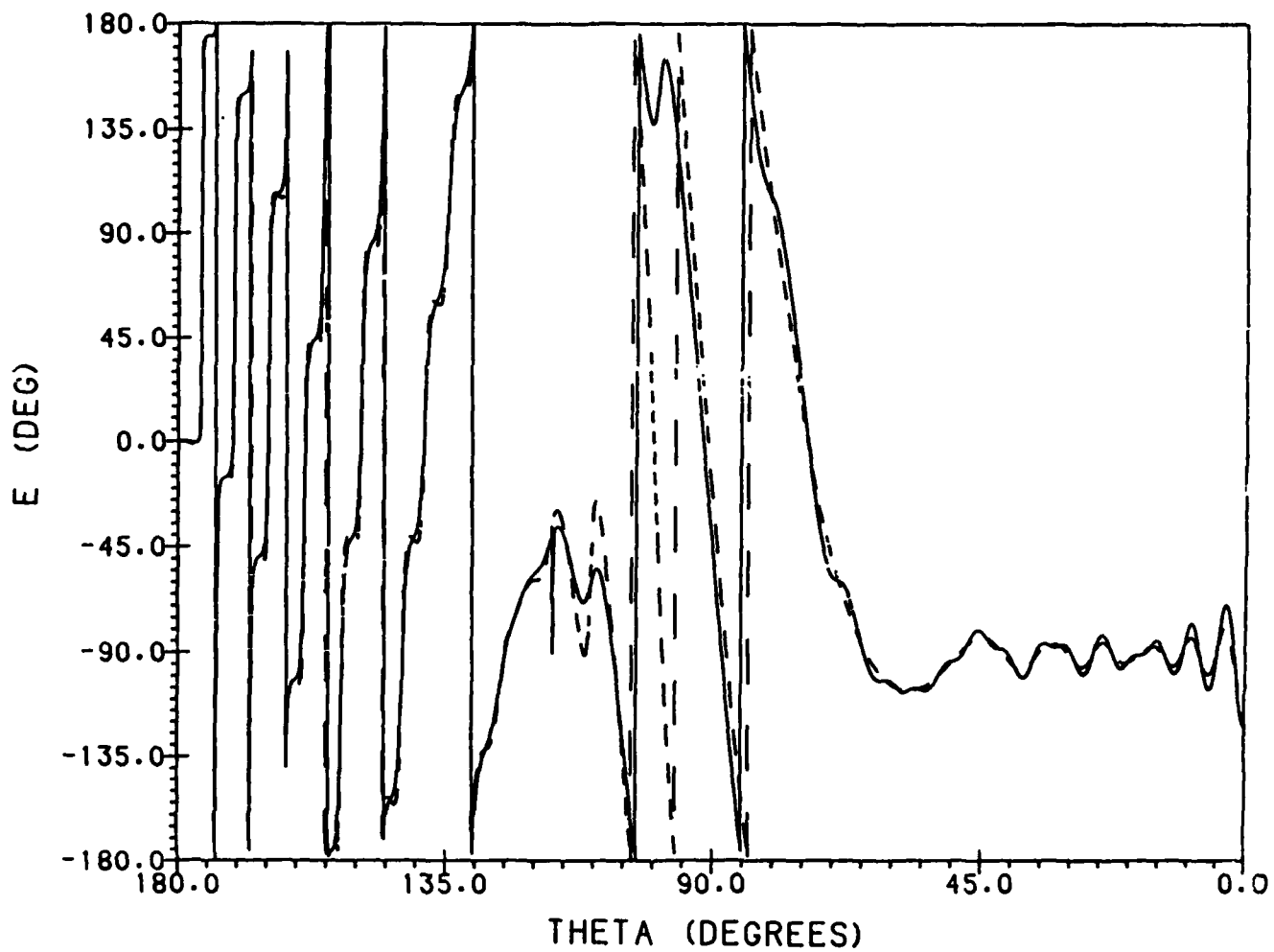
Figure 19a. E-Plane Phase Pattern of 20λ Huygens-Feed Paraboloid Antenna, Primary Field Not Included;
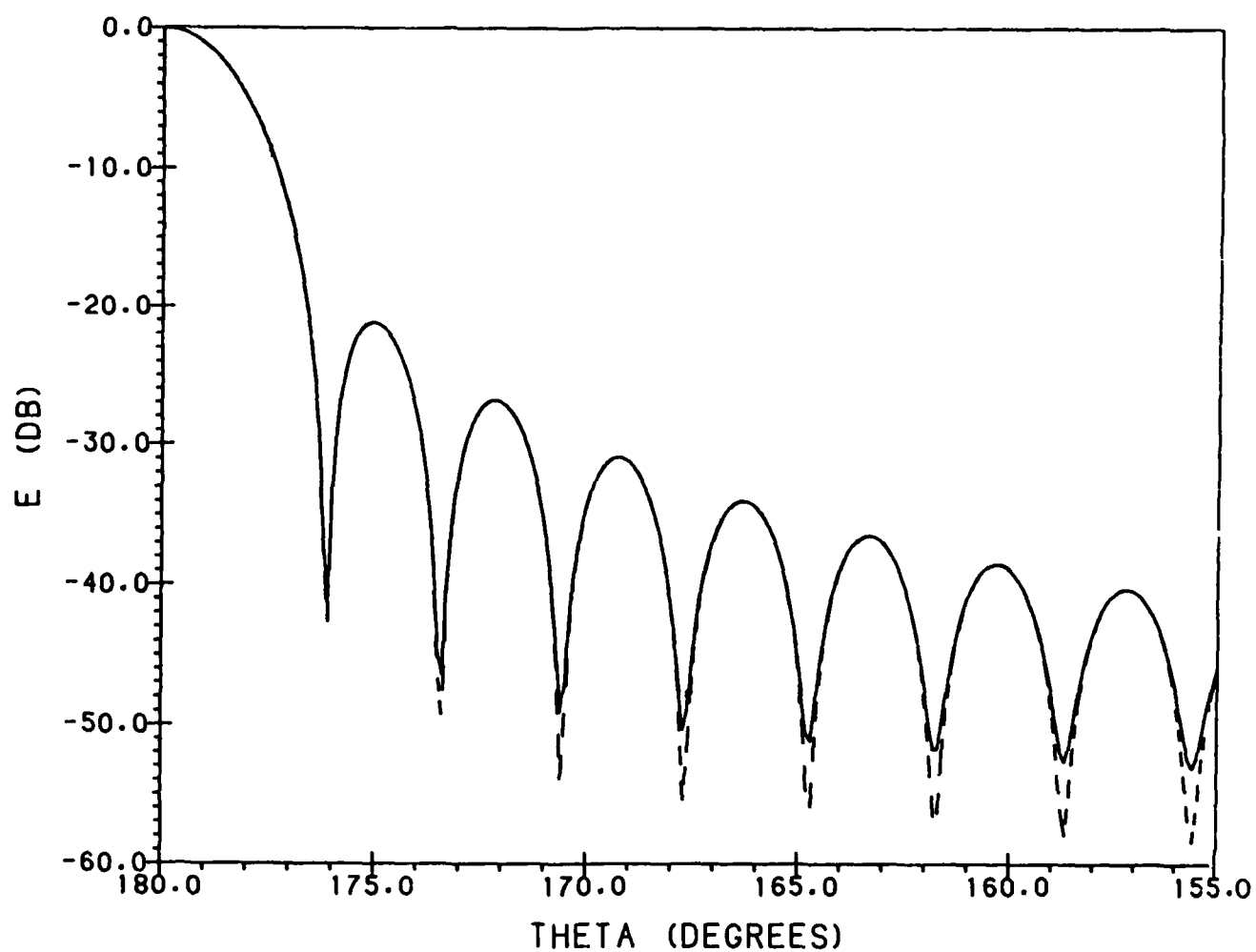– – – – PO, ———— PO + Nonuniform Current Field, F/D = 0.4, θ = [180°, 0°]
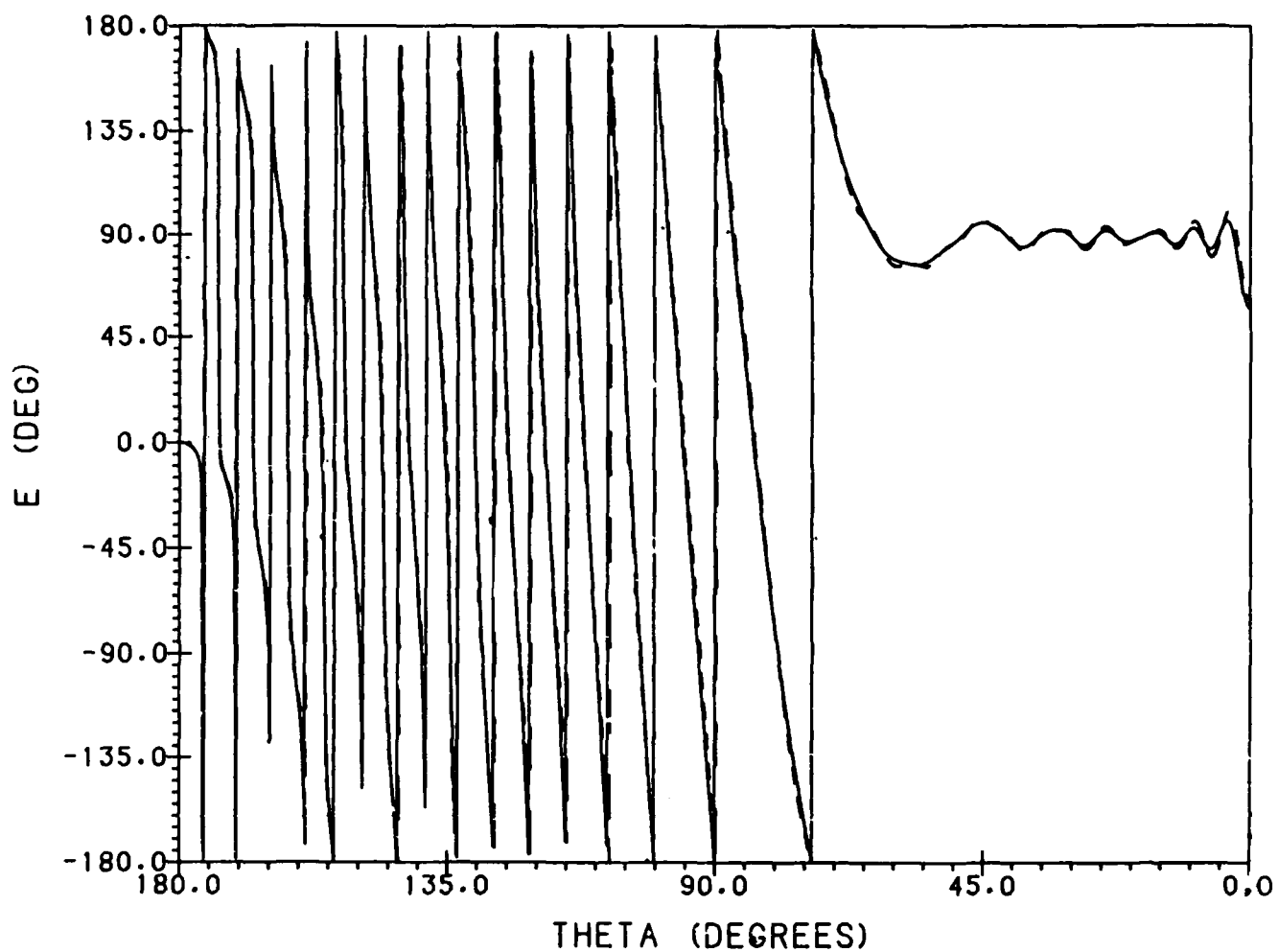
Figure 19b. H-Plane Phase Pattern of 20λ Huygens-Feed Paraboloid Antenna, Primary Field Not Included; ---- PO, ——— PO + Nonuniform Current Field, F/D = 0.4, θ = [180°, 0°]

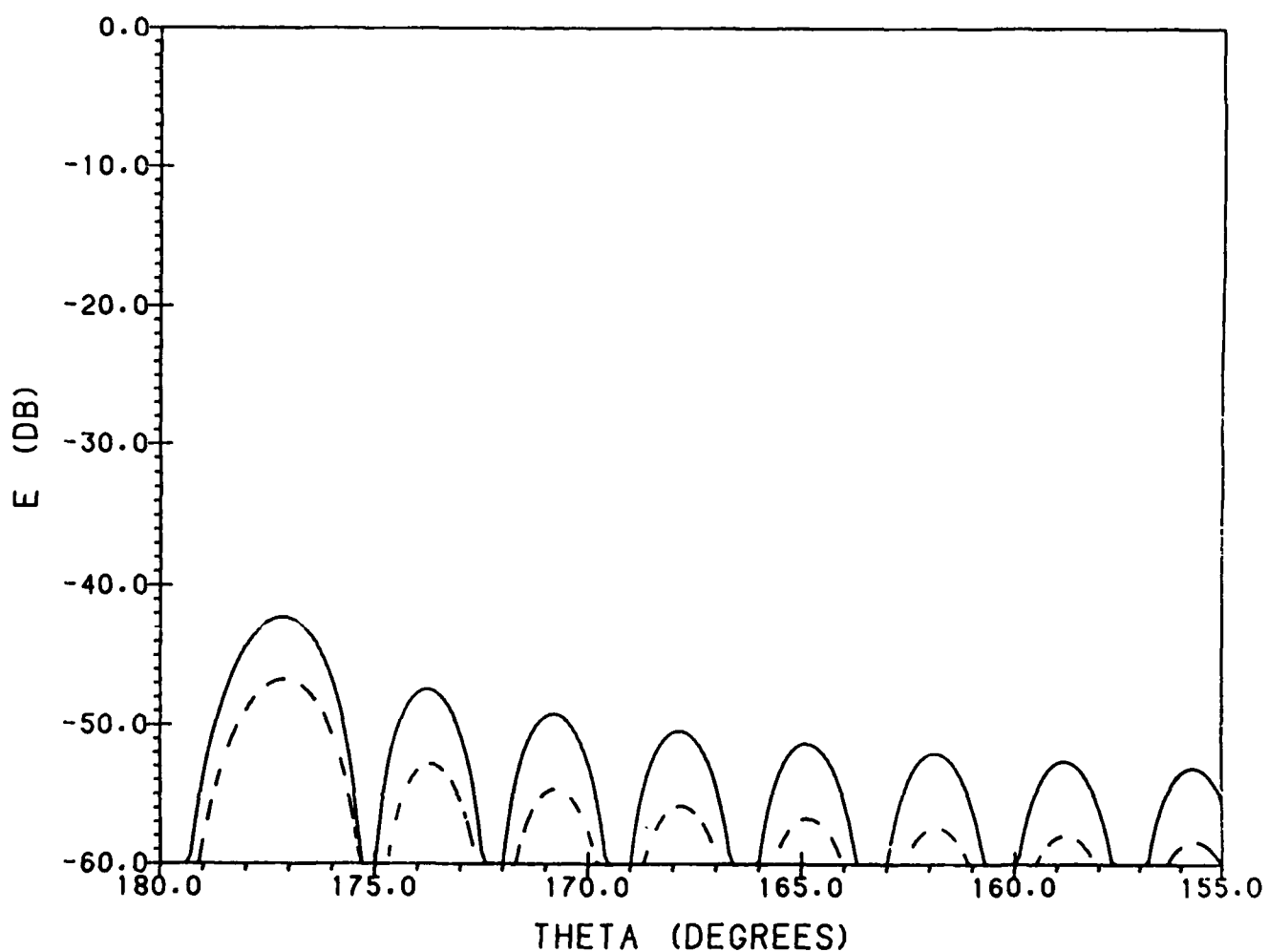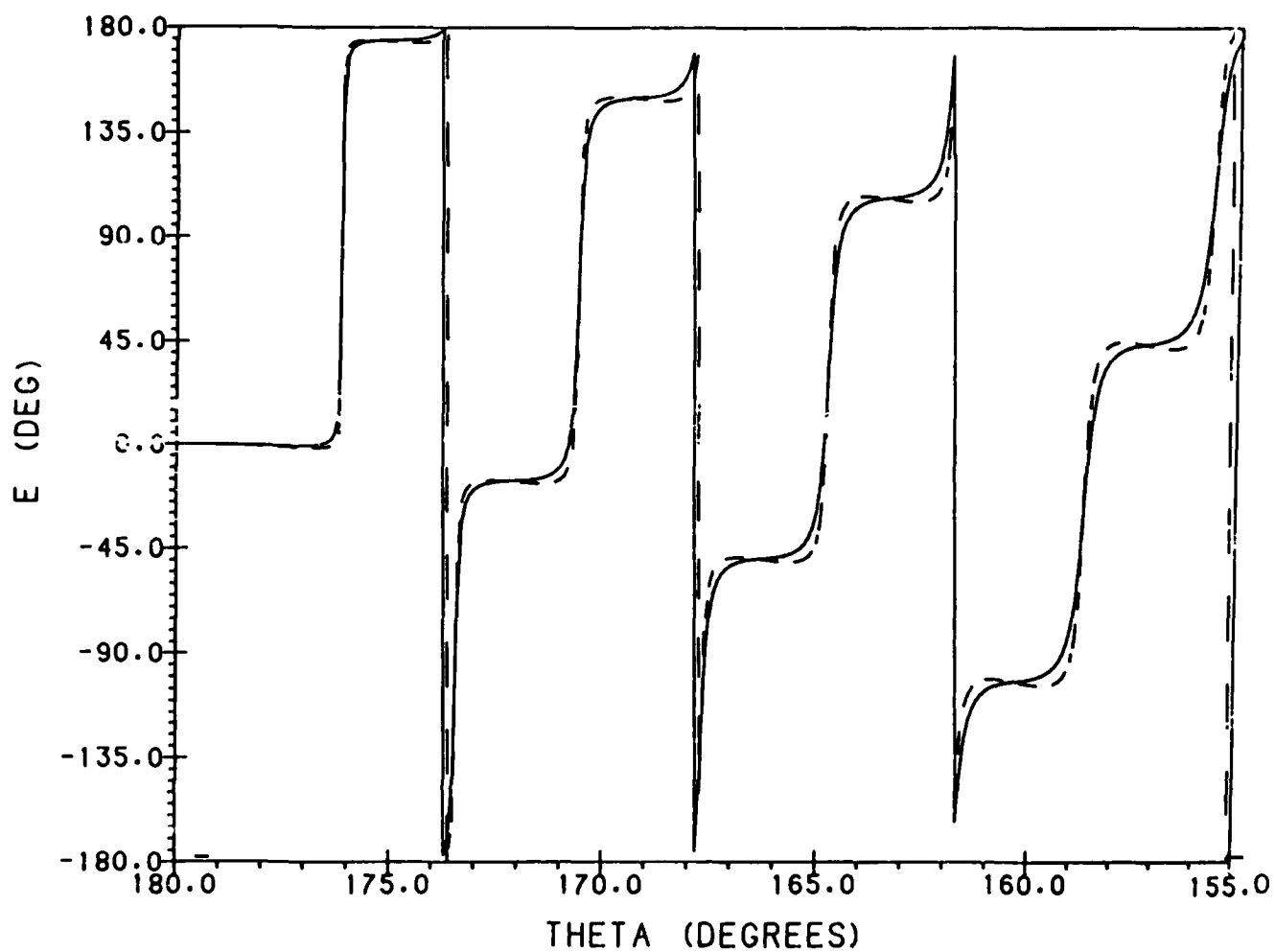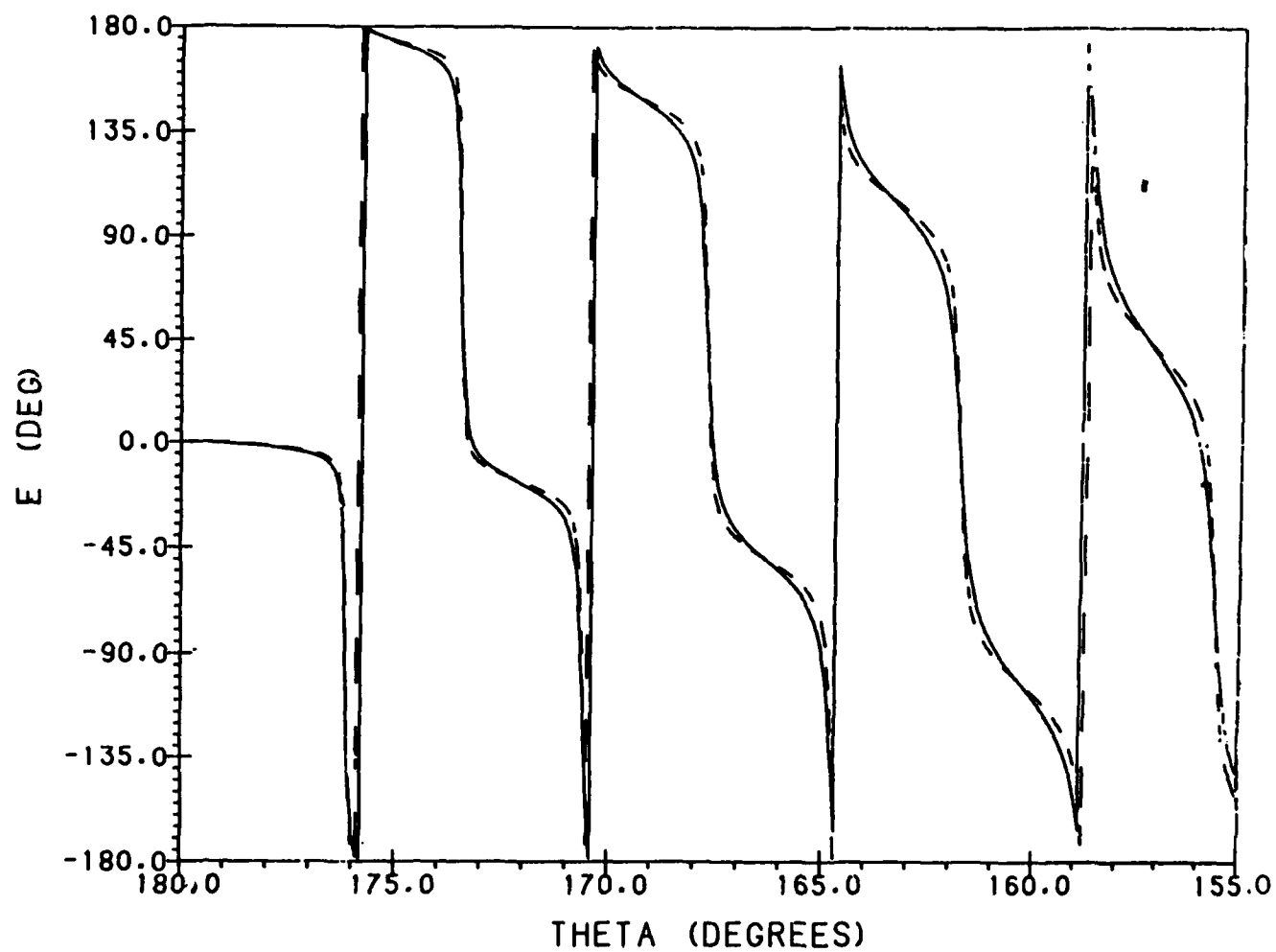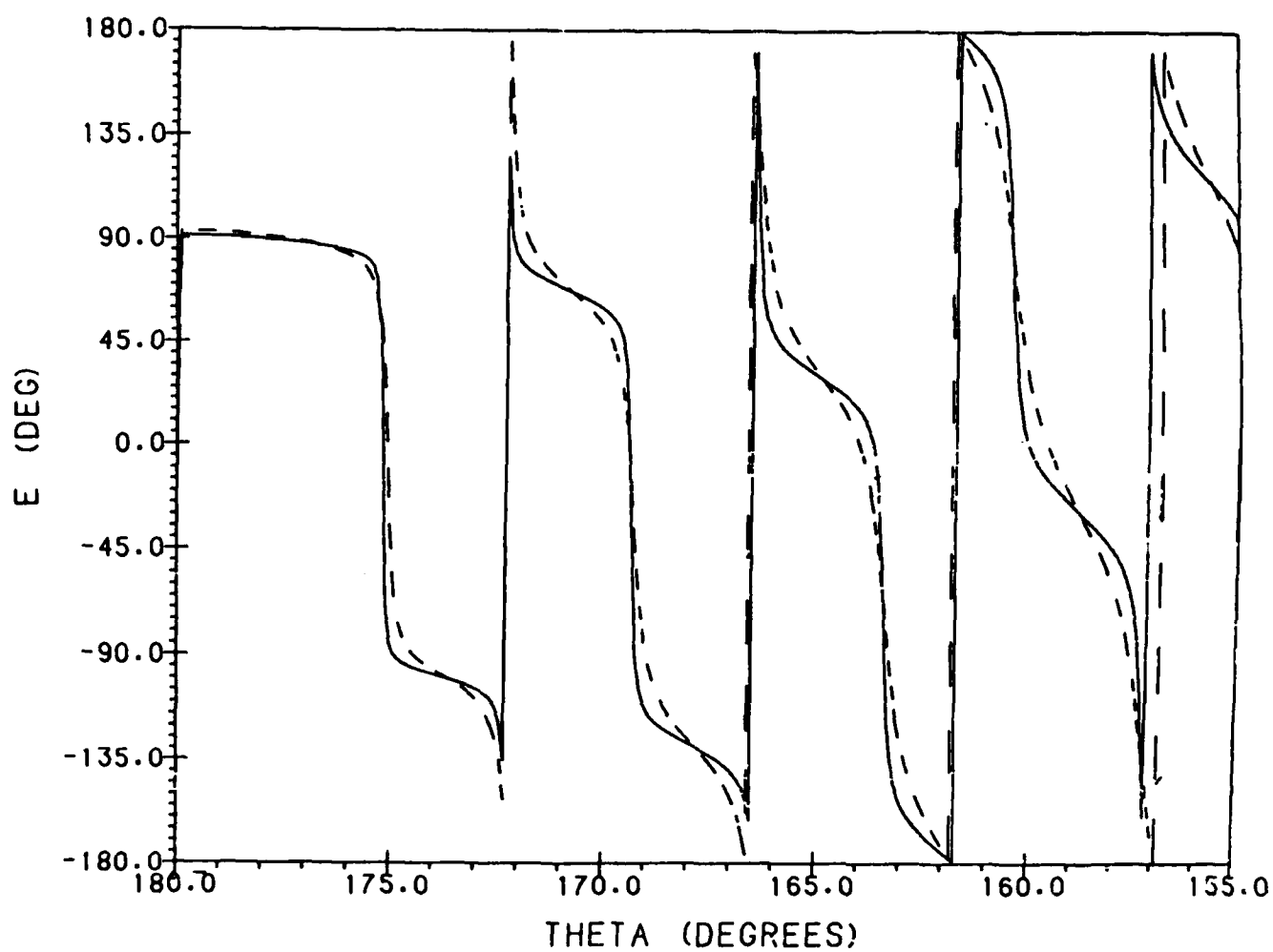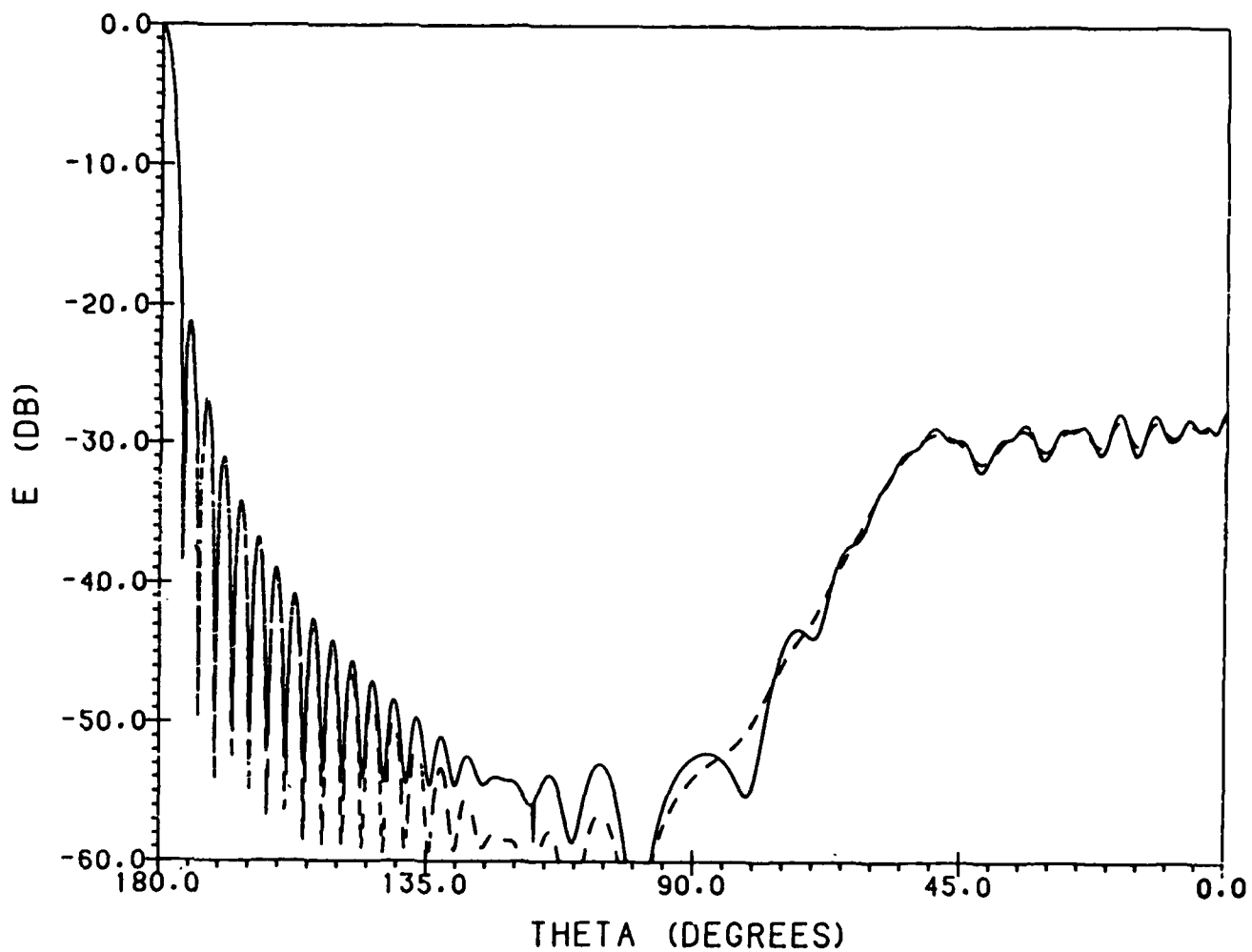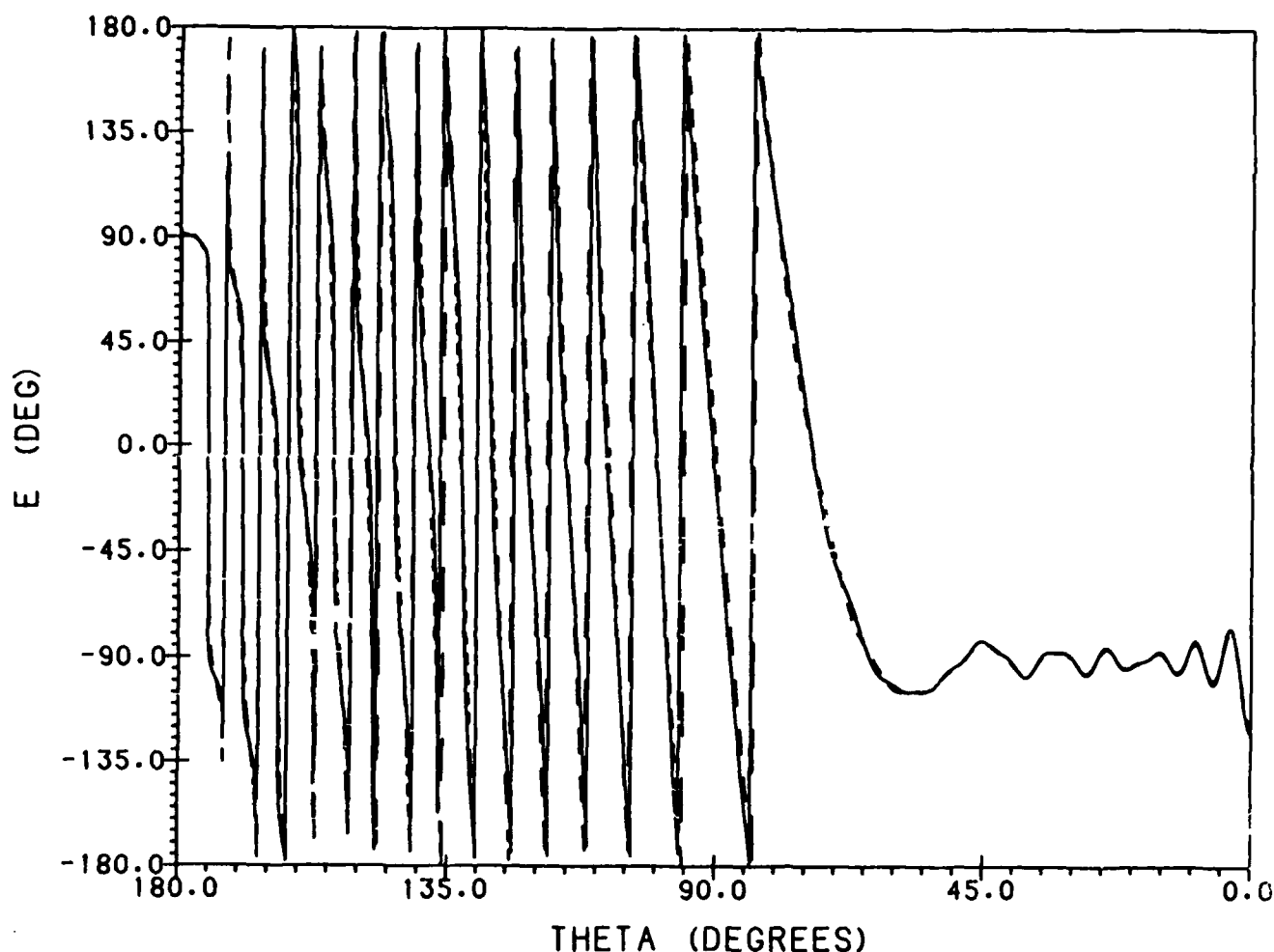Figure 19c. φ = 45° Cross-Polar Phase Pattern of 20λ Huygens-Feed Paraboloid Antenna, Primary Field Not Included; ---- PO, ———— PO + Nonuniform Current Field, F/D = 0.4, θ = [180°, 0°]

Comparing Figures 12 a, b showing the dipole-feed antenna E- and H-plane amplitude patterns without the primary feed field, with Figures 3 a, b showing the patterns with the primary field, we see that, once the masking effect of the primary field is removed, the effect of the nonuniform current field is principally to raise the PO null depths. This is the same effect that we have already noted above in discussing Figures 7 a, b for the Huygens-feed antenna patterns where the inclusion of the primary Huygens-feed field does little since it is close to zero in the forward reflector direction. The cross-polar patterns without the primary field dipole field shown in Figure 12c are very close to the corresponding patterns with the feed field shown in Figure 3c since, as noted above, the primary cross-polar dipole feed field is close to zero in directions close to the mainbeam of the reflector. The Huygens-feed antenna patterns without the primary field shown in Figures 16 a, b, c are all, as expected, quite close to the corresponding patterns shown in Figures 7 a, b, c with the primary field included.

65

Turning to the dipole-feed reflector patterns without the primary field for the full range of θ shown in Figures 14 a, b, c, we note that in the back directions (that is, $\theta < 60°$), the inclusion of the nonuniform current field has very little effect on the PO pattern. This is explained by the fact that the PO field in back of the reflector is very close to being equal and opposite to the primary feed field and so, in the absence of the primary field, masks the effect of the nonuniform current field. In contrast, the effect of the nonuniform current field in the back directions is seen much more strongly in Figures 5 a, b since in these patterns the PO field is largely cancelled by the primary field. A very similar effect is noted for the Huygens-feed reflector patterns without the primary field shown in Figures 18 a, b as compared with the patterns with the primary field shown in Figures 9 a, b. The mid-portion (130°–60°) of the E-plane and the cross-polar patterns of both the dipole- and Huygens-feed antennas is strongly affected by the nonuniform current field.

3.2 Comparison With Nonuniform Fields Obtained by Asymptotic Evaluation of the Diffraction Integrals

In the previous section, we enhanced the accuracy of the PO far fields of a 20λ diameter, 8λ focal-length reflector by adding the far fields of the nonuniform current near the rim of the reflector. These far fields radiated by the nonuniform current were obtained by integrating numerically the incremental diffraction coefficients in Eq. (47) and Eq. (48), which were derived assuming the nonuniform currents near the rim of the thin metal reflector are equal locally to those of a half plane tangent to the reflector at the rim.

Alternatively, we can evaluate the integrals in Eq. (47) and Eq. (48) asymptotically by the method of stationary phase to obtain closed-form approximate expressions for far fields radiated by the nonuniform current. Since the rim of the reflector is a smooth circular edge many wavelengths in diameter, the method of stationary phase should produce a very good approximation to the integrals except near the forward and back directions of the reflector, that is, near the caustics of the far-field rays emanating from the rim of the reflector.

Specifically, the two points of stationary phase are simply the two intersections of the rim of the reflector with the plane formed by the far-field direction and the axis of the reflector. The contribution from each of these two stationary points of diffraction can be found from the equations in Section 6.2 of Kouyoumjian[21] when the GTD diffraction coefficients in Eq. 6.32 of Kouyoumjian are replaced by the nonuniform (PTD) diffraction coefficients for the half plane,[5]

$$D_{TM}^{nu} = -\frac{2e^{i\pi/4}}{\sqrt{2\pi k}} \frac{\sin\frac{\phi_0}{2}}{|\cos\frac{\phi_0}{2}| + \sin\frac{\phi}{2}} \tag{52a}$$

$$D_{TE}^{nu} = -\frac{2e^{i\pi/4}}{\sqrt{2\pi k}} \, \text{sign}(\pi - \phi_0)\frac{\cos\frac{\phi}{2}}{|\cos\frac{\phi_0}{2}| + \sin\frac{\phi}{2}} \tag{52b}$$

Eq. (52a) and Eq. (52b) can also be ascertained by comparing D_s and D_h in Eq. 6.32 of Kouyoumjian with our Eqs. (3,8) and (5,9), respectively, for $\theta = \theta_0 = \pi/2$. Substitution of the 2 $-$ D nonuniform diffraction coefficients Eq. (52) into Eq. 6.30 of Kouyoumjian for the two points of stationary phase on the rim of the reflector shown in Figure 20, yields the following asymptotic approximations for the E- and H-plane fields radiated by the nonuniform current:

66

$$E_\theta^{nu}(\theta) = -H_{i\phi} Z_0 \sqrt{\frac{D\lambda}{2\sin\theta}} \frac{e^{i(kR+\pi/4)}}{2\pi R} \left[\frac{e^{-i\pi D \cos(\theta-\theta')/\lambda \sin\theta'} \cos\frac{\theta_1}{2}}{\sin\left(\frac{\beta'+\theta'}{2}\right) + \sin\frac{\theta_1}{2}} + \frac{ie^{-i\pi D \cos(\theta+\theta')/\lambda \sin\theta} \cos\frac{\theta_2}{2}}{\sin\left(\frac{\beta'+\theta'}{2}\right) + \sin\frac{\theta_2}{2}} \right] \quad (53)$$

(E-plane)

$$E_\phi^{nu}(\theta) = -E_{i\phi} \sqrt{\frac{D\lambda}{2\sin\theta}} \frac{e^{i(kR+\pi/4)}}{2\pi R} \cos\left(\frac{\beta'+\theta'}{2}\right) \left[\frac{e^{-i\pi D \cos(\theta-\theta')/\lambda \sin\theta'}}{\sin\left(\frac{\beta'+\theta'}{2}\right) + \sin\frac{\theta_1}{2}} - \frac{ie^{-i\pi D \cos(\theta+\theta')/\lambda \sin\theta}}{\sin\left(\frac{\beta'+\theta'}{2}\right) + \sin\frac{\theta_2}{2}} \right] \quad (54)$$

(H-plane)

where all the parameters in Eq. (53) and Eq. (54) have been given previously except for the fixed angle that the tangent plane at the rim makes with the z-axis,

$$\beta' = \frac{\pi}{2} - \frac{\theta'}{2},$$

θ_1 and θ_2 which are given in terms of θ as

$$\theta_1 = \begin{cases} 2\pi - (\theta + \beta'), & 0 < \theta < 2\pi - \beta' \\ 4\pi - (\theta + \beta'), & 2\pi - \beta' < \theta < 2\pi \end{cases}$$

$$\theta_2 = \begin{cases} 2\pi - (\theta - \beta'), & \beta' < \theta < 2\pi \\ \beta' - \theta, & 0 < \theta < \beta' \end{cases},$$

and $H_{i\phi}$ and $E_{i\phi}$, the incident magnetic and electric fields at $\phi' = 0$ and $\pi/2$, respectively, of the electric dipole or Huygens feed illuminating the rim of the reflector.

Figures 21a and 21b compare the E-plane amplitude and phase patterns (radiated by the nonuniform current) computed from the asymptotic expression, Eq. (53), (dashed line) and from the numerical integration of Eq. (47) (solid line) for the dipole fed reflector 20λ in diameter with F/D equal to 0.4. Figures 22a and 22b compare the nonuniform H-plane patterns for the same antenna computed from Eq. (48) and Eq. (54). As expected, the agreement is excellent except in the important caustic regions around the forward and back directions where the asymptotic expressions diverge to infinity. The apparent discrepancy in the E-plane amplitude pattern (Figure 21a) near $\theta = 55°$ is misleading. It is caused by the discontinuity in the diffraction coefficients along the face of the half-plane when the incident plane wave is transverse electric [see Eq. (52b)]. This discontinuity appears as a large phase jump ($\approx 180°$) in the asymptotic field Eq. (53), yet as a small amplitude jump. The fields computed from the numerical investiga tion in Eq. (47), however, are continuous, so that the $180°$ phase jump near $55°$ becomes a continuously yet rapidly varying field that goes through a null as shown by the solid curve of Figure 21a. Fortunately, the effect of the fields of either the solid or dashed curves of Figures 21a and 21b near $55°$ on the total field of the reflector are negligible compared to the PO fields near $55°$.
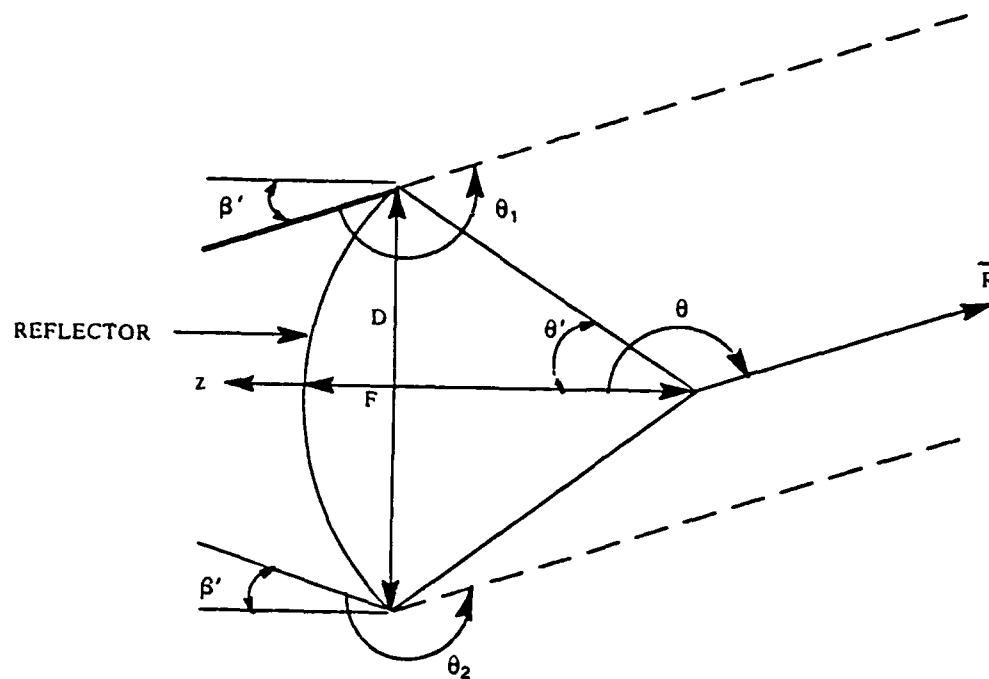
Figure 20. Geometry for Stationary Phase Evaluation of the Nonuniform Current Field

Figure 21a. E-Plane Amplitude Pattern of Nonuniform Fields of 20λ Dipole-Feed Paraboloid Antenna; – – – – Asymptotic, Eq. 53, ——— Numerical Integration, Eq. 47: F/D = 0.4, θ = [180°, 0°]

Figure 21b. E-Plane Phase Pattern of Nonuniform Fields of 20λ Dipole-Feed Paraboloid Antenna; — — — — Asymptotic, Eq. 53, ———— Numerical Integration, Eq. 47: F/D = 0.4, θ = [180°, 0°]
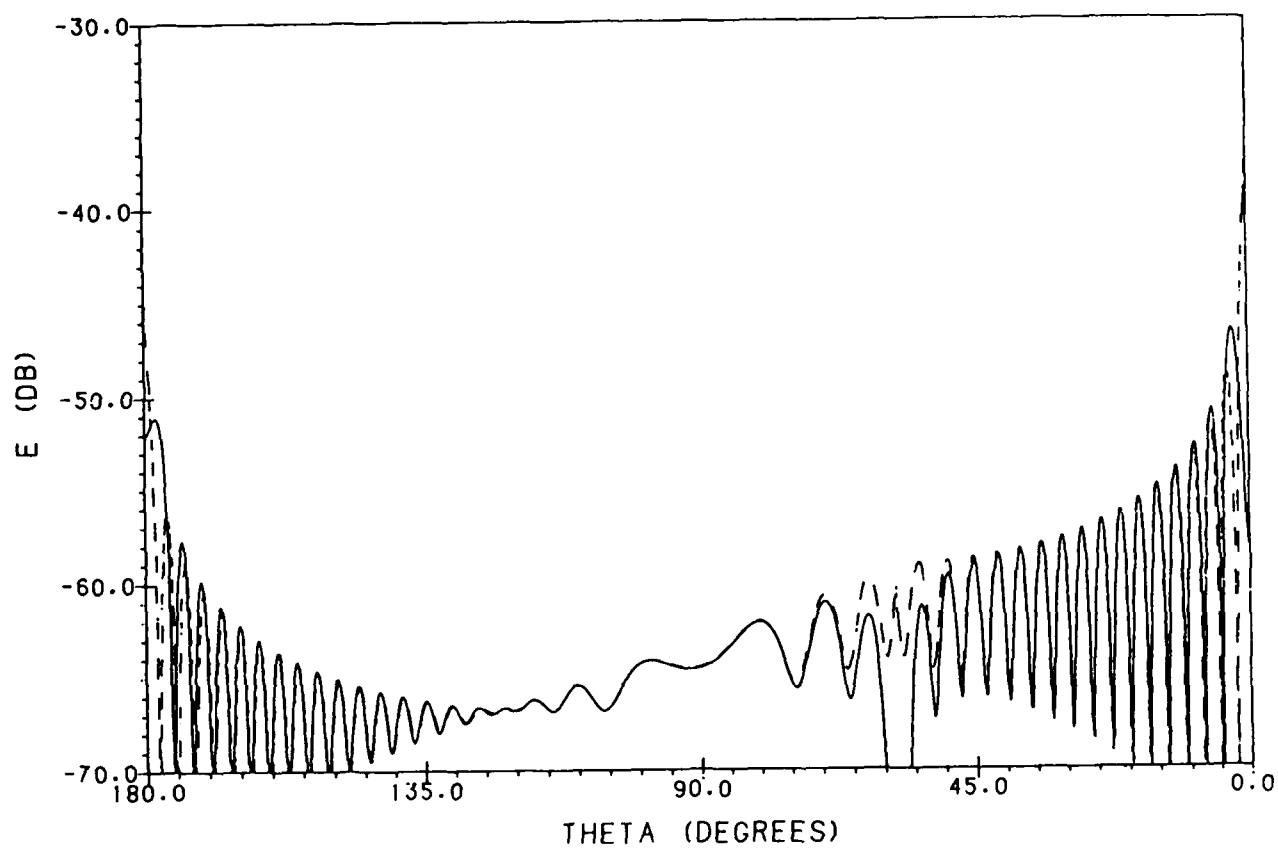
Figure 22a. H-Plane Amplitude Pattern of Nonuniform Fields of 20λ Dipole-Feed Paraboloid Antenna;
– – – – Asymptotic, Eq. 54, ———— Numerical Integration, Eq. 48: F/D = 0.4, θ = [180°, 0°]
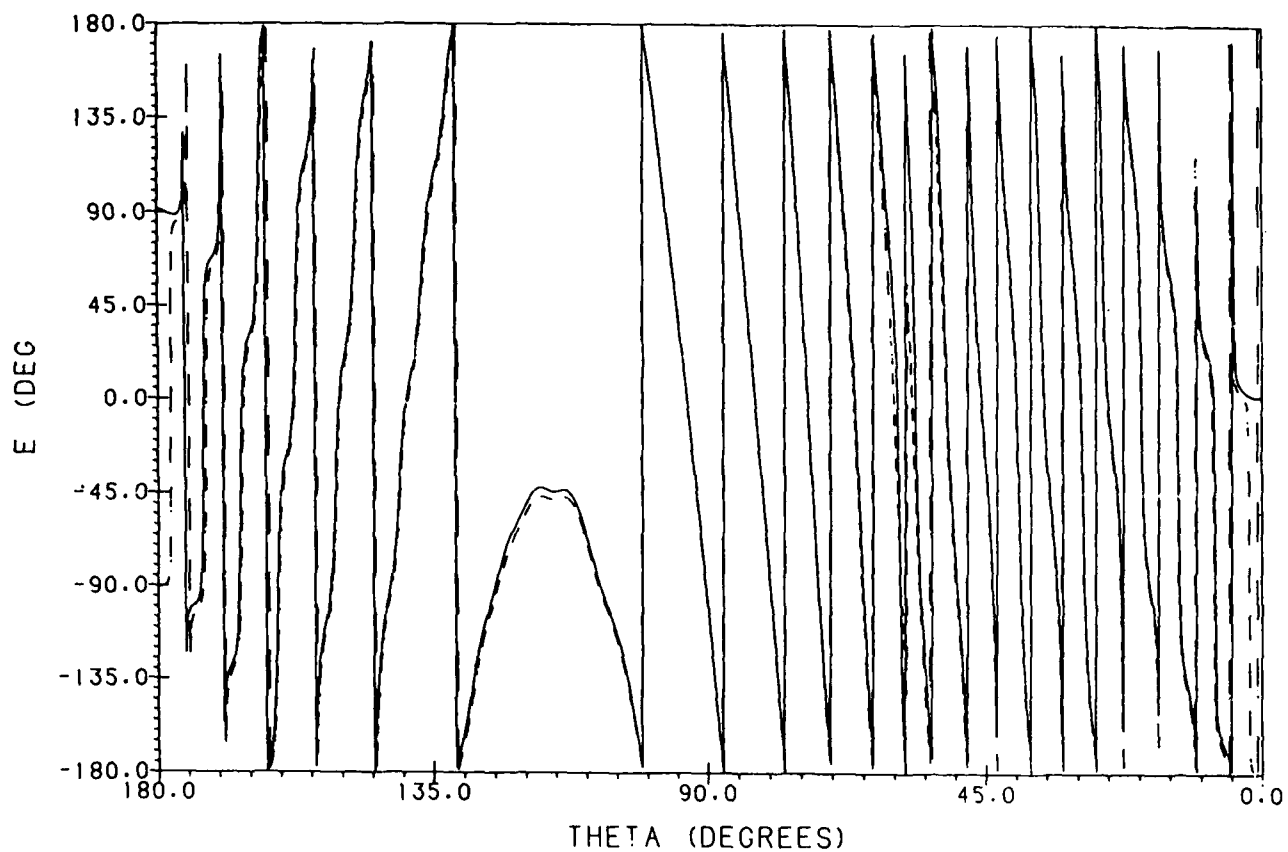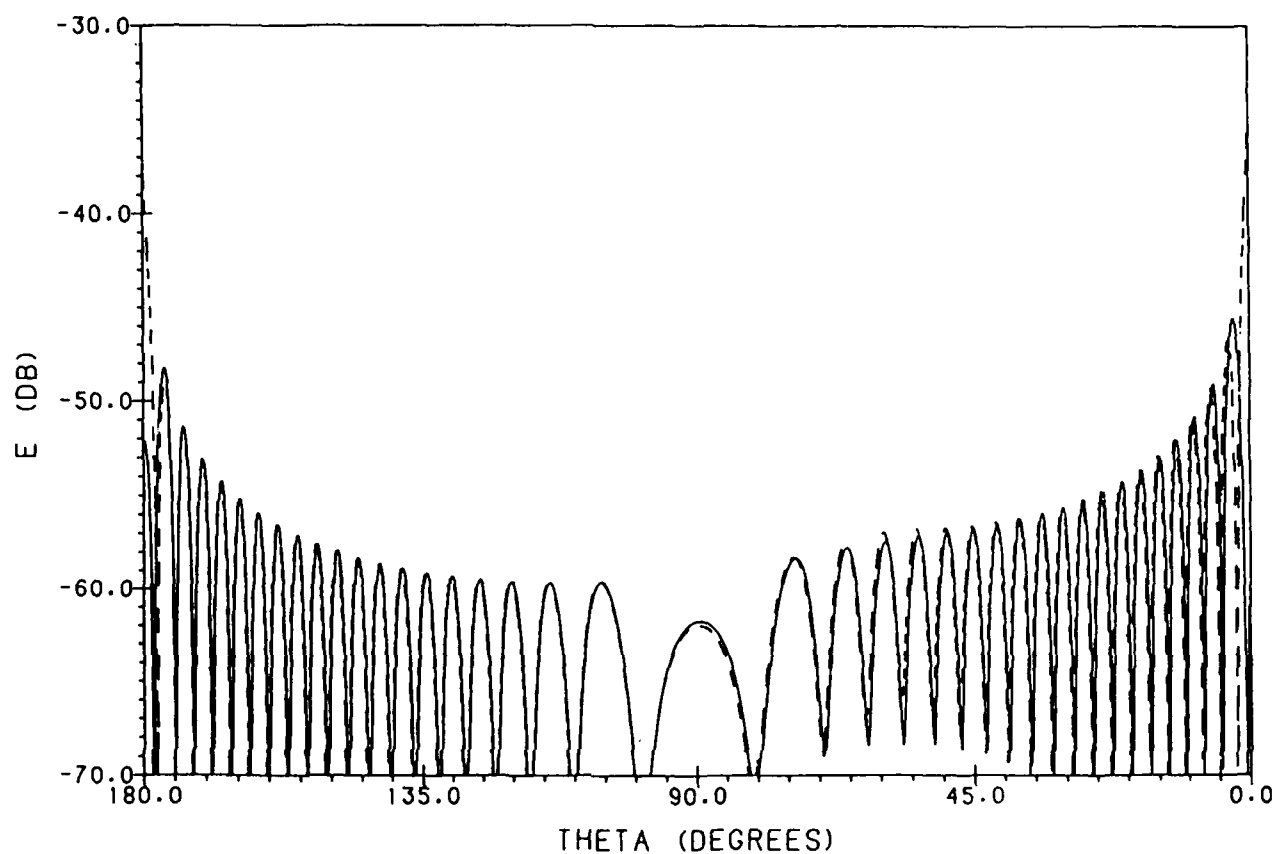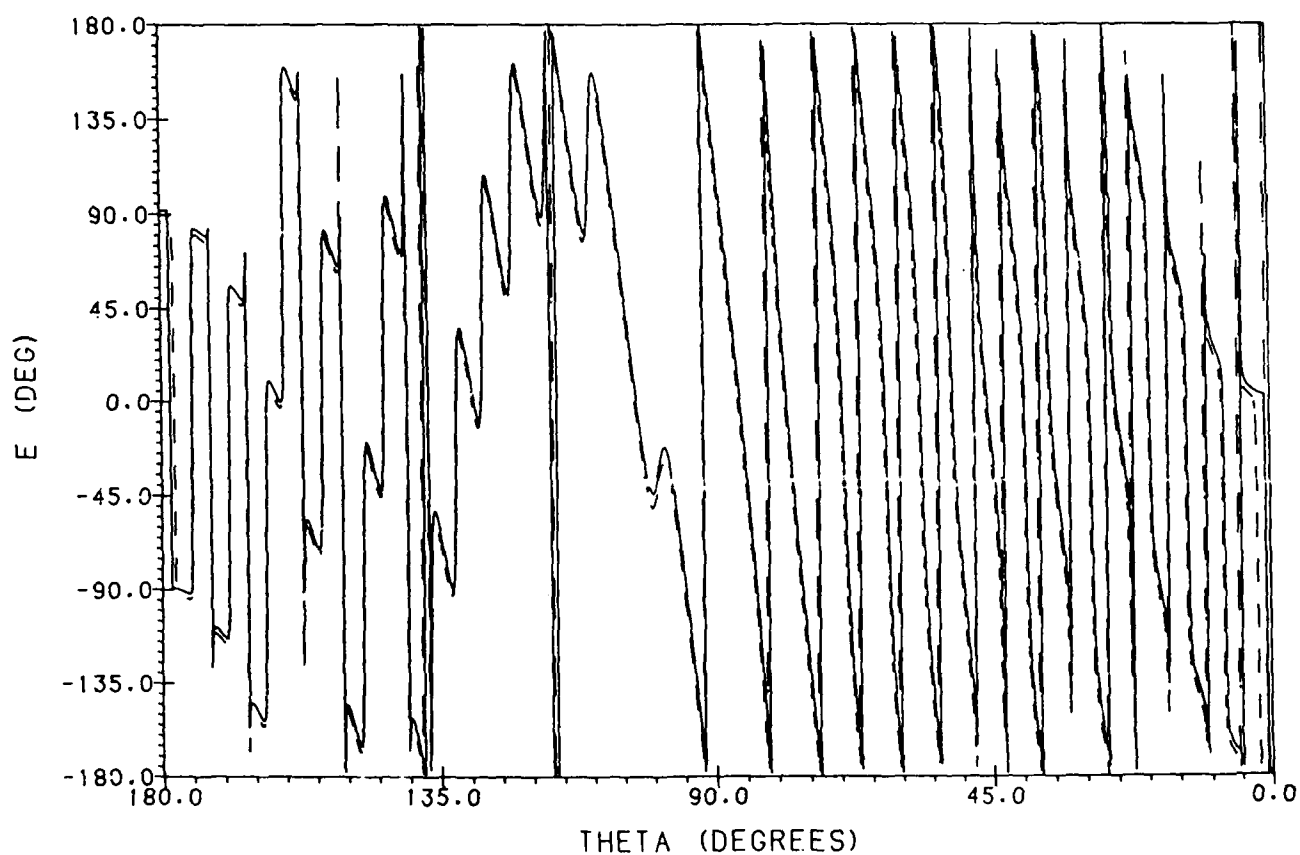
Figure 22b. H-Plane Phase Pattern of Nonuniform Fields of 20λ Dipole-Feed Paraboloid Antenna;
– – – – Asymptotic, Eq. 54, ——— Numerical Integration, Eq. 48: F/D = 0.4, θ = [180°, 0°]

References

1. Franceschetti, G., and Mohsen, A. (1986) Recent developments in the analysis of reflector antennas. A review, *IEE Proc.* **133(Pt. H)**: 65–76.

2. Love, A.W., Ed. (1978) *Reflector Antennas*, New York: IEEE.

3. Yaghjian, A.D. (1984) Equivalence of the surface current and aperture field integrations for reflector antennas, *IEEE Trans. Antennas Propag.*, **AP-32**:1355-1358.

4. Steyskal, H., and Shore, R.A. (1984) *Simple and Efficient Computation of Reflector Antenna Aperture Distributions and Far-Field Patterns*, RADC-TR-84-45, AD A147367.

5. Ufimtsev, P. Ia. (1957, 1958) Approximate computation of the diffraction of plane electromagnetic waves at certain metal bodies, I and II, *Sov. Phys-Tech. Phys.* **27** (1957):1708–1718; **28**(1958):2386–2396.

6. Braunbek, W. (1950) Neue Naherungsmethode fur die Beugung am ebenen Schirm, and Zur Beugung an der Kreisscheibe, *Z. Physik*, **127**:381–390 and 405–415.

7. Bach, H., and Viskum, H.H. (1986) Comparison of three cross-polarization prediction methods for reflector antennas, *IEE Proc.* **133(Pt. H)**:325–326. (1987) The SNFGTD method and its accuracy, *IEEE Trans. Antennas Propag.* **AP-35**:169–175.

8. Keller, J.B. 1962) Geometrical theory of diffraction, *J. Opt. Soc. Am.* **52**:116-130.

9. Chang, Y.C. (1984) *Analysis of Reflector Antennas with Array Feeds Using Multi-Point GTD and Extended Aperture Integration*, Technical Report 71559-3: Ohio State University.

10. Mitzner, K.M. (1974) *Incremental Length Diffraction Coefficients*, AFAL-TR-73-296 (available from NTIS, Springfield, VA 22161, AD918861).

11. Michaeli, A. (1984, 1985) Equivalent edge currents for arbitrary aspects of observation, *IEEE Trans. Antennas Propag.* **AP-32**:252-258, **AP-33**:227.

12. Knott, E.F. (1985) The relationship between Mitzner's ILDC and Michaeli's equivalent currents, *IEEE Trans. Antennas Propag.* **AP-33**:112–114.

13. Millar, R.F. (1956) An approximate theory of the diffraction of an electromagnetic wave by an aperture in a plane screen, *Proc. IEE*, **103(Pt. C)**:177–185 (first published as Monograph 152R, 1955).

14. Millar, R.F. (1957) The diffraction of an electromagnetic wave by a circular aperture, *Proc. IEE*, **104(Pt. C)**:87–95 (first published as Monograph 196R, 1956).

15. Millar, R.F. (1957) The diffraction of an electromagnetic wave by a large aperture, *Proc. IEE*, **104(Pt. C)**:240–250 (first published as Monograph 213R, 1956)

16. Ryan, C.E., Jr., and Peters, L., Jr. (1969) Evaluation of edge-diffracted fields including equivalent currents for the caustic regions, *IEEE Trans. Antennas Propag.* **AP-17**:292–299.

17. Shore, R.A., and Yaghjian, A.D. (1987) *Incremental Diffraction Coefficients for Planar Surfaces, Part I: Theory*, RADC-TR-87-35.

18. Ludwig, A.C. (1973) The definition of cross polarization, *IEEE Trans. Antenas Propag.* **AP-21**:116-119.

19. Rusch, W.V.T. (1974) *Antenna Notes* (Vol. II), NB 84B, University of Denmark: Lyngby, Denmark.

20. Viskum, H.H., Frandsen, A.B., and Bach, H. (1987) Private communication.

21. Kouyoumjian, R.G. (1975) The geometrical theory of diffraction and its application, ch. 6 in R. Mittra (ed.) *Topics in Applied Physics* (Vol. 3): *Numerical and Asymptotic Techniques in Electromagnetics*, New York: Springer-Verlag.

MISSION
of
Rome Air Development Center

RADC plans and executes research, development, test and selected acquisition programs in support of Command, Control, Communications and Intelligence (C³I) activities. Technical and engineering support within areas of competence is provided to ESD Program Offices (POs) and other ESD elements to perform effective acquisition of C³I systems. The areas of technical competence include communications, command and control, battle management, information processing, surveillance sensors, intelligence data collection and handling, solid state sciences, electromagnetics, and propagation, and electronic, maintainability, and compatibility.